

INFORMATION TO USERS

This manuscript has been reproduced from the microfilm master. UMI films the text directly from the original or copy submitted. Thus, some thesis and dissertation copies are in typewriter face, while others may be from any type of computer printer.

The quality of this reproduction is dependent upon the quality of the copy submitted. Broken or indistinct print, colored or poor quality illustrations and photographs, print bleedthrough, substandard margins, and improper alignment can adversely affect reproduction.

In the unlikely event that the author did not send UMI a complete manuscript and there are missing pages, these will be noted. Also, if unauthorized copyright material had to be removed, a note will indicate the deletion.

Oversize materials (e.g., maps, drawings, charts) are reproduced by sectioning the original, beginning at the upper left-hand corner and continuing from left to right in equal sections with small overlaps.

Photographs included in the original manuscript have been reproduced xerographically in this copy. Higher quality 6" x 9" black and white photographic prints are available for any photographs or illustrations appearing in this copy for an additional charge. Contact UMI directly to order.

Bell & Howell Information and Learning
300 North Zeeb Road, Ann Arbor, MI 48106-1346 USA
800-521-0600



Efficient Hybrid MoM/Green's Function Technique to Analyze
Conformal Microstrip Antennas and Arrays

DISSERTATION

Presented in Partial Fulfillment of the Requirements for
the Degree Doctor of Philosophy in the
Graduate School of The Ohio State University

By

Vakur Behçet Ertürk, M.S., B.S.

* * * * *

The Ohio State University

2000

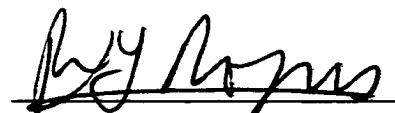
Dissertation Committee:

R. G. Rojas, Adviser

E. H. Newman

W. D. Burnside

Approved by



Adviser

Department of Electrical
Engineering

UMI Number: 9971543



UMI Microform 9971543

Copyright 2000 by Bell & Howell Information and Learning Company.
All rights reserved. This microform edition is protected against unauthorized copying under Title 17, United States Code.

**Bell & Howell Information and Learning Company
300 North Zeeb Road
P.O. Box 1346
Ann Arbor, MI 48106-1346**

ABSTRACT

An efficient and accurate hybrid method based on the combination of the method of moments (MoM) with a special Green's function in the space domain is presented to analyze antennas and array elements conformal to material coated large circular cylinders. This method can be used for the analysis and design of microstrip structures mounted on aircraft, spacecraft and many types of mobile communication applications where low cost, light weight and direct integrability with other devices are important. The efficiency and accuracy of the method strongly depends on the computation of the Green's function which is the kernel of the integral equation solved via MoM for the unknown equivalent currents representing only the antenna elements. Therefore, three types of space domain Green's function representations are used interchangeably, based on the computational efficiency of their calculation and the region where they remain highly accurate. The first one is the steepest descent path (SDP) representation of the special Green's function. This representation is based on obtaining a circumferentially propagating series representation of the appropriate Green's function from its radially propagating counterpart and its efficient numerical evaluation along a steepest descent path (SDP) on which the integrand decays most rapidly. The self and neighboring term calculations in the MoM procedure are performed using an efficient integral representation of the planar microstrip dyadic Green's function. This is based on the assumption that for an electrically large

dielectric coated circular cylinder small separations between source and observation points can be treated as flat surfaces. To calculate the mutual coupling between two current modes in the paraxial (near axial) region (i.e. close to the normal section of the cylinder, passing through the source point and parallel to the cylinder axis), another space domain representation is obtained based on the fact that the circumferentially propagating series representation of the appropriate Green's function is periodic and hence can be approximated by a Fourier series where only the first two terms are included. Consequently, besides combining different representations of the Green's functions with the MoM to obtain a computationally optimized analysis tool for conformal microstrip antennas, new asymptotic space domain Green's function representations are derived for the cases in which previously derived solutions do not yield accurate results. Input impedance of various microstrip antennas and mutual coupling between two identical antennas are calculated and compared with published results to assess the accuracy of this hybrid method.

To My Mother and To the Spirit of My Father

ACKNOWLEDGMENTS

I would like to express my gratitude to my advisor Prof. Roberto G. Rojas who have very closely advised, guided and encouraged me in my research leading to this dissertation. I also wish to thank Prof. E. H. Newman and Prof. W. D. Burnside for participating in the reading committee and for their helpful advise. Many thanks are also owed to my friends, in particular, I. K. Sendur and K. W. Lee (Simon) for their helpful discussions and again to K. W. Lee (Simon) for his helps for the MoM codes.

Finally, I want to express a special note of thanks to my mother to whom I owe a deep debt of gratitude.

VITA

June 13, 1971 Born - Ankara, Turkey

1993 B.S. Electrical Engineering, Middle East Technical University, Ankara, Turkey

1996 M.S. Electrical Engineering, The Ohio State University, Columbus, Ohio

1993-present Graduate Research Associate, The Ohio State University

FIELDS OF STUDY

Major Field: Electrical Engineering

Studies in:

Electromagnetic Theory	Prof. P. H. Pathak
Communication Theory	Prof. U. Mitra
Mathematics	Prof. U. Gerlach

TABLE OF CONTENTS

Abstract	ii
Dedication	iv
Acknowledgments	v
Vita	vi
List of Figures	x
List of Tables	xv
	Page
Chapters:	
1. Introduction	1
2. Efficient Computation of Surface Fields Excited on a Dielectric Coated Circular Cylinder	16
2.1 Introduction	16
2.2 Development of an Eigenfunction Series Representation of the Surface Fields due to a Current Distribution on the Surface of a Coated Cylinder	17
2.2.1 Tangential Components	20
2.2.2 Normal Components	22
2.2.3 Numerical Considerations	24
2.3 Development of Steepest Descent Path Integral Representation for the Surface Fields	25
2.4 Numerical Evaluation of Special Functions	31
2.4.1 Evaluation of R_ν	32

2.4.2	Evaluation of C_ν^m , C_ν^e , C_ν^{pr1} and C_ν^{pr2}	36
2.5	Numerical Evaluation of Integrals	43
2.5.1	The Choice of Integration Contour	47
2.5.2	Integration Routine and Tail Contributions	49
2.6	Numerical Results	54
3.	Paraxial Space-Domain Formulation for Surface Fields on Dielectric Coated Circular Cylinder	65
3.1	Introduction	65
3.2	Development of the Approximate Green's Function	66
3.2.1	Tangential Components	68
3.2.2	Normal Components	74
3.3	Calculation of Surface Fields	75
3.4	Numerical Results	78
3.4.1	Expressions for regions away from the paraxial region	79
4.	The MoM/Green's Function Solution	94
4.1	Introduction	94
4.2	Development of Integral Equation	95
4.3	Moment Method Solution	98
4.4	Numerical Results	100
5.	Conclusion	115

Appendices:

A.	Limiting Case of the SDP Integral Representation of the Surface Fields for a Dielectric Coated Circular Cylinder	117
A.1	The Limiting Expression for $E_z(\alpha, s)$	119
A.2	The Limiting Expression for $E_\phi(\alpha, s)$	122
B.	Limiting Values of the SDP Integral Representation of the Surface Fields for a Dielectric Coated Circular Cylinder for large τ values	126
C.	Approximation of Periodic Functions Using Fourier Series	130

D. Representation of $G_{\phi\phi}(\zeta, \psi)$ component as the sum of Planar + Curvature Correction terms	132
E. Special Functions used to Calculate the Approximate Space Domain Green's Function Representations valid in the Paraxial Region	137
Bibliography	144

LIST OF FIGURES

Figure	Page
2.1 The geometry of a cylinder with inner radius a and outer radius d	20
2.2 Contour used to evaluate (2.36) in the complex ν – plane	26
2.3 Steepest Descend Path (SDP) Contour	29
2.4 The real and imaginary parts of R_ν for $a = 3\lambda_0$, $t_h = 0.06\lambda_0$, $\epsilon_r = 3.25$ and $\alpha = \psi = 25^\circ$	34
2.5 The real and imaginary parts of R_ν for $a = 0.3\lambda_0$, $t_h = 0.06\lambda_0$, $\epsilon_r = 2.33$ and $\alpha = \psi = 40^\circ$	35
2.6 The real and imaginary parts of C_ν^e for $a = 3\lambda_0$, $t_h = 0.06\lambda_0$, $\epsilon_r = 3.25$ (i.e. $t_h = 0.1082\lambda_d$) and $\alpha = \psi = 25^\circ$	39
2.7 The real and imaginary parts of C_ν^m for $a = 3\lambda_0$, $t_h = 0.06\lambda_0$, $\epsilon_r = 3.25$ (i.e. $t_h = 0.1082\lambda_d$) and $\alpha = \psi = 25^\circ$	40
2.8 The real and imaginary parts of C_ν^e for $a = 0.3\lambda_0$, $t_h = 0.06\lambda_0$, $\epsilon_r = 2.33$ (i.e. $t_h = 0.0916\lambda_d$) and $\alpha = \psi = 40^\circ$	41
2.9 The real and imaginary parts of C_ν^m for $a = 0.3\lambda_0$, $t_h = 0.06\lambda_0$, $\epsilon_r = 2.33$ (i.e. $t_h = 0.0916\lambda_d$) and $\alpha = \psi = 40^\circ$	42
2.10 The real and imaginary parts of C_ν^e for $a = 3\lambda_0$, $t_h = 0.142\lambda_0$, $\epsilon_r = 3.25$ (i.e. $t_h = 0.2560\lambda_d$) and $\alpha = \psi = 25^\circ$	44
2.11 The real and imaginary parts of C_ν^e for $a = 3\lambda_0$, $t_h = 0.06\lambda_0$, $\epsilon_r = 17.5$ (i.e. $t_h = 0.2510\lambda_d$) and $\alpha = \psi = 25^\circ$	45

2.12 Integration paths C and \tilde{C} in the complex $\nu-$ plane	48
2.13 Integration points on the SDP contour	49
2.14 Typical integration contours in the $\tau-$ plane	50
2.15 Effect of tail contribution on an integral in the form of (2.78) for a coated cylinder with $a = 3\lambda_0$, $t_h = 0.06\lambda_0$, $\epsilon_r = 3.25$ and $\alpha = 40^\circ$	53
2.16 Effect of the envelope extraction technique on an integral written in the form of (2.86) for a coated cylinder with $a = 2.5\lambda_0$, $t_h = 0.06\lambda_0$, $\epsilon_r = 2.33$ and $\alpha = 50^\circ$	55
2.17 (a) Geometry used for mutual coupling problem (b) Piecewise sinusoidal current distribution on each tangential element.	59
2.18 Real and imaginary parts of the mutual coupling between two identical z -directed current sources for two coated cylinders of different radii.	60
2.19 Real and imaginary parts of the mutual coupling between ϕ - and z -directed current sources for two coated cylinders of different radii.	61
2.20 Real and imaginary parts of the mutual coupling between two ϕ -directed current sources for two coated cylinders of different radii.	62
2.21 Real and imaginary parts of the mutual coupling between a tangential and a ρ -directed current sources for a coated cylinder with $a = 2.0184\lambda_0$, $t_h = 0.0214\lambda_0$, $\epsilon_r = 2.94$	63
2.22 Real and imaginary parts of the mutual coupling between two tangential current sources for a coated cylinder with $a = 3.0\lambda_0$, $t_h = 0.06\lambda_0$, $\epsilon_r = 3.25$, $\alpha = 70^\circ$	64
3.1 The algorithm used to calculate the surface fields accurate around the paraxial region	67
3.2 Space (s, δ) and spectral (ζ, ψ) polar coordinates after [53]	68
3.3 Real and imaginary parts of the mutual coupling between two identical z -directed current sources.	80

3.4	Real and imaginary parts of the mutual coupling between two identical z -directed current sources.	81
3.5	Real and imaginary parts of the mutual coupling between ϕ - and z -directed current sources.	82
3.6	Real and imaginary parts of the mutual coupling between ϕ - and z -directed current sources.	83
3.7	Real and imaginary parts of the mutual coupling between two ϕ -directed current sources.	84
3.8	Real and imaginary parts of the mutual coupling between two ϕ -directed current sources.	85
3.9	Real and imaginary parts of the mutual coupling between two ϕ -directed current sources.	86
3.10	Real and imaginary parts of the mutual coupling between ϕ - and z -directed current sources.	89
3.11	Real and imaginary parts of the mutual coupling between two ϕ -directed current sources.	90
3.12	Real and imaginary parts of the mutual coupling between ϕ - and z -directed current sources.	91
3.13	Real and imaginary parts of the mutual coupling between two ϕ -directed current sources.	92
4.1	Equivalence Principle	96
4.2	Mutual coupling (Z_{12}) between two identical z -directed current modes for a coated cylinder with $a = 3\lambda_0, t_h = 0.06\lambda_0, \epsilon_r = 3.25$	101
4.3	Mutual coupling (Z_{12}) between ϕ and z -directed current modes for a coated cylinder with $a = 3\lambda_0, t_h = 0.06\lambda_0, \epsilon_r = 3.25$	102
4.4	Mutual coupling (Z_{12}) between two ϕ -directed current modes for a coated cylinder with $a = 3\lambda_0, t_h = 0.06\lambda_0, \epsilon_r = 3.25$	102

4.5 Mutual coupling (Z_{12}) between two identical z -directed current modes for a coated cylinder with $a = 3\lambda_0$, $t_h = 0.06\lambda_0$, $\epsilon_r = 3.25$	103
4.6 Mutual coupling (Z_{12}) between two identical ϕ -directed current modes for a coated cylinder with $a = 3\lambda_0$, $t_h = 0.06\lambda_0$, $\epsilon_r = 3.25$	103
4.7 The geometry for the (a) input impedance and (b) the mutual coupling problems. (c) Definitions of two-port voltages and currents.	109
4.8 Input impedance versus frequency for the patch excited with a TM_{01} mode; $a = 20$ cm, $\epsilon_r = 2.32$, $t_h = 0.795$ mm, $L = 3$ cm, $W = 4$ cm with $(z_f, rl_f) = (0.5cm, 2cm)$	110
4.9 Input impedance versus frequency for the patch excited with a TM_{01} mode; $a = 20$ cm, $\epsilon_r = 2.32$, $t_h = 0.795$ mm, $L = 3$ cm, $W = 4$ cm with $(z_f, rl_f) = (0.95cm, 2cm)$	110
4.10 Mutual coupling coefficient s_{12} for the E-plane coupling case, the antenna parameters are the same as given in Fig. 4.9	111
4.11 Mutual coupling coefficient s_{12} for the H-plane coupling case, the antenna parameters are the same as given in Fig. 4.9	111
4.12 Convergence curve for input impedance at $f = 3175MHz$. The antenna parameters are: $a = 20$ cm, $\epsilon_r = 2.32$, $t_h = 0.795$ mm, $L = 3$ cm, $W = 4$ cm. Size of basis functions along the ϕ -direction is decreased while the size of the z -directed basis functions is kept constant.	112
4.13 Convergence curve for input impedance at $f = 3175MHz$. The antenna parameters are: $a = 20$ cm, $\epsilon_r = 2.32$, $t_h = 0.795$ mm, $L = 3$ cm, $W = 4$ cm. Size of basis functions along the z -direction is decreased while the size of the ϕ -directed basis functions is kept constant.	112
4.14 Input impedance versus frequency for the patch excited at the TM_{01} mode. The antenna parameters are: $a = 40$ cm, $\epsilon_r = 2.98$, $t_h = 0.762$ mm, $L = 6$ cm, $W = 4$ cm.	113
4.15 Mutual coupling coefficient s_{12} for the E-plane coupling case where the antenna parameters are the same as given in Fig. 4.14	113

4.16 Mutual coupling coefficient s_{12} for the H-plane coupling case where the antenna parameters are the same as given in Fig. 4.14	114
A.1 High frequency method used by [3] to find the UTD-based radiated and surface fields	118

LIST OF TABLES

Table	Page
2.1 Abscissas and weights for Gauss-Hermite integration algorithm	47

CHAPTER 1

Introduction

Microstrip antennas and arrays have gained prominence over the last 20 years and have naturally replaced conventional antennas for many applications ranging from satellite and wireless communications, environmental instrumentation and remote sensing to biomedical applications. The interest in these antennas comes directly from their advantages over conventional microwave antennas such as low fabrication cost, light weight, mass production, conformity to surface and direct integrability with other microwave and solid-state devices. Therefore, there has been major advances in the area of computer aided design (CAD) technology due to the development of efficient and accurate numerical methods for the modeling of microstrip elements. Although many practical applications such as high-velocity aircraft, missiles, space vehicles, etc. have stringent aerodynamic constraints that require the use of antennas that conform to their surface, the majority of the work for microstrip elements has been for planar structures. This necessitates the development of efficient and accurate analytical and numerical tools for this class of antennas conformal to cylindrically shaped substrates.

In this dissertation, an efficient and accurate space domain hybrid method, based on the combination of the method of moments (MoM) [1] with a special Green's

function, is used to analyze microstrip antennas and array elements conformal to material coated electrically large cylinders. This method is also referred to as the hybrid MoM/Green's function method [2]. An exact integral equation for the unknown equivalent currents representing only the microstrip patches on top of the substrate is formulated and contains as its kernel the special Green's function, developed in this dissertation (which satisfies the boundary conditions of a dielectric coated perfectly electric conducting (PEC) circular cylinder). The unknown equivalent currents in the integral equation are then solved using the MoM procedure. Briefly, they are expanded as a finite sum of N basis functions, and N weighted averages of the integral equation are enforced on the microstrip patches which transforms the integral equation into a matrix equation whose order is N . Finally, the matrix equation is solved for the N coefficients in the expansion for the current on the microstrip patches.

The efficiency and accuracy, which are the most important issues in this hybrid method, depend strongly on the computation of the Green's functions which should yield accurate results for arbitrary source and observation locations. In order to achieve this goal, three different types of space domain Green's function representations are combined with the MoM. The first one is the Steepest Descent Path (SDP) representation of the special Green's function. This is based on obtaining a circumferentially propagating (ϕ -propagating) series representation of the appropriate Green's function from its radially propagating (ρ -propagating) counterpart, and its efficient numerical evaluation along a SDP on which the integrand decays most rapidly. In this case, as the separation between the source and observation points increases, the numerical integration becomes even faster and easier to perform. In the limiting case of large separations, this method reduces to the leading term of the

saddle point integration (uniform theory of diffraction (UTD) [3] based Green's function) considered in [4], [5] and [6]. However, in contrast to most asymptotic solutions, the results obtained in this method are valid for very small separations of source and field points. The second representation is an efficient integral representation of the planar microstrip dyadic Green's function which was derived by Barkeshli [7]. This representation is used for the calculation of self-terms and mutual coupling between two neighboring current modes (or sources) in the MoM procedure. For a dielectric coated electrically large circular cylinder ($d = \text{outer radius} > \lambda; \lambda = \text{wavelength}$), small separations between source and observation points can be treated as flat surfaces and planar approximations can be used. Finally, a third type of representation is necessary around the paraxial (i.e. near axial) region of the coated circular cylinder because the aforementioned SDP representation of the special Green's function is not valid in this region. This is a well-known problem that has been observed for PEC and impedance cylinders in the past [8–10]. Furthermore, the planar approximations are not valid in this region as well since the curvature effects are not taken into account, yielding inaccurate results as the distance between the source and observation points become large. A valid representation in this region is obtained based on the fact that the circumferentially propagating series representation of the appropriate Green's function is periodic and hence can be approximated by a Fourier series where only the first two terms of the expansion are included. The accuracy of this paraxial Green's function representation as well as the ease of its evaluation is determined by the integration algorithm used to obtain the Fourier series coefficients. Thus, another important contribution of this study is the development of a new asymptotic space domain Green's function representation for an electrically large dielectric

coated circular cylinder. This new solution may be useful toward the development of asymptotic solutions valid for an arbitrary smooth coated surface.

At this point, it is worthwhile to briefly mention the advantages and disadvantages of this hybrid method over the other conventional methods to analyze the microstrip elements on a dielectric coated cylindrical structure. The conventional Method of Moments has been very popular for the solution of EM problems due its ability to treat complex bodies of general shape and material composition where the whole body is replaced by free-space and equivalent currents using the surface and/or volume equivalence theorems [11]. An exact integral equation, whose kernel is the free-space Green's function, is formulated for the unknown equivalent currents. Then these unknown currents are solved by using the aforementioned MoM procedure. However, the practical use of the conventional MoM is restricted to bodies that are not large in terms of wavelength since it suffers greatly from storage requirements and computing time due to the restriction of placing a fixed number of unknowns per unit electrical surface area (λ^2 ; λ = wavelength) or volume (λ^3). Some other pure numerical methods such as the Finite Element Method (FEM) and the Finite Difference Time Domain (FDTD) have the same problems. On the other hand, Green's function solutions are more accurate, and in many cases computationally efficient but available only for simple structures. Using this hybrid MoM/Green's function method, the flexibility of MoM is combined with the efficiency and accuracy of the Green's function. Compared with the conventional MoM solution, the number of unknowns in the integral equation diminishes significantly, and hence, electrically larger structures can be analyzed using less CPU time and storage. For example, in this research, the unknown currents are restricted to the microstrip patches on top of the substrate, rather than the whole

dielectric coated body in addition to all the microstrip patches if the conventional MoM were used.

A similar hybrid approach for conformal microstrip antennas is also a MoM/Green's function method performed in the spectral domain in which the exact plane wave spectral representations of the Green's function (the traditional eigenfunction representation) is the kernel of the integral equation solved via MoM for the unknown equivalent currents [12], [13]. The advantages of this formulation are the evaluation of some integrals in closed form using a carefully chosen MoM basis function (piece-wise sinusoidal (PWS), triangular, etc.), and this formulation avoids the singularity problems which arise when a space domain formulation is used to calculate the self-impedance terms. However, spectral domain MoM/Green's function methods are extremely inefficient in terms of computational time. Furthermore, the spectral representation of the Green's function, which involves a series summation in terms of Bessel functions and a Fourier integral, has severe convergence problems for large cylinders and separations between source and observation points. The aforementioned basis functions can alleviate the convergence problem to some extent, even though the rate of convergence is still very slow. Moreover, the restriction in the selection of basis functions limits the usage of this method to some simple geometries. It is worthwhile to mention that the spectral domain hybrid MoM/Green's function method can only be used for geometries which conform with a coordinate axis so that the plane wave spectral representations of the Green's function can be obtained. Although this is possible for a material (dielectric) coated circular cylinder, it is not possible for material (dielectric) coated arbitrarily shaped convex structures.

The concept of conformal microstrip antennas and microstrip arrays can be traced back to the 1970's where some significant work has been reported [14–16]. The need for conformal antennas for high-speed missiles and aircraft, together with the advances in printed circuit technology and availability of better microstrip substrates led to the development of new design and analysis tools. The cavity model was one of the earliest models used to design and analyze rectangular microstrip antennas on circular dielectric coated perfect electric conducting (PEC) cylinders [17–19]. In [17], the main concern was to find the resonance frequencies, f_r , and investigate the effects of curvature on the resonance frequencies for thin dielectric coated cylindrical-rectangular microstrip antennas. This study was extended in [18, 19] to include the input impedance, Z_{in} , the quality factor (Q-factor), the bandwidth and radiation patterns. These studies were mainly limited to antennas whose coating thicknesses were much smaller than both the inner radius of the cylinder and the free space wavelength so that only TM _{r} modes were assumed to exist. Based on some approximate calculations and comparisons with experiments, they concluded that resonance frequencies were not affected by the radius of curvature however, the radiation patterns were significantly affected. Moreover, their results showed that curvature has different effects on the characteristics of TM₁₀, and TM₀₁ modes [18, 19]. Finally, using the same approach, the behavior of a circular patch antenna on a dielectric coated circular cylinder was investigated in [20] for the TM₁₁ mode. Although the cavity model is not accurate compared to the full-wave analysis, the simplicity and efficiency of this method enable researchers to design and investigate the basic characteristics of fairly complex structures on coated circular cylinders [21, 22] and rectangular patches on coated elliptic cylinders [23].

The use of cavity models or other approximate models such as the generalized transmission line model (GTLM) [24] as first cut design tools for conformal microstrip structures is a reasonable approach. However, a final design should be accurately obtained before the expensive fabrication process is started. This is particularly important for antennas used in space craft, missiles, etc. The full-wave analysis of microstrip antennas on coated cylinders have been performed mainly using a MoM/Green's function method in the spectral domain. In [12], the near fields and the input impedance of printed antennas were calculated by solving the electric field integral equation (EFIE) in the spectral domain via a MoM/Green's function method where they used Galerkin's MoM. They evaluated the Green's function writing the special functions (Hankel and Bessel functions) as logarithmic derivatives and calculated these logarithmic derivatives via recurrence relations and the continued fraction method so that high order Bessel or Hankel functions with large arguments can be evaluated accurately. The same method was applied to characterize infinite microstrip lines [25] and coupled microstrip lines [26] on dielectric coated cylinders, which are in fact two-dimensional (2-D) problems (the structures are infinite along the axial (z) direction). Therefore, the method described in [12] was modified for the 2-D case. The Green's function for the quasi-static model was also derived and the similarity of the functional behavior of both Green's functions was discussed in these papers. In [27], the aforementioned methods [12, 25, 26] were combined and a single algorithm which is capable of modeling microstrip elements on cylindrical substrates including high/low frequency limits, lossy materials and arbitrary thickness was presented. Furthermore, the dyadic Green's functions were converted to rapidly converging forms using some of their asymptotic behaviors to reduce the computation time.

In [28] the mutual coupling for conformal microstrip antennas is analyzed. First, a general solution to the dielectric slab problem were presented along with some numerical results. A dielectric coated cylinder problem was then treated using the eigenfunction representation of the dyadic Green's function. Finally, an alternative representation (circumferentially propagating) was derived (which is more rapidly converging for large cylinders) and a two-dimensional coupling problem was considered to illustrate this approach.

In [29] and [13], a set of vector integral equations which governs the current distribution on the conducting patches were formulated in the spectral domain and then solved using Galerkin's MoM. In [29], their concern was mainly the complex resonance frequencies (consequently the Q-factor and bandwidth) and hence they also developed an approximate formulation based on the perturbation approach which is valid for thin dielectric coatings. On the other hand, in [13], the input impedance and the radiation patterns of cylindrical-rectangular and wraparound microstrip antennas were evaluated using both the full-wave approach and single mode approximations where the latter is valid for thin coatings. They also considered the effects of a probe by modeling it as a ρ -directed dipole where the curvature was neglected for its self-term evaluation. This is a reasonable approximation for cylinders whose radius of curvature is large compared to the thickness of the substrate. At this point, it is worthwhile to mention that their Galerkin's method is not exactly a Galerkin's method in the usual sense due to the slight difference in the form of the expansion and testing basis functions which they used.

Wong et al. [30–32] reported the analysis of more complicated geometries again using a MoM/Green’s function approach where the EFIE was formulated in spectral domain and solved with Galerkin’s MoM. In [30], they studied the complex resonant frequencies and Q-factor for superstrate-loaded cylindrical-rectangular structures where the emphasis was given to the effects of superstrate thickness and permittivity on the complex resonant frequencies. Also, the numerical convergence of their method based on the selection of basis functions was discussed. Similar discussions were reported in [31] for a microstrip structure where the dielectric layer (substrate) is separated from the PEC cylinder with a thin air-gap. Finally, they applied this method to analyze microstrip lines mounted on the inner surface of a cylindrical substrate that is enclosed by a cylindrical ground surface [32] and observed strong dispersive behavior.

Tam et al. [33] analyzed a two-element microstrip arrays on dielectric coated conducting cylinders using the same method. In [34–38] the EFIE-MoM approach was used in the spectral domain to analyze various printed circuit elements on dielectric coated circular cylinders. Among them, [38] analyzed the mutual coupling between two probe-fed cylindrical-triangular microstrip antennas using a single basis function for the unknown surface current density on each patch. Pan and Wong [38] justified the sufficiency of using a single basis function based on the fact that the resonant frequency of the fundamental mode of the triangle patch is far below the other higher-order modes. The probe feed was modeled as a line source of unit amplitude pointing in the ρ -direction and extending from the inner radius to the outer radius.

Kildal et al. [39] followed a slightly different approach to analyze nearly cylindrical antennas and scattering problems using a spectrum of 2-D solutions. They assumed the cylindrical parts of the geometry to be infinitely long (in the z -direction) and

the non cylindrical parts such as dipoles/apertures/slots are replaced by equivalent current sources. By doing that a three dimensional (3-D) field problem was obtained with 2-D boundary conditions, and investigated in the spectral domain as a 2-D problem. They calculated the radiation patterns directly from the 2-D solutions, but 3-D solutions are required to find the input impedances and current distributions of the radiating elements. They accomplished this task using an inverse Fourier transform technique. Their method was also used in [40] to calculate the radiation patterns of a dielectric coated cylinder and a grounded dielectric cylinder with rectangular cross section. Different applications as well as a brief description of this method was also reported in [41].

Jin et al. [42] presented a reciprocity based approach to calculate the radiation patterns of microstrip antennas and arrays on a cylindrical body having arbitrary cross-section. Since the microstrip elements are highly resonant structures, the shape of the host body should have little effect on the input impedance or current distribution of the antenna elements, but it can change the radiation patterns significantly. Therefore, they characterized the microstrip antennas/arrays using FEM assuming that they were placed on an infinitely large ground plane. Then, the radiation patterns were calculated using the reciprocity theorem in conjunction with a 2-D MoM solution for scattering computations. A very similar approach for the radiation patterns of patch antennas on dielectric coated circular cylinders was also presented in [43].

Hall et al. [44, 45] presented a mixed potential integral equation (MPIE) approach to analyze conformal microstrip antennas. Although this method is more complicated than the EFIE approach, the mixed potential Green's functions are less singular in

the space domain. Using this approach, they analyzed circularly-polarized cylindrical wraparound microstrip antennas and arrays.

Recently, Loffler et al. [46] designed and analyzed a conformal aperture coupled microstrip phased array on a cylindrical surface in the spectral domain using a special Green's function as the kernel of the integral equation. The corresponding integral equation was solved via MoM (Galerkin) with entire domain basis functions.

In addition to the aforementioned references, dyadic Green's functions involving vector wave functions [47–49] in the spectral domain combined with MoM and numerical methods such as the Finite Element-Boundary Integral (FE-BI) method [50] and FDTD [51] are the other approaches used to solve cylindrical microstrip antennas and arrays.

Regarding the construction of Green's functions, a significant amount of work has been done for cylindrical single or multilayer structures. The radially propagating eigenfunction series representation of the Green's functions exhibit poor convergence at high frequencies, although this representation was widely used in most of the MoM/Green's functions solutions. Naishadham and Felsen [52] presented an eigenfunction solution for a cylindrical substrate-superstrate layered medium which exhibits rapid convergence at high frequencies. They investigated the effects of the curvature as well as the electrical parameters of the substrate and superstrate on the solution of the dispersion equation associated with the Green's function for the waves guided tangentially along the outer layer (superstrate). They classified the waves as leaky, creeping or trapped depending on the pole locations (and hence their phase velocities) which were found from the dispersion equation via Davidenko's method. Similar studies for thin or thick dielectric coated circular cylinders were done for a

line source excitation in [53–55], which reduces the problem into 2-D. Kim et al.[56] developed a 2-D UTD-based Green’s function for the first time to solve the scattering by a circular cylinder with a thin lossy coating. Their solution employed the geometrical optics (GO) solution in the lit region, and the usual creeping wave format in the shadow region. A universal transition function was developed for the transition region (the region around the shadow boundaries) where the pure ray-optical solution fails.

Pearson [57] developed an asymptotic expression for the fields produced by a point source in the presence of an infinitely long multilayer coated cylinder which is only valid in the shadow region. In his solution, the diffracted waves were interpreted in a ray-optic format different from UTD. This work is actually an extension of his previous work [58] where an exact field representation was constructed as an integral over longitudinally and azimuthally propagating waves.

Marin et al. [59] presented both spectral and space domain formulations for the calculation of the surface fields created by a current distribution, and mutual coupling between two current distributions on coated circular cylinders. In the spectral domain solution, the Green’s functions derived by [12] were used but evaluated differently. Closed form approximate expressions were obtained for the special functions using two term Debye approximations whereas in the space domain solution, they obtained an approximate Green’s function using approximations which are commonly used for the planar cases. However, their space domain results are accurate only for large cylinders and for the coupling between the current distributions when they are not far from each other along the surface of the coated cylinder.

Tokgoz [60] developed an efficient two-step technique to obtain the space domain Green's functions due to a tangential electric/magnetic dipole in an arbitrary layer of a cylindrical stratified medium. First, the fields in the spectral domain were evaluated. Then, they were approximated in terms of complex exponentials using the Generalized Pencil of Function (GPOF) method and transformed into the space domain analytically in two consecutive steps.

Munk [4], heuristically derived UTD-based Green's functions for the surface fields on a material coated arbitrarily convex conducting surfaces generalizing the asymptotic results of a coated circular cylinder and a coated sphere. His work [4] includes surface fields up to order $O(1/(k_0 s)^3)$ where k_0 is the free-space propagation constant and s is the arc length of the geodesic ray path on the surface from the source to the observation point. The scheme followed in [4] is an extension of the method developed in [3] and [9] for metallic surfaces. That scheme is a two-step procedure where the leading term ($O(1/k_0 s)$) of the potentials A_z and F_z are first developed and the fields are then obtained by taking the second derivative of A_z and F_z , dropping terms higher than $O(1/(k_0 s)^3)$ and $O(1/d)$ where d is the radius of the cylinder. That procedure becomes quite complex for dielectric coated surfaces. The surface wave solution in [4] were implemented in [5] and [6] using a combination of Olver's uniform representation and a single term Debye approximation for the logarithmic derivative of the Hankel functions. Numerical results showed that reasonable results can be obtained for large separations if only terms of $O(1/(k_0 s))$ are included. If terms up to $O(1/(k_0 s)^3)$ are used, the results are not as accurate. Furthermore, as mentioned before, the solutions presented in [4], [5] and [6] are not valid in the paraxial regions.

This dissertation is organized as follows. In Chapter 2, the SDP representation of the special Green's function is presented for both tangential and normal components along with the numerical evaluation of some special functions and slowly decaying oscillatory integrals. Some numerical results illustrating the accuracy of this method are also presented in this chapter. Chapter 3 deals with the approximate space domain Green's function representation which is valid along the paraxial region. Calculation of the surface fields and some numerical results are also given to assess the accuracy of this method. Furthermore, some minor modifications which make this representation valid away from the paraxial region are pointed out. Note that, unlike the previous chapter, only the tangential components are of interest in this chapter. The Green's function representations derived in Chapter 2 and Chapter 3, together with the planar approximations, are combined with the MoM in Chapter 4 to analyze the input impedance of a single rectangular patch antenna as well as the mutual coupling between two identical patches on dielectric coated cylinders with different parameters. Some calculated results are compared with available results found in the literature. Finally, a brief conclusion is presented in Chapter 5.

There are five appendices in this dissertation. Appendix A discusses how the limiting case of the SDP integral representation of the surface fields for a dielectric coated circular cylinder reduces to the leading term of the UTD-based Green's function. The limiting values of the SDP representation of the surface fields for large τ values (which form the tail expressions for the integrals) are explicitly given in Appendix B. Appendix C briefly reviews the approximation of periodic functions using Fourier series. Appendix D explains how the $G_{\phi\phi}(\zeta, \psi)$ component, which is used in Chapter 3, is represented as a combination of planar and curvature correction terms.

Finally, explicit expressions for the special functions used to calculate the approximate space domain Green's function representations valid in the paraxial region are given in Appendix E.

CHAPTER 2

Efficient Computation of Surface Fields Excited on a Dielectric Coated Circular Cylinder

2.1 Introduction

In this chapter, an efficient and accurate method to evaluate the surface fields (away from the paraxial region) excited by an electric current source located on the surface of a dielectric coated electrically large circular cylinder is presented. The method is based on obtaining a circumferentially propagating (ϕ -propagating) series representation of the appropriate Green's function from its radially propagating (ρ -propagating) counterpart, and its efficient numerical evaluation along a steepest descent path (SDP) on which the integrand decays most rapidly. In Section 2.2, the eigenfunction series representation (radially propagating) of the surface fields created by a current distribution on the surface of the coating is given. Section 2.3 presents the formulation of the SDP integral representation of the special Green's function for the aforementioned cylinder along with the deformation of the contour of integration which is required to obtain the SDP integral representation. Numerical evaluation of several special functions which involve a combination of Bessel and Hankel functions is presented in Section 2.4 where they are mostly expressed in terms of closed form

analytic expressions that involve some elementary functions. Numerical evaluation of the integrals is presented in Section 2.5. As will be mentioned in this section, a direct integration along the SDP can be performed efficiently using Gauss-Hermite quadrature approach. The number of terms required in this algorithm decreases with the distance between the source and field points, making it suitable for the analysis of large cylinders. It is important to note that the limiting case (large separations) of this method would be the saddle point integration considered in [5] and [6]. Finally, numerical results which illustrate the accuracy of this method with the traditional eigenfunction solution is presented in Section 2.6.

2.2 Development of an Eigenfunction Series Representation of the Surface Fields due to a Current Distribution on the Surface of a Coated Cylinder

A Fourier transform pair for the electric and magnetic fields can be defined as follows:

$$\left\{ \begin{array}{c} \vec{e} \\ \vec{h} \end{array} \right\} \equiv \int_{-\infty}^{\infty} dz \left\{ \begin{array}{c} \vec{E} \\ \vec{H} \end{array} \right\} e^{jk_z z} \quad (2.1)$$

and

$$\left\{ \begin{array}{c} \vec{E} \\ \vec{H} \end{array} \right\} \equiv \frac{1}{2\pi} \int_{-\infty}^{\infty} dk_z \left\{ \begin{array}{c} \vec{e} \\ \vec{h} \end{array} \right\} e^{-jk_z z} \quad (2.2)$$

Taking the Fourier transform of the source free wave equation in free space and solving it in the spectral domain for e_z and h_z , these components (e_z and h_z) may be expressed in terms of the Bessel and Hankel functions as

$$e_z^i = \sum_{n=-\infty}^{\infty} e^{-jn\phi} [a_n^i J_n(k_{ti}\rho) + b_n^i H_n^2(k_{ti}\rho)] \quad (2.3)$$

and

$$h_z^i = \sum_{n=-\infty}^{\infty} e^{-jn\phi} [c_n^i J_n(k_{ti}\rho) + d_n^i H_n^2(k_{ti}\rho)] . \quad (2.4)$$

In (2.3) and (2.4), a_n^i , b_n^i , c_n^i and d_n^i are the unknown coefficients to be determined from the boundary conditions. The superscript $i = 1$ indicates the dielectric region ($a < \rho < d$), whereas $i = 0$ is the free-space region ($\rho > d$). The free-space transverse propagation constant k_{t0} is defined in terms of the free-space propagation constant k_0 as

$$k_{t0}^2 = k_0^2 - k_z^2 ; \quad k_0 = \omega \sqrt{\epsilon_0 \mu_0} \quad (2.5)$$

whereas the transverse propagation constant inside the dielectric region k_{t1} is defined in terms of the propagation constant inside the dielectric region k_1 as

$$k_{t1}^2 = k_1^2 - k_z^2 ; \quad k_1 = \omega \sqrt{\epsilon_1 \mu_1} . \quad (2.6)$$

Using (2.3) and (2.4) in the Maxwell's curl equations, the ϕ and ρ components of the transformed fields can be obtained from e_z^i and h_z^i as

$$e_\rho^i = -\frac{jk_i Z_i}{k_{ti}^2} \left(\frac{1}{\rho} \frac{\partial h_z^i}{\partial \phi} + \frac{k_z Y_i}{k_i} \frac{\partial e_z^i}{\partial \rho} \right) \quad (2.7)$$

$$h_\rho^i = \frac{jk_i Y_i}{k_{ti}^2} \left(\frac{1}{\rho} \frac{\partial e_z^i}{\partial \phi} - \frac{k_z Z_i}{k_i} \frac{\partial h_z^i}{\partial \rho} \right) \quad (2.8)$$

$$e_\phi^i = -\frac{jZ_i}{k_{ti}^2} \left(\frac{k_z Y_i}{\rho} \frac{\partial e_z^i}{\partial \phi} - k_i \frac{\partial h_z^i}{\partial \rho} \right) \quad (2.9)$$

and

$$h_\phi^i = -\frac{jY_i}{k_{ti}^2} \left(\frac{k_z Z_i}{\rho} \frac{\partial h_z^i}{\partial \phi} + k_i \frac{\partial e_z^i}{\partial \rho} \right) \quad (2.10)$$

where Z_i and Y_i represent the intrinsic impedance and admittance, respectively, of the region i , namely,

$$Z_i = \sqrt{\frac{\mu_i}{\epsilon_i}} ; \quad Y_i = \sqrt{\frac{\epsilon_i}{\mu_i}} . \quad (2.11)$$

Now, consider an electric surface current source given by

$$\vec{J} = \vec{P}_e \frac{\delta(\phi - \phi')\delta(z - z')}{\rho'} \quad (2.12)$$

where

$$\vec{P}_e = P_e^z \hat{z} + P_e^\phi \hat{\phi} \quad (2.13)$$

located on the surface of a dielectric coated circular cylinder ($\rho' = d$) whose geometry is given in Figure 2.1. The cylindrical Fourier transform of this current distribution is given by [61],

$$\tilde{\vec{J}}_e = \frac{\vec{P}_e}{2\pi d} e^{jk_z z'} e^{jn\phi'} . \quad (2.14)$$

Enforcing the boundary conditions on the coated cylinder shown in Figure 2.1, namely, at $\rho = a$ (zero tangential electric field at the conducting surface) and at $\rho = d$ (continuity of the tangential fields) and applying the radiation condition as $\rho \rightarrow \infty$, the surface fields at $\rho = d$, excited by a point source given by (2.12), can be written as (after taking the inverse Fourier transform of the transformed fields (2.2))

$$\vec{E}(\phi, z) = \frac{1}{2\pi} \sum_{n=-\infty}^{\infty} e^{-jn(\phi-\phi')} \int_{-\infty}^{\infty} \frac{\overline{\overline{G}} \cdot \vec{P}_e}{2\pi d} e^{-jk_z(z-z')} dk_z \quad (2.15)$$

where

$$\overline{\overline{G}} = \overline{\overline{G}}(n, k_z, \rho = \rho' = d) = \begin{bmatrix} G_{\rho\rho} & G_{\rho\phi} & G_{\rho z} \\ G_{\phi\rho} & G_{\phi\phi} & G_{\phi z} \\ G_{z\rho} & G_{z\phi} & G_{zz} \end{bmatrix} \quad (2.16)$$

which is the radially propagating series representation of the appropriate dyadic Green's function.

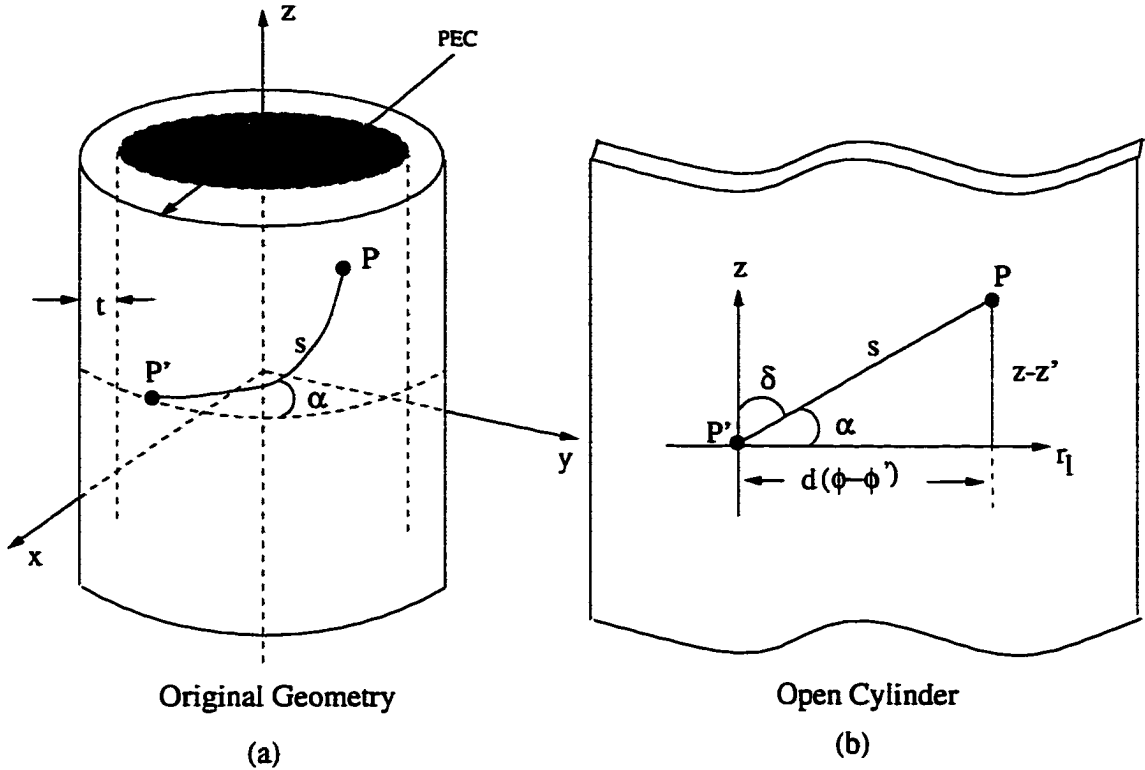


Figure 2.1: The geometry of a cylinder with inner radius a and outer radius d .

2.2.1 Tangential Components

Most of the MoM based conformal antenna analysis require the use of tangential components of the surface fields due to the tangential current sources. Therefore, the ρ -related components of $\bar{\bar{G}}$ (for example $G_{\rho\phi}$ or $G_{z\rho}$ which might be important for some applications involving an excitation via probe) are considered separately in Section 2.2.2. Thus, $\bar{\bar{G}}_{tan}$ obtained from (2.16), is defined as

$$\bar{\bar{G}}_{tan} = \begin{bmatrix} G_{\phi\phi} & G_{\phi z} \\ G_{z\phi} & G_{zz} \end{bmatrix} \quad (2.17)$$

whose components for source and observation points on the surface ($\rho = \rho' = d$) are explicitly given by

$$G_{\phi\phi} = \frac{jZ_0}{k_0} \left\{ \left[\frac{k_0^2 k_{t0}}{k_{tl}^2} \right] \frac{R_n C_n^e T_m}{T} - k_{t0} \frac{R_n T_c^2}{(\epsilon_r - 1)T} - \left[\frac{nk_z}{dk_{tl}} \right]^2 \frac{(C_n^e - k_{t0} R_n)}{T} \right\} \quad (2.18a)$$

$$G_{\phi z} = \frac{jZ_0}{k_0} \left[\frac{nk_z}{d} \frac{k_{t0}^2}{k_{tl}^2} \right] \frac{(C_n^e - k_{t0} R_n)}{T} \quad (2.18b)$$

$$G_{z\phi} = G_{\phi z}, \text{ and} \quad (2.18c)$$

$$G_{zz} = \frac{jZ_0}{k_0} k_{t0}^2 \frac{T_e}{T} \quad (2.18d)$$

where

$$T = T_e T_m - T_c^2 \quad (2.19)$$

with

$$T_e = k_{t0} R_n - \frac{k_{t0}^2}{k_{tl}^2} C_n^e \quad (2.20a)$$

$$T_m = k_{t0} R_n - \epsilon_r \frac{k_{t0}^2}{k_{tl}^2} C_n^m \quad (2.20b)$$

$$T_c = \frac{k_0 (\epsilon_r - 1)}{k_{tl}^2} \frac{nk_z}{d} \quad (2.20c)$$

and

$$R_n = \frac{H_n^{(2)\prime}(k_{t0} d)}{H_n^{(2)}(k_{t0} d)} \quad (2.21)$$

$$C_n^e = k_{t1} \frac{J'_n(k_{t1}a)Y'_n(k_{t1}d) - J'_n(k_{t1}d)Y'_n(k_{t1}a)}{J'_n(k_{t1}a)Y_n(k_{t1}d) - J_n(k_{t1}d)Y'_n(k_{t1}a)} \quad (2.22a)$$

$$C_n^m = k_{t1} \frac{J_n(k_{t1}a)Y'_n(k_{t1}d) - J'_n(k_{t1}d)Y_n(k_{t1}a)}{J_n(k_{t1}a)Y_n(k_{t1}d) - J_n(k_{t1}d)Y'_n(k_{t1}a)} \quad (2.22b)$$

where ' denotes the derivatives with respect to the argument.

2.2.2 Normal Components

As previously mentioned, cylindrical antennas excited via a probe require the ρ -related components of the dyadic Green's function to determine the incident field as well as the input impedance.

As a first step, the ρ -component of the electric field inside the coating due to a source given by (2.12) is determined. Using (2.3) and (2.4) together with (2.7) for the case $i = 1$ (i.e. inside the dielectric), the ρ -component of the surface field can be written as

$$\vec{E}(\rho, \phi, z) = \frac{1}{2\pi} \sum_{n=-\infty}^{\infty} e^{-jn(\phi-\phi')} \int_{-\infty}^{\infty} \frac{\bar{\bar{G}}_{\rho} \cdot \vec{P}_e}{2\pi d} e^{-jk_z(z-z')} dk_z \quad (2.23)$$

where

$$\bar{\bar{G}}_{\rho} = G_{\rho\phi} \hat{\rho} \hat{\phi} + G_{\rho z} \hat{\rho} \hat{z} \quad (2.24)$$

whose components for source points on the surface ($\rho' = d$) and observation points inside the coating $a < \rho < d$ are explicitly given by

$$\begin{aligned}
G_{\rho\phi} &= \frac{jZ_0}{k_0} \left\{ \frac{jn}{\rho} \left[\frac{T_c^2}{\epsilon_r - 1} - \frac{k_0^2 k_{t0} R_n T_m}{k_{t1}^2} \right] \frac{C_n^{pr1}}{T} \right. \\
&\quad \left. + \frac{jk_z}{T} \left(\frac{nk_z}{dk_{t1}^2} \right) \left(\frac{k_{t0}^2}{k_{t1}^2} \right) (C_n^e - k_{t0} R_n) k_{t1} C_n^{pr2} \right\}, \tag{2.25}
\end{aligned}$$

and

$$G_{\rho z} = \frac{jZ_0}{k_0} \left\{ \frac{-jn}{\rho} \left(\frac{k_{t0}^2}{k_{t1}^2} \right) \frac{k_0 T_c C_n^{pr1}}{T} + \frac{jk_z}{T} \left(\frac{k_{t0}^2}{k_{t1}^2} \right) T_e k_{t1} C_n^{pr2} \right\} \tag{2.26}$$

where

$$C_n^{pr1} = \frac{J'_n(k_{t1}a)Y_n(k_{t1}\rho) - J_n(k_{t1}\rho)Y'_n(k_{t1}a)}{J'_n(k_{t1}a)Y_n(k_{t1}d) - J_n(k_{t1}d)Y'_n(k_{t1}a)} \tag{2.27}$$

and

$$C_n^{pr2} = \frac{J_n(k_{t1}a)Y'_n(k_{t1}\rho) - J'_n(k_{t1}\rho)Y_n(k_{t1}a)}{J_n(k_{t1}a)Y_n(k_{t1}d) - J_n(k_{t1}d)Y'_n(k_{t1}a)} \tag{2.28}$$

with other functions being the same as given by (2.19)-(2.22).

Next, the tangential components of the electric fields \vec{E}_{tan}^{en} at $\rho = d$, generated by a normal point electric current $\vec{J} = \hat{\rho} P_e^\rho \delta(|\hat{r} - \hat{r}'|)$ embedded in the dielectric coating of the coated conducting circular cylinder ($a < \rho' < d$), can be developed using the reciprocity theorem as discussed in [4]. Making use of the general reciprocity relationship [11]

$$\int_{V_1} (\vec{E}_2 \cdot \vec{J}_1 - \vec{H}_2 \cdot \vec{M}_1) dv = \int_{V_2} (\vec{E}_1 \cdot \vec{J}_2 - \vec{H}_1 \cdot \vec{M}_2) dv \tag{2.29}$$

one may write

$$P_e^\rho \hat{\rho} \cdot \hat{\rho} E_\rho(\rho, \phi, z) \Big|_{at P_e^\rho} = \vec{E}_{tan}^{en} \cdot \vec{P}^e \Big|_{at \vec{P}_e} \tag{2.30}$$

where $E_\rho(\rho, \phi, z) \Big|_{at P_e^\rho}$ is given by (2.23). It should be noted at this point that during the mutual coupling calculations (between the tangential and normal components), let us set $\rho = d$ and numerically integrate on ρ' the Green's function components $G_{\phi\rho}$ and $G_{z\rho}$ over the probe of constant current and thickness t_h , whereas let $\rho' = d$ and numerically integrate on ρ the components $G_{\rho\phi}$ and $G_{\rho z}$ over the probe height. A similar approach was performed in [62] for the analysis of microstrip patches which are fed via a probe.

2.2.3 Numerical Considerations

Now, by using (2.15) together with (2.18), (2.25) and (2.26) one can calculate the surface fields due to any given current distribution. However, there are certain numerical problems which should be addressed.

a) Limiting values: As shown in [59], the series in (2.15) is not absolutely convergent for the Green's function components given by (2.18). For example, one finds that

$$\lim_{n \rightarrow \infty} G_{\phi\phi}(n, k_z) = C_1 n \quad (2.31)$$

$$\lim_{(n \text{ or } k_z) \rightarrow \infty} G_{\phi z}(n, k_z) = C_2 \quad (2.32)$$

$$\lim_{k_z \rightarrow \infty} G_{zz}(n, k_z) = C_3 k_z \quad (2.33)$$

$$\lim_{k_z \rightarrow \infty} G_{\rho z}(n, k_z) = C_4 k_z \quad (2.34)$$

and

$$\lim_{n \rightarrow \infty} G_{\rho\phi}(n, k_z) = C_5 n \quad (2.35)$$

where C_i is a certain constant. This problem can be alleviated to some extent by using carefully chosen basis functions which show a spectral decay of at least $1/n^2$ (or $1/k_z^2$) in a moment method based solution, however, the product of the Green's function and basis function is still poorly convergent.

b) Numerical Evaluation of Bessel and Hankel Functions: Expressions for the Green's function involve Bessel and Hankel functions along with their derivatives, and their computation for large values of n is not a trivial matter due to the numerical instabilities which occur for large order and argument of these functions. In the following sections, an alternative representation of these Green's function components are given which yield a much faster convergence. Moreover, some closed form expressions for (2.21) and (2.22) are mentioned in order to avoid the aforementioned instabilities.

2.3 Development of Steepest Descent Path Integral Representation for the Surface Fields

The starting point of the SDP integral representation of the surface fields is to convert the slowly convergent radially propagating (ρ -propagating) series representation of the Green's function into a rapidly convergent circumferentially propagating series representation using the Watson transform [63] (i.e. the series in ϕ is converted into a complex integral), namely,

$$E_l(\phi, z) = \frac{1}{4\pi^2 d} \int_{-\infty}^{\infty} dk_z e^{-jk_z(z-z')} \left\{ \int_{-\infty-j\epsilon}^{\infty-j\epsilon} G_{l,u}(k_z, \nu) P_e^u \right. \\ \left(\sum_{p=-\infty}^{\infty} e^{-j\nu[(\phi-\phi')-2\pi p]} \right) d\nu \right\} \quad (2.36)$$

where \hat{u} represents the source orientation, \hat{l} represents the field orientation, ϵ is a small positive number and all the functions are defined as before with n replaced by ν . Figure 2.2 shows the contour used to evaluate (2.36) in the complex ν -domain.

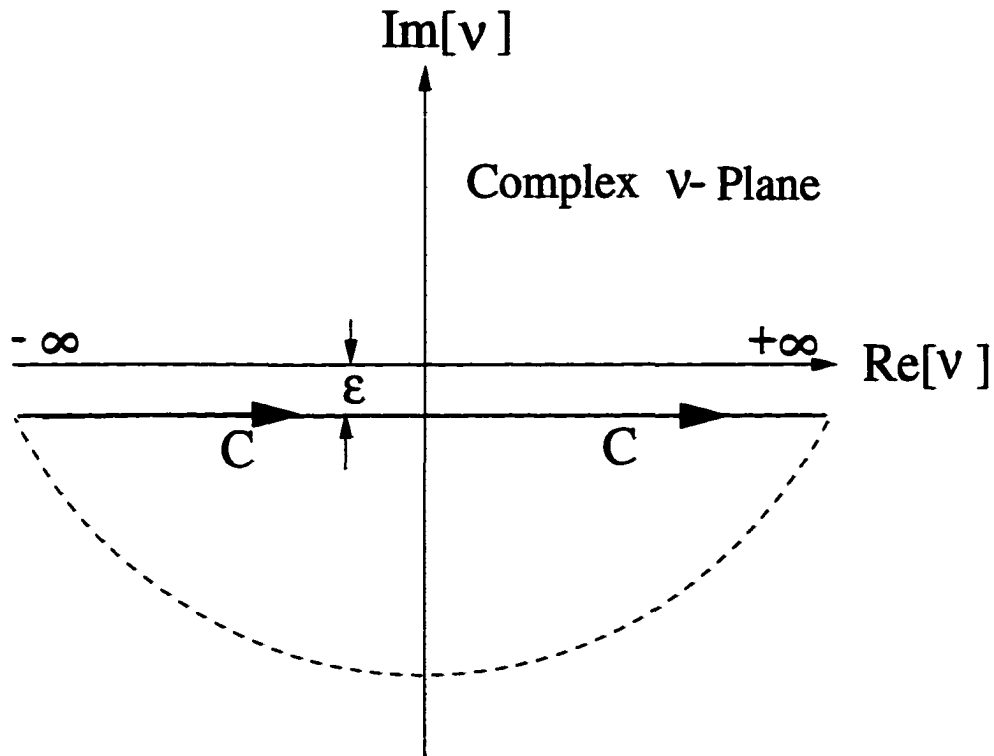


Figure 2.2: Contour used to evaluate (2.36) in the complex ν -plane

Equation (2.36) represents an infinite number of propagating modes in the azimuthal (ϕ) direction. Moreover, the $e^{-j\nu(\phi-\phi')}$ term may be interpreted as the wave propagating in the $+ \phi$ direction, while the term $e^{-j\nu[2\pi-(\phi-\phi')]}$ is associated with the wave propagating in the $- \phi$ direction. Provided that the cylinder is electrically large (a few wavelengths in diameter), it is enough to retain the $p = 0$ term since the $|p| > 0$ terms are associated with multiple wave encirclements. However, for relatively small

cylinders and different material coatings, $|p| = 1$ or more wave encirclements have to be added in the solution to increase the accuracy of field calculations. The effect of multiple wave encirclements become visible for large $\phi - \phi'$ values. Restricting our attention to the cases in which the leading term ($p = 0$) is dominant and provides enough accuracy in (2.36), it can be rewritten as

$$E_t(\phi, z) \approx \frac{1}{4\pi^2 d} \int_{-\infty}^{\infty} dk_z e^{-jk_z(z-z')} \left\{ \int_{-\infty-j\epsilon}^{\infty-j\epsilon} G_{tu}(k_z, \nu) P_e^u e^{-j\nu(\phi-\phi')} d\nu \right\}. \quad (2.37)$$

Although (2.37) converges faster than (2.15) for electrically large cylinders, computation of the surface fields can be performed more efficiently if the original contour of the ϕ -propagating representation of the Green's function is deformed into its SDP on which the integrand decays most rapidly. Therefore, making the substitution originally suggested by Fock [64]

$$\nu = k_{t0}d + m_t \tau \quad (2.38)$$

in which

$$m_t = \left(\frac{k_{t0}d}{2} \right)^{\frac{1}{3}} \quad (2.39)$$

and employing the usual polar transformations

$$k_z = k_0 \sin \psi, \text{ and} \quad (2.40a)$$

$$k_{t0} = k_0 \cos \psi \quad (2.40b)$$

along with the geometrical relations based on Figure 2.1, namely

$$z - z' = s \sin \alpha, \text{ and} \quad (2.41a)$$

$$d(\phi - \phi') = s \cos \alpha \quad (2.41b)$$

one gets

$$E_l(\alpha, s) \approx \frac{1}{4\pi^2 d} \int_{C_\Psi} d\psi k_0 \cos \psi e^{-jk_0 s \sin \psi \sin \alpha} \\ \left(\int_{C_\tau} G_{lu}(\psi, \tau) P_e^u e^{-jk_0 s \cos \psi \cos \alpha} e^{-jm_t \tau (\phi - \phi')} m_t d\tau \right) \quad (2.42)$$

where s is the arc length of the geodesic path on the surface of the coating from the source to the observation point, α is the angle between the ray path and the axis r_l as depicted in Figure 2.1 and C_τ is the integration contour in the τ -domain which will be defined in Section 2.5. Furthermore, (2.42) can be written in the form of

$$E_l(\alpha, s) \approx \frac{1}{4\pi^2 d} \int_{C_{SDP}} e^{k_0 s f(\psi)} F(\psi) d\psi \quad (2.43)$$

with

$$f(\psi) = -j \cos(\alpha - \psi) \quad (2.44)$$

and

$$F(\psi) = k_0 \cos \psi \int_{C_\tau} m_t G_{lu}(\psi, \tau) P_e^u e^{-j\xi \tau} d\tau \quad (2.45)$$

where

$$\xi = m_t(\phi - \phi') \quad . \quad (2.46)$$

Figure 2.3 shows the contour of integration C_Ψ (with end points at infinity) along with the steepest descend path contour in the complex Ψ -plane. Now, consider the integral (2.43) which is in the proper canonical form to evaluate it asymptotically. It has been shown in [65] and [66], that the point(s) where the maximum contribution to the integral occurs are “saddle” or “stationary points” of the function $f(\psi)$, obtained

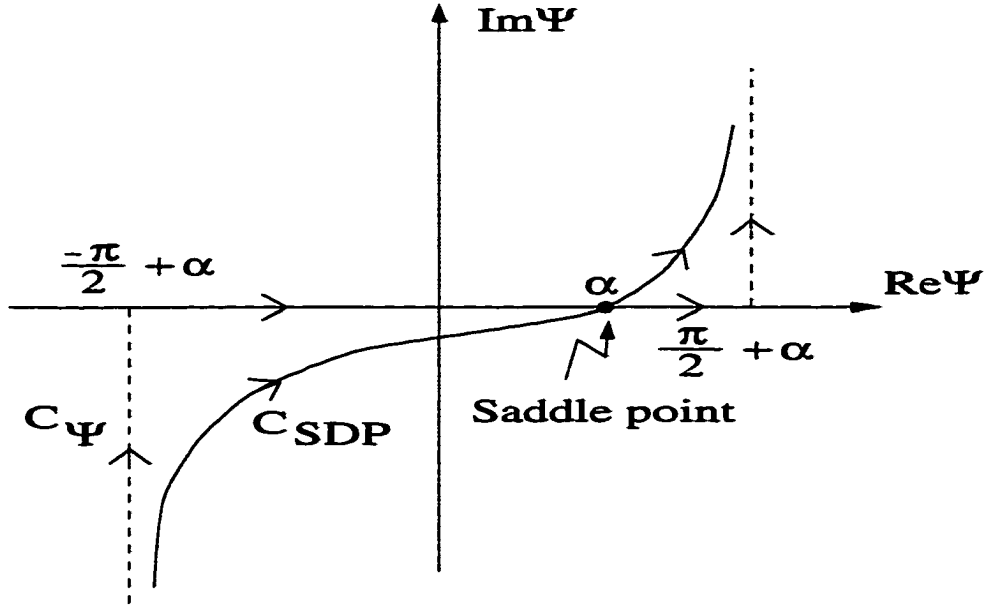


Figure 2.3: Steepest Descend Path (SDP) Contour.

by setting the first derivative of $f(\psi)$ to zero. Thus, taking the first derivative of $f(\psi)$ with respect to ψ and setting it to zero yields $\psi_s = \alpha$, where ψ_s is an isolated first-order saddle point ([65]). To evaluate (2.43), let us use a pertinent transformation from the Ψ to the t domain, namely,

$$f(\psi) = f(\psi_s) - \frac{t^2}{k_0 s} \quad (2.47)$$

with

$$G(t) = F(\psi) \frac{d\psi}{dt} \quad (2.48)$$

such that the SDP in the complex Ψ -plane is mapped onto the real axis in the complex t -plane, whereas the saddle point ψ_s is mapped to the origin of the t -plane ($t = 0$). Using (2.47), the relation between ψ and t , and an expression for $\frac{d\psi}{dt}$ can be obtained

as follows:

$$\psi(t) = \alpha - 2 \arcsin \left(\frac{t e^{j\pi/4}}{\sqrt{2} \sqrt{k_0 s}} \right) \quad (2.49)$$

$$\frac{d\psi}{dt} = \frac{\sqrt{2} e^{j3\pi/4}}{\sqrt{k_0 s} \cos(\frac{\alpha-\psi(t)}{2})} \quad (2.50)$$

Substituting (2.47) and (2.48) into (2.43) and making use of (2.49) and (2.50), the surface fields can be expressed as

$$E_l(\alpha, s) \approx \frac{\sqrt{2} e^{j3\pi/4}}{4\pi^2 d} \frac{e^{-jk_0 s}}{\sqrt{k_0 s}} \int_{-\infty}^{\infty} dt e^{-t^2} \bar{F}(\alpha, s, t) \quad (2.51)$$

with

$$\bar{F}(\alpha, s, t) = \frac{k_0 \cos \psi(t)}{\cos(\frac{\alpha-\psi(t)}{2})} \int_{C_\tau(t)} G_{lu}(\tau, t) P_e^u m_t e^{-j\xi\tau} d\tau \quad . \quad (2.52)$$

As seen in (2.52), the integration contour in the complex τ -domain is a function of t . This will be explained in detail in Section 2.5.

Finally, substituting the Green's function components into (2.52), the following expressions can be obtained for the surface fields :

$$E_\phi(\alpha, s) \approx \frac{\sqrt{2} e^{j3\pi/4}}{4\pi^2 d} \frac{e^{-jk_0 s}}{\sqrt{k_0 s}} \int_{-\infty}^{\infty} dt e^{-t^2} \frac{k_0 \cos \psi(t) m_t}{\cos(\frac{\alpha-\psi(t)}{2})} \left[\int_{C_\tau(t)} (G_{\phi\phi}(\tau, t) P_e^\phi + G_{\phi z}(\tau, t) P_e^z) e^{-j\xi\tau} d\tau \right] \quad (2.53)$$

$$E_z(\alpha, s) \approx \frac{\sqrt{2} e^{j3\pi/4}}{4\pi^2 d} \frac{e^{-jk_0 s}}{\sqrt{k_0 s}} \int_{-\infty}^{\infty} dt e^{-t^2} \frac{k_0 \cos \psi(t) m_t}{\cos(\frac{\alpha-\psi(t)}{2})} \left[\int_{C_\tau(t)} (G_{z\phi}(\tau, t) P_e^\phi + G_{zz}(\tau, t) P_e^z) e^{-j\xi\tau} d\tau \right] \quad (2.54)$$

and

$$E_p(\alpha, s) \approx \frac{\sqrt{2} e^{j3\pi/4}}{4\pi^2 d} \frac{e^{-jk_0 s}}{\sqrt{k_0 s}} \int_{-\infty}^{\infty} dt e^{-t^2} \frac{k_0 \cos \psi(t) m_t}{\cos(\frac{\alpha - \psi(t)}{2})} \left[\int_{C_\tau(t)} (G_{\phi\phi}(\tau, t) P_e^\phi + G_{\rho z}(\tau, t) P_e^z) e^{-j\xi\tau} d\tau \right] \quad (2.55)$$

where $G_{\phi\phi}$, $G_{\phi z}$, $G_{z\phi}$, G_{zz} , $G_{\rho\phi}$ and $G_{\rho z}$ are explicitly given by (2.18), (2.25) and (2.26) with n replaced with ν which is related to τ by (2.38).

2.4 Numerical Evaluation of Special Functions

As mentioned in the previous section, special care must be given to the evaluation of R_n , C_n^e and C_n^m (or R_ν , C_ν^e and C_ν^m) along with C_n^{pr1} and C_n^{pr2} (C_ν^{pr1} and C_ν^{pr2}) since numerical evaluation of Bessel and Hankel functions and their derivatives is not a trivial matter. The potential problems are:

- i) Since there is not a unique representation of Bessel and Hankel functions that converges over the entire argument plane, it is common to use two or more different asymptotic expansions that converge over the different regions which should overlap each other. As an example, the Watson and Debye approximations are the most widely used nonuniform approximations to the Hankel functions valid at the regions $|\nu - z| < O(m_t)$ and $|\nu - z| > O(m_t)$, respectively, where z is the argument ($z = k_{t0}d$) and m_t is defined in (2.39). However, the overlapping region between these two approximations is not well-defined, which reveals the difficulty in deciding where to switch from one approximation to the other.
- ii) The order and argument of Bessel and Hankel functions are functions of the integration variables τ and t and may become large during the evaluation of

the integrals resulting in numerical instabilities which affect the accuracy of the solution. Furthermore, both order and argument of these functions become complex for certain τ and t values. Note that the evaluation of Bessel and Hankel functions with complex order and argument is challenging.

Here, the work done in [12] and [59] is modified and combined to build a robust method capable of handling the evaluation of these special functions for wide ranges of τ and t values.

2.4.1 Evaluation of R_ν

As in [12], the Green's function components are written in terms of the logarithmic derivative of $H_\nu^{(2)}(z)$ as seen in (2.18), namely,

$$R_\nu = \frac{H_\nu^{(2)'}(z)}{H_\nu^{(2)}(z)} \quad (2.56)$$

with $z = k_{t0}d$ and ν is given by (2.38). Instead of evaluating the Hankel functions and their derivatives separately, the ratios are evaluated directly yielding numerically stable and accurate results (possible overflow/underflow problems are suppressed). Next, these ratios are represented either by a 2-term Debye approximation or Olver's uniform representation depending on where these representations are valid and most accurate on the complex τ -plane. Debye approximations as well as Olver's uniform representations for $H_\nu^{(2)}(z)$ and $H_\nu^{(2)'}(z)$ are given in [67]. A 2-term Debye approximation for R_ν is given by

$$R_\nu \approx -\frac{j\sqrt{z^2 - \nu^2}}{z} - \frac{z}{2(z^2 - \nu^2)}, \quad (2.57)$$

whereas, Olver's uniform representation is given by

$$R_\nu \approx \frac{A'_i(x)}{A_i(x)} \frac{1}{\nu^{1/3}} \frac{e^{j\pi/3}}{\left[\frac{(z/\nu)^2 \zeta}{1 - (z/\nu)^2} \right]^{1/2}} \quad (2.58)$$

where

$$x = \zeta \nu^{2/3} e^{-j2\pi/3} \quad (2.59)$$

$$\zeta = (1.5\rho)^{2/3} \quad (2.60)$$

and

$$\rho = \ln(1 + \sqrt{1 - (z/\nu)^2}) - \ln(z/\nu) - \sqrt{1 - (z/\nu)^2} \quad (2.61)$$

where $A_i(x)$ is the Airy function and $A'_i(x)$ is its derivative with respect to x . The Airy function $A_i(x)$ and its derivative $A'_i(x)$ are calculated using different series expansions [67] depending on z . Note that use of (2.58) requires the proper choice of branches in the functions (2.59), (2.60) and (2.61) as explained in [68]. Equation (2.57) yields a very accurate result for (2.56) nearly for all z and ν values except a small region in the τ -plane ($\tau = \frac{\nu - k_{\text{tot}}}{m_t}$) where (2.58) is used. It is worthwhile to mention at this point that the first term of (2.57) can be recognized as the equation corresponding to the planar grounded dielectric slab, whereas the second term can be treated as the curvature correction term. Figure 2.4 compares (2.56) with a combination of (2.57) and (2.58) for a cylinder with $a = 3\lambda_0$, $t_h = 0.06\lambda_0$, $\epsilon_r = 3.25$ and $\alpha = 25^\circ$ where t_h is the thickness of the coating ($t_h = d - a$) as depicted in Figure 2.1. Next, Figure 2.5 shows the same comparison for a different cylinder with $a = 0.3\lambda_0$, $t_h = 0.6\lambda_0$, $\epsilon_r = 2.33$ and $\alpha = 40^\circ$. As the two figures suggest, a combination of (2.57) and

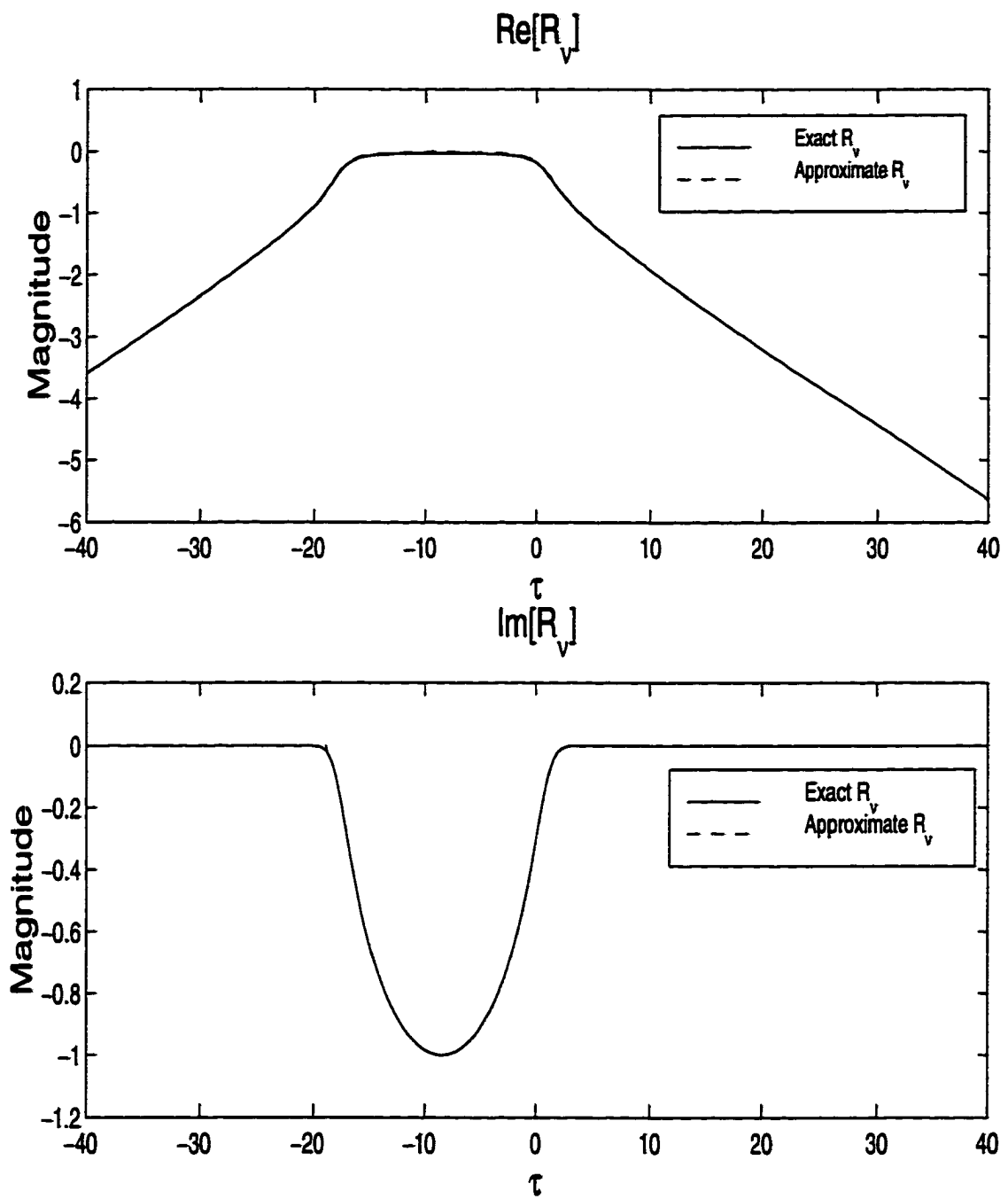


Figure 2.4: The real and imaginary parts of R_v for $a = 3\lambda_0$, $t_h = 0.06\lambda_0$, $\epsilon_r = 3.25$ and $\alpha = \psi = 25^\circ$.

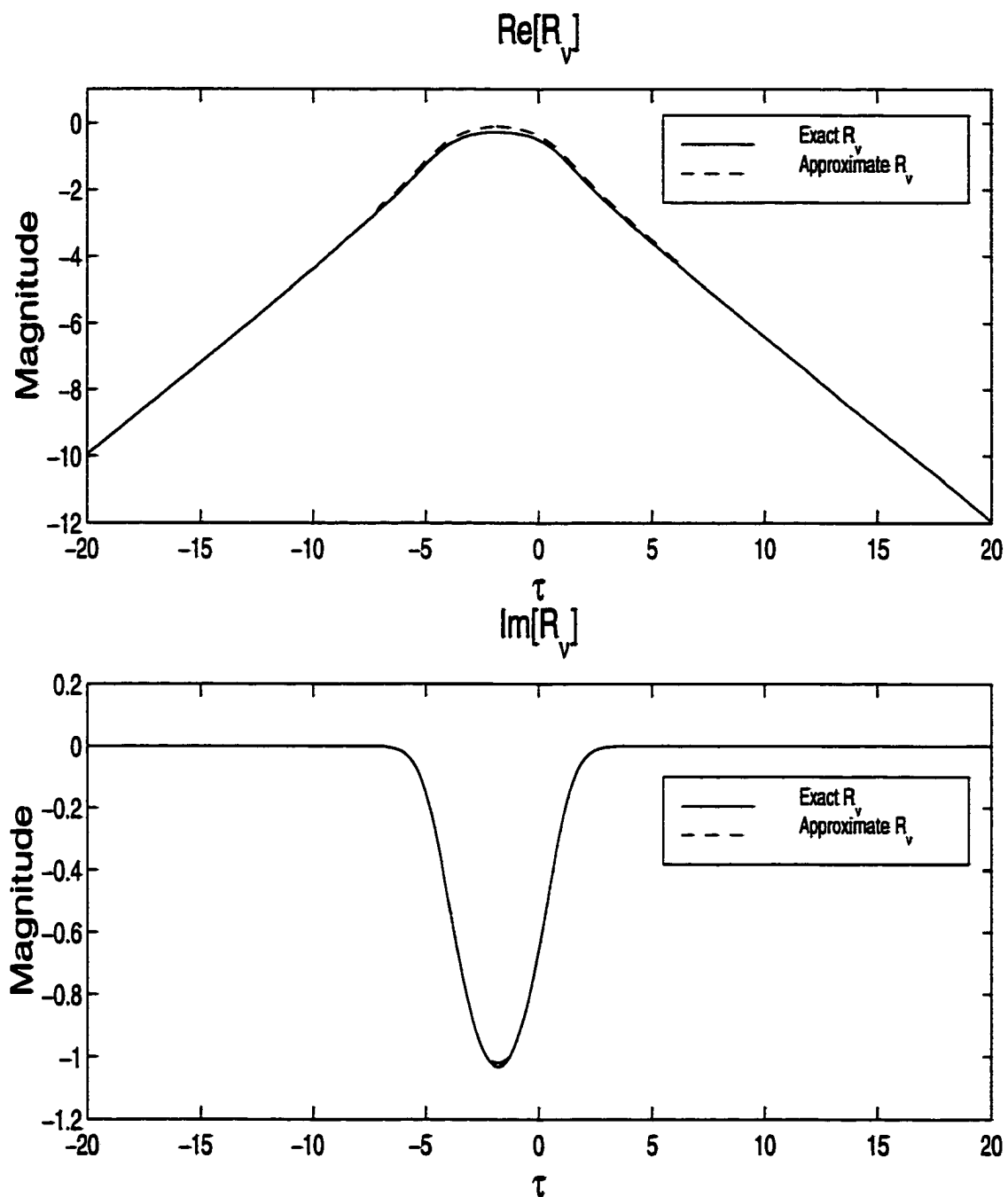


Figure 2.5: The real and imaginary parts of R_v for $a = 0.3\lambda_0$, $t_h = 0.06\lambda_0$, $\epsilon_r = 2.33$ and $\alpha = \psi = 40^\circ$.

(2.58) represents (2.56) accurately and decreases the required CPU time to calculate (2.56) tremendously. The expression in (2.57) involves only elementary functions, whereas the calculation of (2.58) is also faster than the direct calculation of (2.56) because Airy functions and their derivatives can be evaluated more efficiently than the Hankel functions and their derivatives. Furthermore, as Figure 2.5 suggests, these representations hold even for electrically small cylinders. Note that, in both figures the complex angle ψ is chosen to be α (so that ψ is real) for comparison purposes. For complex ψ values, the order and argument of Hankel functions become complex. Unfortunately, the necessary computer programs which evaluate the exact representation of Bessel and Hankel functions with complex order and argument are not available.

2.4.2 Evaluation of C_ν^m , C_ν^e , C_ν^{pr1} and C_ν^{pr2}

The functions C_ν^m and C_ν^e are evaluated as suggested in [59], namely, using a 2-term Debye approximation for the Bessel functions, yielding closed-form expressions for C_ν^m and C_ν^e . These approximations, valid for thin dielectric coatings (in particular, for C_ν^e), are given by

$$C_\nu^e \approx -\frac{\sqrt{k_{t1}^2 - (\nu/d)^2}}{\cot(t_h \sqrt{k_{t1}^2 - (\nu/d)^2})} + \frac{1}{2d} \left\{ \frac{k_{t1}^2 \tan^2(t_h \sqrt{k_{t1}^2 - (\nu/d)^2})}{k_{t1}^2 - (\nu/d)^2} + \frac{d^2(\nu/d)^2}{\cos^2(t_h \sqrt{k_{t1}^2 - (\nu/d)^2})} \right\} \quad (2.62)$$

and

$$C_\nu^m \approx \frac{\sqrt{k_{t1}^2 - (\nu/d)^2}}{\tan(t_h \sqrt{k_{t1}^2 - (\nu/d)^2})} - \frac{1}{2d} \left\{ \frac{k_{t1}^2}{k_{t1}^2 - (\nu/d)^2} - \frac{d^2(\nu/d)^2}{\sin^2(t_h \sqrt{k_{t1}^2 - (\nu/d)^2})} \right\} . \quad (2.63)$$

On the other hand, the normal components of the electric field are numerically integrated with respect to ρ (or ρ') using the trapezoidal rule. Therefore, the expressions for C_ν^{pr1} and C_ν^{pr2} are evaluated at $\rho = b$ and $\rho = a$ and can be written in terms of C_ν^m , assuming that the substrate is thin, namely

$$C_\nu^{pr1} \Big|_{\rho=b} = 1 \quad (2.64a)$$

$$C_\nu^{pr1} \Big|_{\rho=a} \approx \frac{b}{a} \quad (2.64b)$$

and

$$k_{t1} C_\nu^{pr2} \Big|_{\rho=b} = C_\nu^m \quad (2.65a)$$

$$k_{t1} C_\nu^{pr2} \Big|_{\rho=a} \approx C_\nu^m \frac{b}{a} \quad (2.65b)$$

Note that, similar thin substrate approximations were given in [13] in the process of developing the fields due to a probe excitation. As it can be seen, the above functions provide a very useful and efficient way to calculate the otherwise complicated functions since they only involve some elementary functions. As in the R_ν case, the first terms of (2.62) and (2.63) correspond to the planar grounded dielectric slab case whereas, the following terms are the curvature correction factors. Note that, there is no branch

cut associated with the square roots given in (2.62) and (2.63). Therefore, the results are independent of the sign chosen for the square roots. In Figures 2.6 and 2.7, the analytic closed form expressions given by (2.62) and (2.63) are compared with (2.22a) and (2.22b), respectively, for a cylinder with $a = 3\lambda_0$, $t_h = 0.06\lambda_0$, $\epsilon_r = 3.25$ (i.e. $t_h = 0.1082\lambda_d$ where λ_d is the wavelength inside the dielectric region given by $\lambda_0/\sqrt{\epsilon_r}$) and $\alpha = 25^\circ$. A similar comparison is given in Figures 2.8 and 2.9, respectively, for a much smaller cylinder whose parameters are given by $a = 0.3\lambda_0$, $t_h = 0.06\lambda_0$, $\epsilon_r = 2.33$ (i.e. $t_h = 0.0916\lambda_d$) and $\alpha = 40^\circ$. As in the R_ν case, the complex angle ψ is chosen to be α (so that ψ is real) in all examples for comparison purposes.

As the figures suggest, excellent agreement is achieved, resulting in a tremendous savings in CPU time. As depicted in Figures 2.6 - 2.9, the exact representations show numerical problems for relatively small τ values due to overflow/underflow problems resulting from the extremely high/small values of products of the Bessel functions. Unlike the R_ν case, there is no need for another representation for the functions C_ν^m and C_ν^e . This is an unexpected result since Debye approximations for Bessel functions and their derivatives are supposed to fail in regions where $|\nu - z| < O(m_t)$. Although each individual function may lose its accuracy in some regions of the domain, defining C_ν^m and C_ν^e as ratios of products of Bessel functions maintains the accuracy over the entire domain. At this point it should be mentioned that when the thickness of the coating is thicker than approximately $0.25\lambda_d$, numerical problems appear for C_ν^e . This problem is depicted in Figures 2.10 and 2.11 for a cylinder with $a = 3\lambda_0$ and the angle α is selected as 25° . For the first example depicted in Figure 2.10, $t_h = 0.142\lambda_0$ and $\epsilon_r = 3.25$ (i.e. $t_h = 0.2560\lambda_d$); whereas in Figure 2.11, $t_h = 0.06\lambda_0$ and $\epsilon_r = 17.5$ (i.e. $t_h = 0.2510\lambda_d$). Consequently, new approximations should be found for cylinders

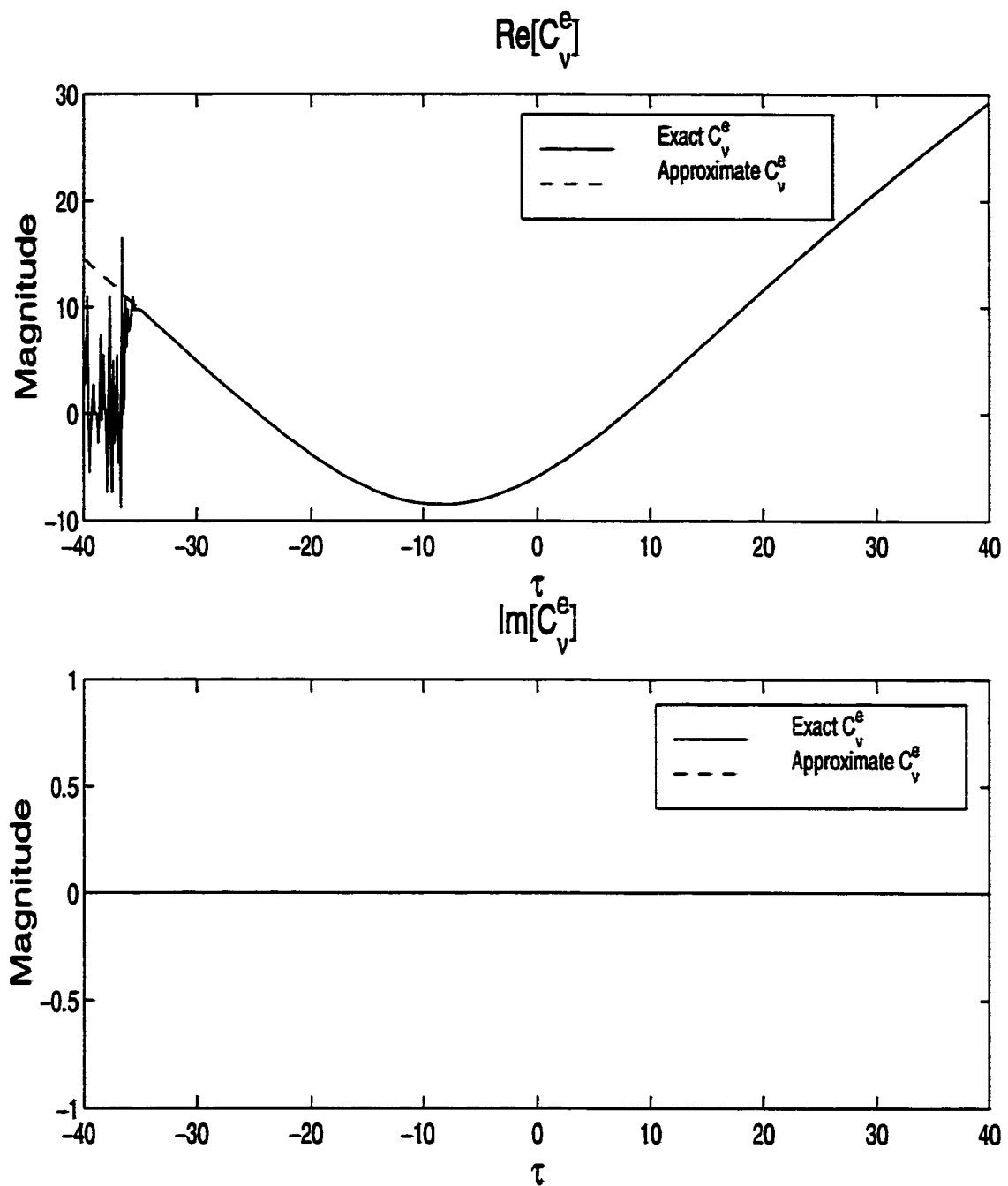


Figure 2.6: The real and imaginary parts of C_v^e for $a = 3\lambda_0$, $t_h = 0.06\lambda_0$, $\epsilon_r = 3.25$ (i.e. $t_h = 0.1082\lambda_d$) and $\alpha = \psi = 25^\circ$.

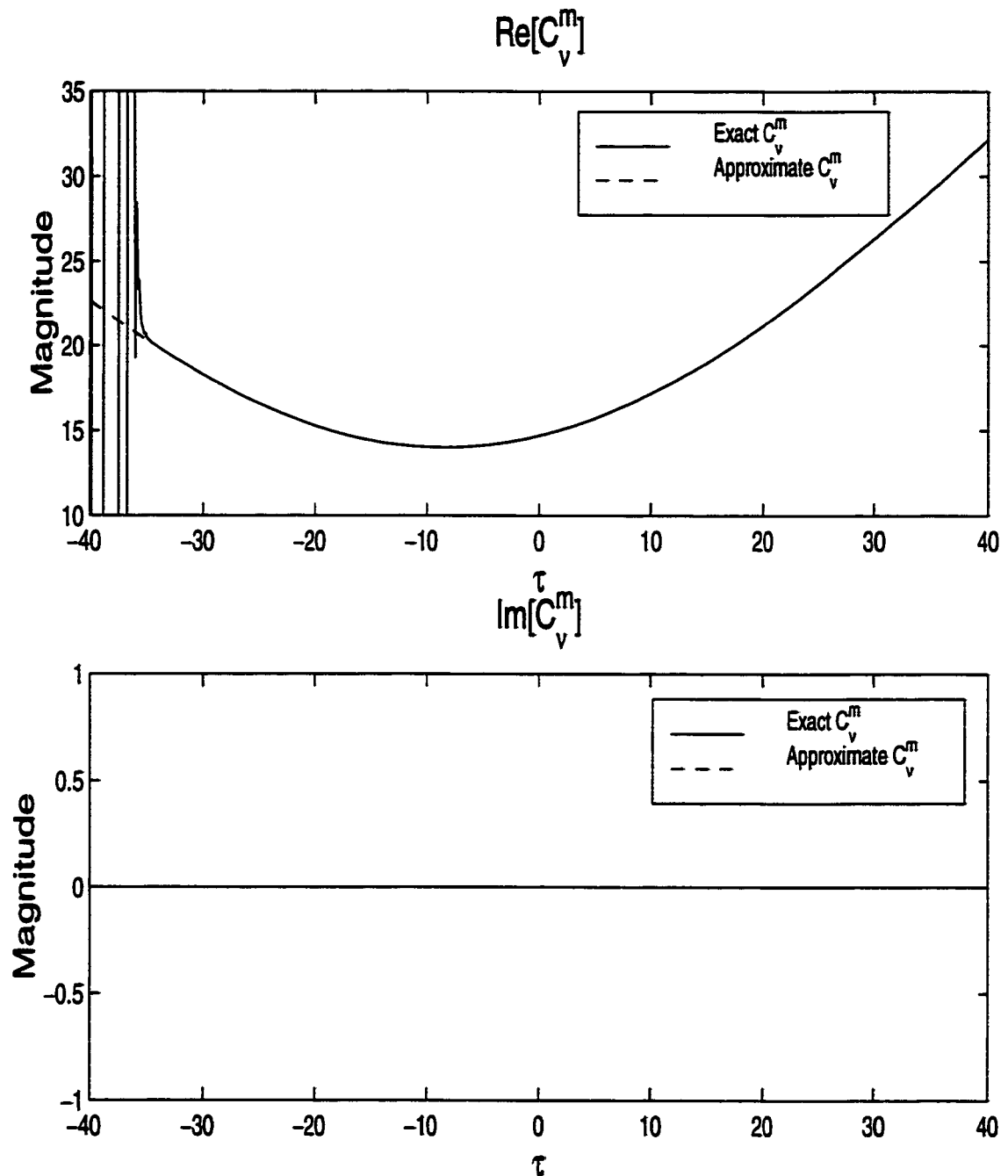


Figure 2.7: The real and imaginary parts of C_v^m for $a = 3\lambda_0$, $t_h = 0.06\lambda_0$, $\epsilon_r = 3.25$ (i.e. $t_h = 0.1082\lambda_d$) and $\alpha = \psi = 25^\circ$.

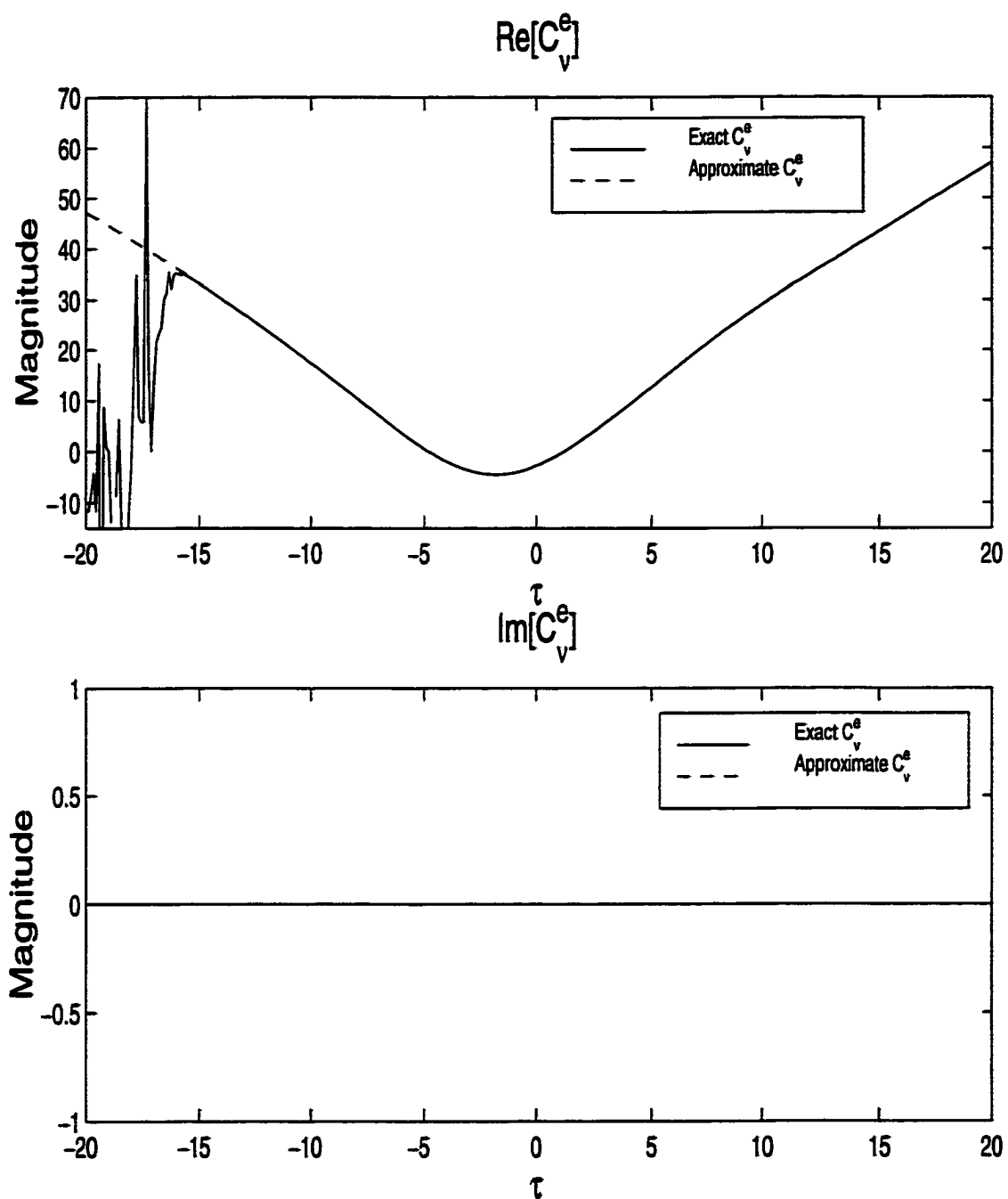


Figure 2.8: The real and imaginary parts of C_v^e for $a = 0.3\lambda_0$, $t_h = 0.06\lambda_0$, $\epsilon_r = 2.33$ (i.e. $t_h = 0.0916\lambda_d$) and $\alpha = \psi = 40^\circ$.

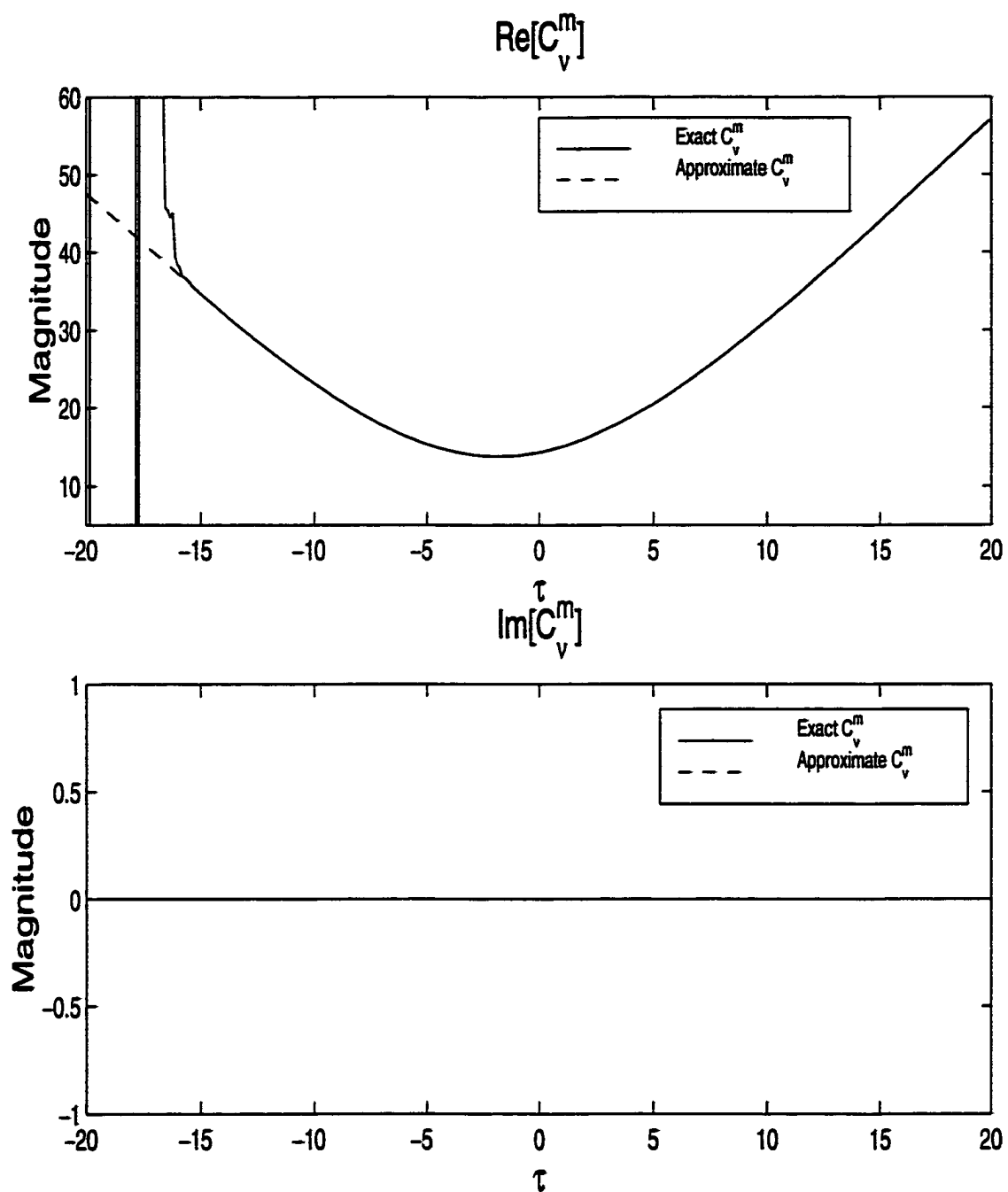


Figure 2.9: The real and imaginary parts of C_v^m for $\alpha = 0.3\lambda_0$, $t_h = 0.06\lambda_0$, $\epsilon_r = 2.33$ (i.e. $t_h = 0.0916\lambda_d$) and $\alpha = \psi = 40^\circ$.

having thicker coatings or higher ϵ_r . Nevertheless, the simplicity and accuracy of (2.62) and (2.63) is very encouraging.

2.5 Numerical Evaluation of Integrals

As given by (2.53)-(2.55) in Section 2.3, the final expressions for the surface fields contain two integrals, one in the t -domain which is obtained by mapping the SDP onto the real axis, and the other is in the τ -domain whose contour changes with respect to t as will be shown in this section. The integral along the t -axis can be easily performed in a very effective and accurate way using Gauss-Hermite quadrature [69] approach. This algorithm is best suited for integrals in the form

$$\int_{-\infty}^{\infty} e^{-x^2} f(x) dx = \sum_{j=1}^N w_j f(x_j) \quad (2.66)$$

where x_j are the roots of Hermite polynomials H_N and are given by

$$H_{j+1} = 2xH_j - 2jH_{j-1} \quad (2.67)$$

where $H_0(x) = 1$, $H_1(x) = 2x$ ($H_{-1}(x)$ is not necessary because the second term in the right hand side of (2.67) vanishes for $j = 0$). Note that w_j are the appropriate weights given by

$$w_j = \frac{2}{(\sqrt{2j}\tilde{H}_{j-1})^2} \quad (2.68)$$

where \tilde{H}_j is an orthonormal polynomial slightly different than H_j . To avoid possible numerical problems, they are generated by the following recurrence relation:

$$\tilde{H}_{j+1} = x\sqrt{\frac{2}{j+1}}\tilde{H}_j - \sqrt{\frac{j}{j+1}}\tilde{H}_{j-1} \quad (2.69)$$

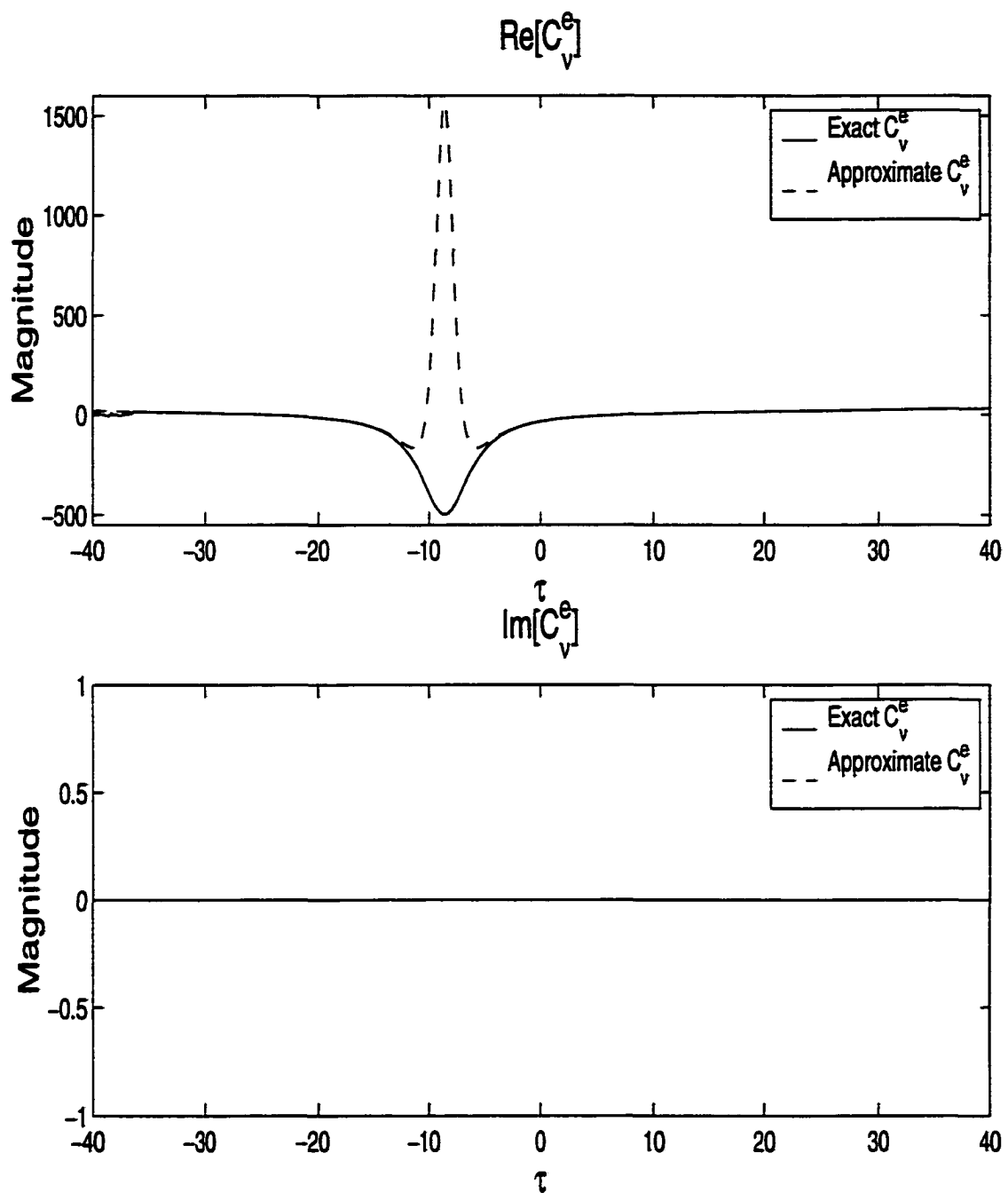


Figure 2.10: The real and imaginary parts of C_v^e for $a = 3\lambda_0$, $t_h = 0.142\lambda_0$, $\epsilon_r = 3.25$ (i.e. $t_h = 0.2560\lambda_d$) and $\alpha = \psi = 25^\circ$.

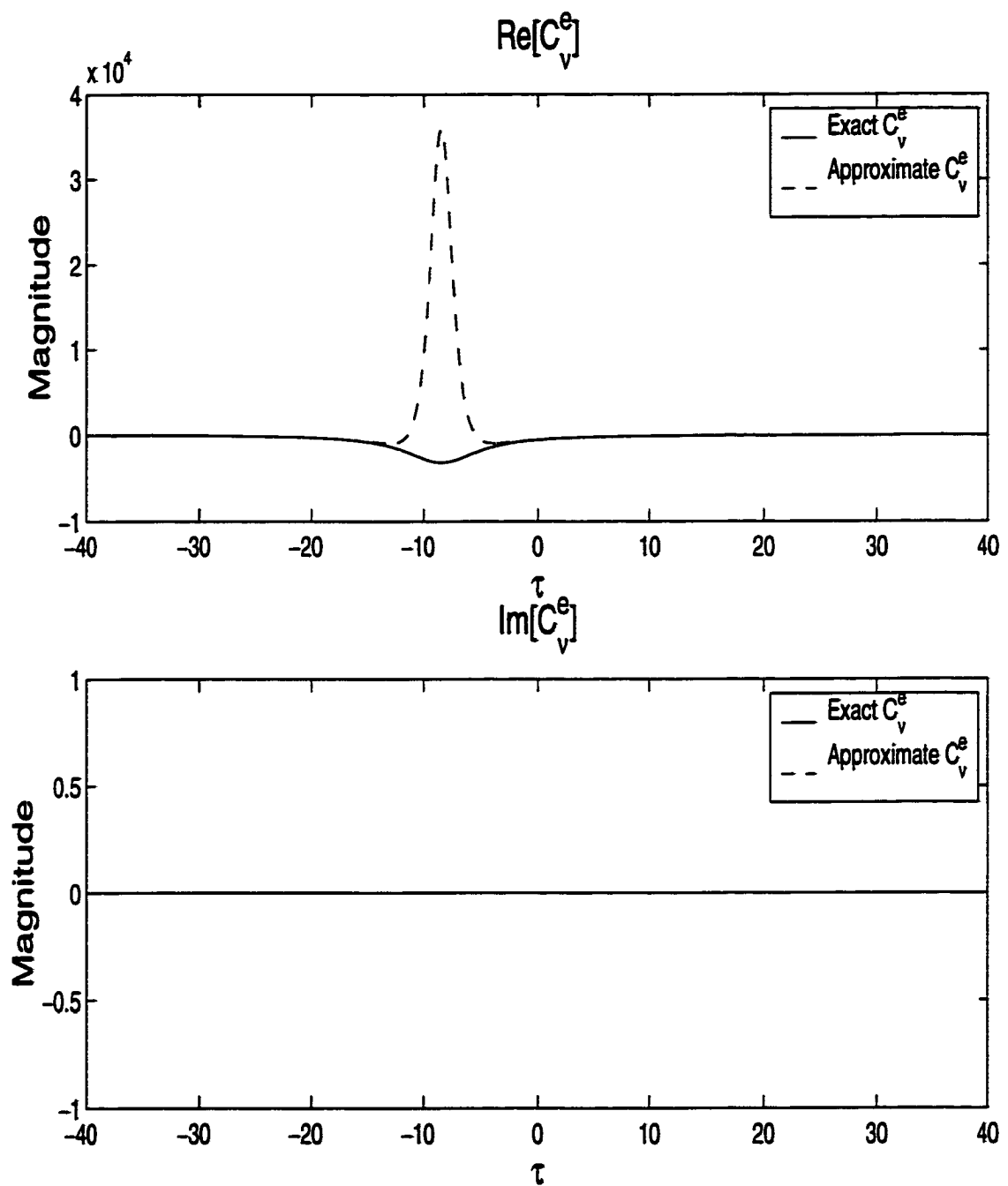


Figure 2.11: The real and imaginary parts of C_v^e for $\alpha = 3\lambda_0$, $t_h = 0.06\lambda_0$, $\epsilon_r = 17.5$ (i.e. $t_h = 0.2510\lambda_d$) and $\alpha = \psi = 25^\circ$.

with $\tilde{H}_{-1} = 0$ and $\tilde{H}_0 = \frac{1}{\pi^{1/4}}$ as given in [69]. The result of this procedure for (2.53)-(2.55) can be written as

$$E_\phi(\alpha, s) \approx \frac{\sqrt{2} e^{j3\pi/4}}{4\pi^2 d} \frac{e^{-jk_0 s}}{\sqrt{k_0 s}} \sum_{q=1}^Q w_q \frac{k_0 \cos \psi(t_q) m_t}{\cos(\frac{\alpha - \psi(t_q)}{2})} \left[\int_{C_\tau(t_q)} (G_{\phi\phi}(\tau, t_q) P_e^\phi + G_{\phi z}(\tau, t_q) P_e^z) e^{-j\xi\tau} d\tau \right] \quad (2.70)$$

$$E_z(\alpha, s) \approx \frac{\sqrt{2} e^{j3\pi/4}}{4\pi^2 d} \frac{e^{-jk_0 s}}{\sqrt{k_0 s}} \sum_{q=1}^Q w_q \frac{k_0 \cos \psi(t_q) m_t}{\cos(\frac{\alpha - \psi(t_q)}{2})} \left[\int_{C_\tau(t_q)} (G_{z\phi}(\tau, t_q) P_e^\phi + G_{zz}(\tau, t_q) P_e^z) e^{-j\xi\tau} d\tau \right] \quad (2.71)$$

and

$$E_\rho(\alpha, s) \approx \frac{\sqrt{2} e^{j3\pi/4}}{4\pi^2 d} \frac{e^{-jk_0 s}}{\sqrt{k_0 s}} \sum_{q=1}^Q w_q \frac{k_0 \cos \psi(t_q) m_t}{\cos(\frac{\alpha - \psi(t_q)}{2})} \left[\int_{C_\tau(t_q)} (G_{\rho\phi}(\tau, t_q) P_e^\phi + G_{\rho z}(\tau, t_q) P_e^z) e^{-j\xi\tau} d\tau \right] \quad (2.72)$$

where t_q are the roots of the Hermite polynomial $H_Q(t)$ and w_q are the appropriate weights. Values of t_q and w_q for some Q values are tabulated in Table 2.1. In the limiting case where $Q = 1$, $t_1 = 0$ and $w_1 = \sqrt{\pi}$, this algorithm will recover the saddle point integration used in [4], [5] and [6] (which is valid for large separations between source and observation points). This is shown in Appendix A. On the other hand, the integration along the τ -contour is not trivial because of the following reasons:

- a) The integration contour $C_\tau(t)$ has to be adjusted for each value of t_q . This contour mapping is essential because it avoids potential numerical problems due to the $e^{-j\xi\tau}$ term during the integration process (recall that $\xi = m_t(\phi - \phi')$ and $m_t = (\frac{k_{10}d}{2})^{1/3}$ with $k_{10} = k_0 \cos \psi(t_q)$) and guarantees that no pole crosses the integration contour $C_\tau(t_q)$.

Q	Abscissas $\pm x_q$	Weights w_q
1	0.000000	1.772454
2	0.707107	0.886227
3	0.000000 1.224745	1.181636 0.295409
4	0.524648 1.650680	0.804914 0.081313
5	0.000000 0.958572 2.020183	0.945309 0.393619 0.019953

Table 2.1: Abscissas and weights for Gauss-Hermite integration algorithm

b) The integrands in the τ -domain exhibit a highly oscillatory and slowly decaying nature. Therefore, one must be careful in the choice of an integration routine to handle the oscillatory behavior of the integrands as well as a proper tail should be added to the solution to take care of the slowly decaying nature of the integrands.

2.5.1 The Choice of Integration Contour

The original contour of integration C in the ν -plane is depicted in Figure 2.12 (also in Figure 2.2). A careful study in [52], [4] and others show that the poles and branch cuts of the Green's function components remain in the second and fourth quadrants of the complex ν -plane. Since there is no branch cut or poles in the third quadrant where $Re(\nu) < 0$ and $Im(\nu) < 0$, the contour C can be freely deformed to a complex \tilde{C} contour as shown in Figure 2.12. The reason for such a deformation is that the integrands converge much faster on the complex \tilde{C} contour due to the $e^{-j\nu(\phi-\phi')}$ term (an exponential decay is achieved). However, the integration variable

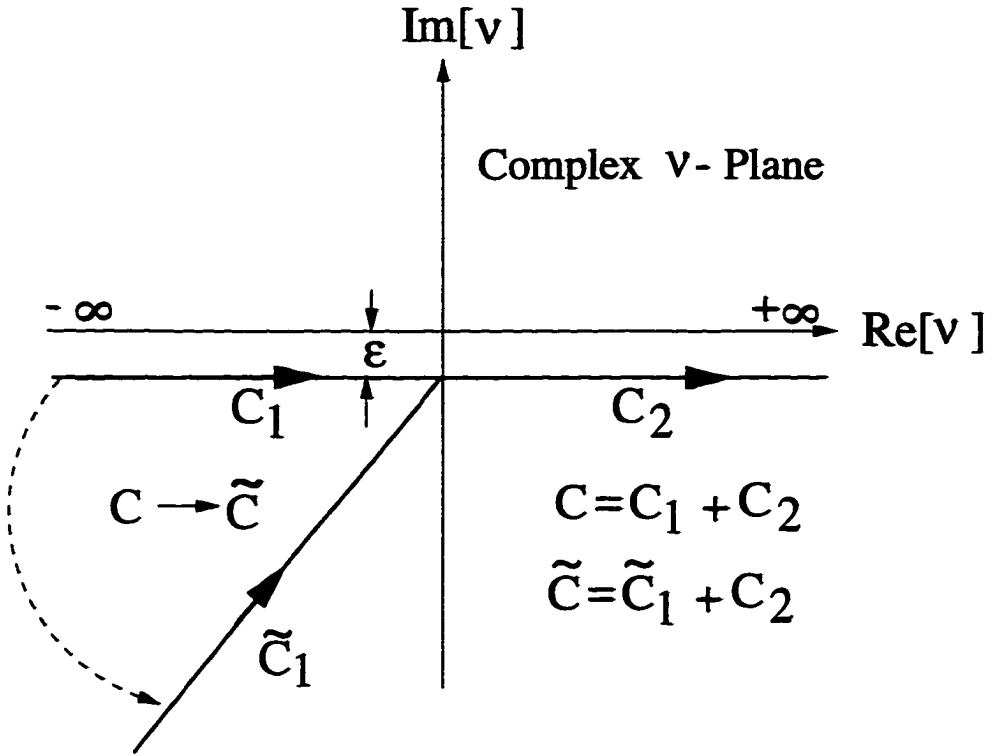


Figure 2.12: Integration paths C and \tilde{C} in the complex $\nu-$ plane

in (2.70)-(2.72) is τ where $\tau = \frac{\nu - k_{t0}d}{m_t}$, $m_t = (\frac{k_{t0}d}{2})^{1/3}$ with $k_{t0} = k_0 \cos \psi(t_q)$, so the integration contour in the τ -plane depends on the values of t_q because k_{t0} is a function of t_q . Figure 2.13 depicts a typical SDP contour on which three $\psi(t_q)$ values are marked. The corresponding τ -contours ($C_\tau(t_q)$) are illustrated in Figure 2.14 where they all map to \tilde{C} depicted in Figure 2.12, in the ν -plane. In Figure 2.14, the contour $C_\tau(t_q)$ is divided into two regions $C_\tau^\pm(t_q)$ where $C_\tau^-(t_q)$ is the part of the integration contour on which $Re(\tau) < Re(\bar{\tau})$ whereas, $C_\tau^+(t_q)$ is the part on which $Re(\bar{\tau}) < Re(\tau)$. Furthermore, $C_\tau^+(t_q)$ has a segment defined as $Re(\tau') < Re(\tau) < \infty$ where a tail is applied as will be mentioned in the following subsection. Note that, the $C_\tau^+(t_q)$ contour goes to infinity following the direction of \hat{p}_i vectors.

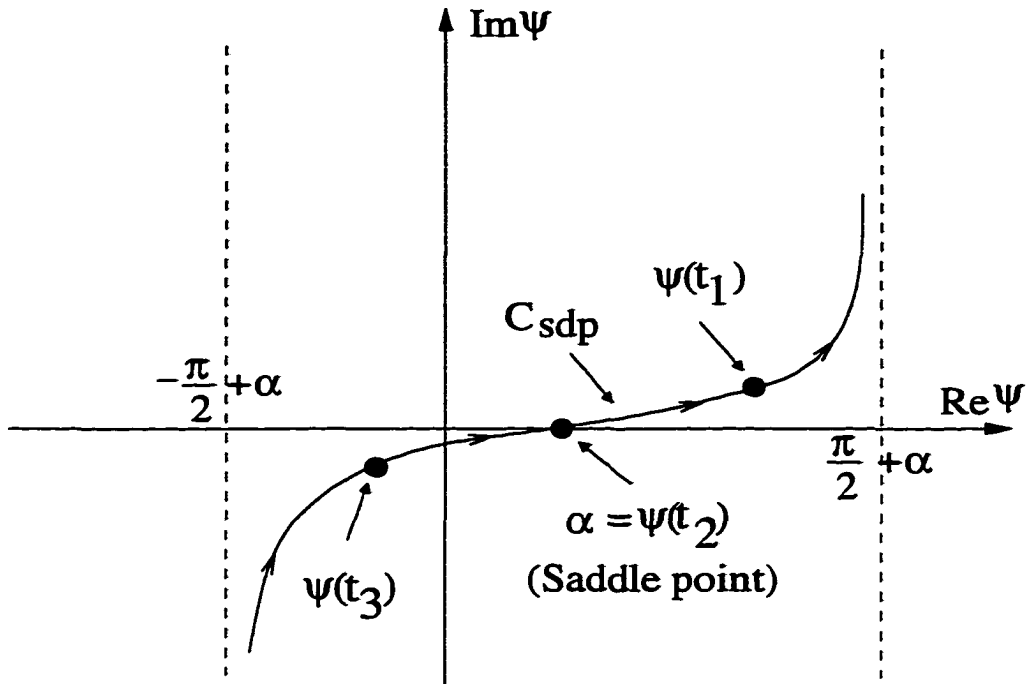


Figure 2.13: Integration points on the SDP contour

2.5.2 Integration Routine and Tail Contributions

The integration in the τ -plane is performed using Filon's algorithm combined with a Gaussian quadrature approach, where a tail is added for large τ values ($\tau \geq \tau'$) so that integration from τ' to ∞ can be performed analytically. Along the contour $C_\tau^-(t_q)$ the integrand decays quickly (exponential decay is achieved) and the numerical integration can be performed easily. The integration along $C_\tau^+(t_q)$ is more difficult because the integrand does not decay fast and it is oscillatory. To handle the oscillatory nature of the integrand Filon's algorithm [70]-[71] is used. In this algorithm, a portion of the integration contour ($Re(\bar{\tau}) < Re(\tau) < Re(\tau')$) is subdivided into half periods determined by $\pi/|\xi|$ to avoid numerical problems that might be encountered

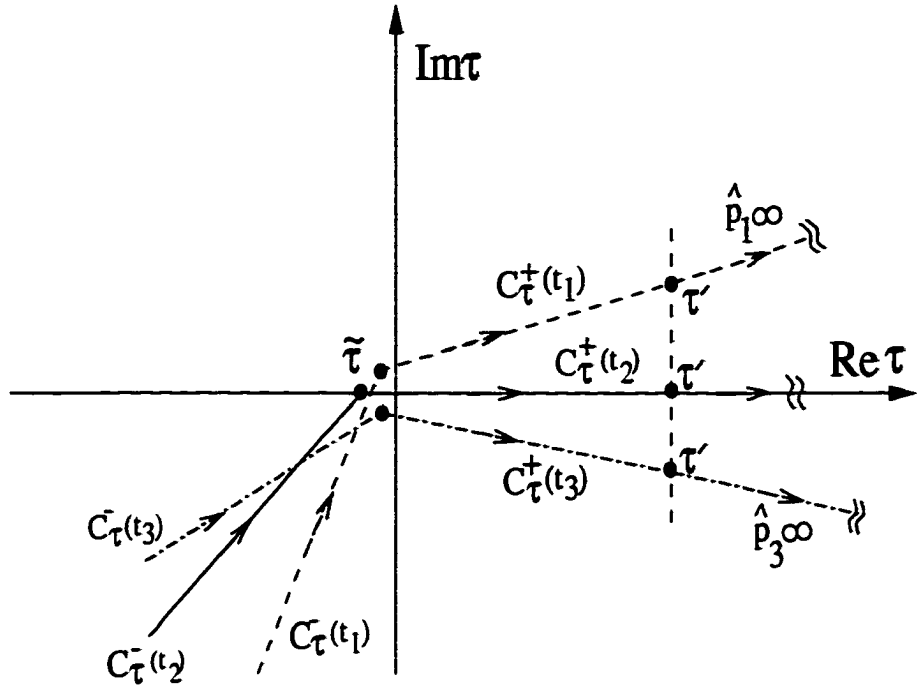


Figure 2.14: Typical integration contours in the τ -plane

if arbitrary intervals are chosen ([72]). Then a Gaussian quadrature algorithm is used to perform the integration within each half period.

On the other hand, the limiting values of the Green's function components for large τ values are given by

$$\lim_{\tau \rightarrow \infty} G_{zz}(t_q, \tau) = \frac{B_1}{\tau} \quad (2.73)$$

$$\lim_{\tau \rightarrow \infty} G_{\phi z}(t_q, \tau) = B_2 \quad (2.74)$$

$$\lim_{\tau \rightarrow \infty} G_{\phi \phi}(t_q, \tau) = B_3 \tau + B_4 \quad (2.75)$$

$$\lim_{\tau \rightarrow \infty} G_{\rho z}(t_q, \tau) = B_5 \quad (2.76)$$

and

$$\lim_{\tau \rightarrow \infty} G_{\rho \phi}(t_q, \tau) = B_6 \tau + B_7 \quad (2.77)$$

where B_i are some constants whose values are given in Appendix B. As it can be seen in (2.73)-(2.77), the Green's function components are not absolutely convergent for large τ values ($G_{\phi\phi}(t_q, \tau)$ and $G_{\rho\phi}(t_q, \tau)$ are even increasing functions with respect to τ). Therefore, in the calculation of integrals which contain $G_{zz}(t_q, \tau)$, $G_{\phi z}(t_q, \tau) = G_{z\phi}(t_q, \tau)$ and $G_{\rho z}(t_q, \tau)$, the contour $C_\tau^+(t_q)$ is further divided into two regions where the numerical integration is performed in one region and the integration is evaluated analytically in the second region using a proper tail. Namely, an integral related with the $G_{zz}(t_q, \tau)$ component of the dyadic Green's function which is in the form of

$$I_1 = C_1 \int_{C_\tau^-(t_q)} G_{zz}(t_q, \tau) P_e^z e^{-j\xi\tau} d\tau \quad (2.78)$$

is written as

$$\begin{aligned} I_1 = & C_1 \left[\int_{C_\tau^-(t_q)} G_{zz}(t_q, \tau) P_e^z e^{-j\xi\tau} d\tau + \int_{\bar{\tau}}^{\tau'} G_{zz}(t_q, \tau) P_e^z e^{-j\xi\tau} d\tau \right. \\ & \left. + \int_{\tau'}^{j\infty} \frac{B_1}{\tau} P_e^z e^{-j\xi\tau} d\tau \right]. \end{aligned} \quad (2.79)$$

The following complex exponential integral:

$$F_1(\tau') = \int_{\tau'}^{j\infty} \frac{B_1}{\tau} e^{-j\xi\tau} d\tau \quad (2.80)$$

is evaluated using a first order stationary-phase method in which only the end-point contributions are considered since the interval $\tau' < \tau < \infty$ does not contain a stationary point. Furthermore, the contribution from ∞ is omitted as mentioned in [65] and consequently, $F_1(\tau')$ is given by

$$F_1(\tau') \approx B_1 \frac{e^{-j\xi\tau'}}{j\xi\tau'} . \quad (2.81)$$

In Figure 2.15, the magnitude and phase of an integral in the form of (2.78) is plotted versus N (where $N = \tau'/(\frac{m_t}{2k_{totd}})$) with and without tail contribution for a cylinder

whose parameters are given as $a = 3\lambda_0$, $t_h = 0.06\lambda_0$, $\epsilon_r = 3.25$ and $\alpha = 40^\circ$. As illustrated in the figure with the tail contribution, good accuracy can be obtained with $N = 100$. Although this N value can be slightly adjusted for some other cases, no radical change should be expected.

Similarly, an integral related with the $G_{\phi z}(t_q, \tau)$ (or $G_{z\phi}(t_q, \tau)$) component of the dyadic Green's function which is in the form of

$$I_2 = C_1 \int_{C_\tau(t_q)} G_{\phi z}(t_q, \tau) P_e^z e^{-j\xi\tau} d\tau \quad (2.82)$$

is written as

$$\begin{aligned} I_2 = C_1 & \left[\int_{C_\tau^-(t_q)} G_{\phi z}(t_q, \tau) P_e^z e^{-j\xi\tau} d\tau + \int_{\bar{\tau}}^{\tau'} G_{\phi z}(t_q, \tau) P_e^z e^{-j\xi\tau} d\tau \right. \\ & \left. + \int_{\tau'}^{\hat{\rho}_i \infty} B_2 P_e^z e^{-j\xi\tau} d\tau \right] \end{aligned} \quad (2.83)$$

and the following integral:

$$F_2(\tau') = \int_{\tau'}^{\infty} B_2 e^{-j\xi\tau} d\tau \quad (2.84)$$

is evaluated using the first order stationary-phase method, and is given by

$$F_2(\tau') \approx B_2 \frac{e^{-j\xi\tau'}}{j\xi} . \quad (2.85)$$

However, due to the analytical properties of $G_{\phi\phi}(t_q, \tau)$ and $G_{\rho\phi}(t_q, \tau)$, the integrals that contain these components are performed via an envelope extraction technique in the $C_\tau^+(t_q)$ part of the integration contour in the τ -domain. In this technique, the asymptotic value of the integrand can be integrated in closed form; therefore, if one subtracts the asymptotic value from the integrand, the resulting integrand is

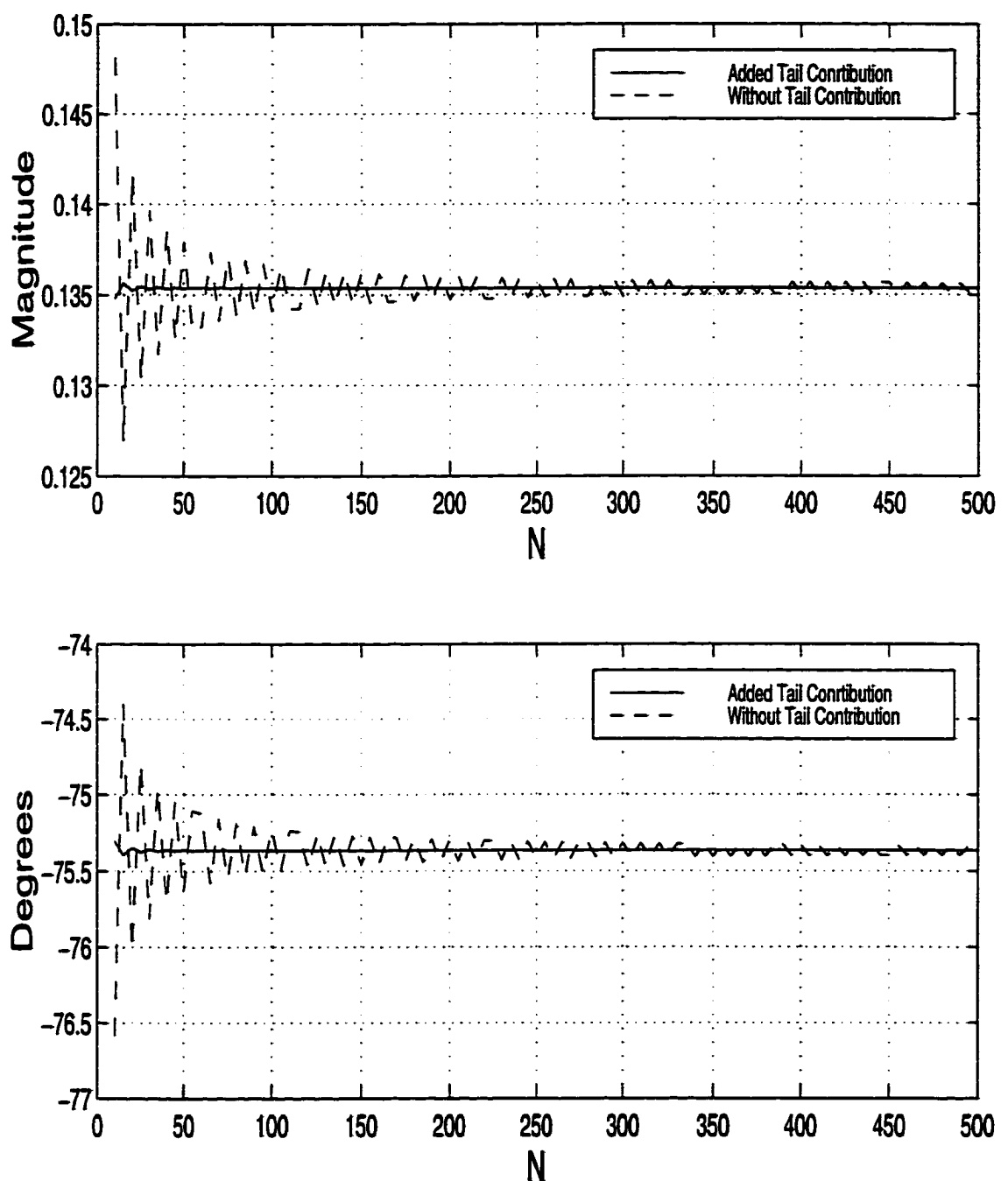


Figure 2.15: Effect of tail contribution on an integral in the form of (2.78) for a coated cylinder with $a = 3\lambda_0$, $t_h = 0.06\lambda_0$, $\epsilon_r = 3.25$ and $\alpha = 40^\circ$.

relatively smooth and fast decaying so that it can be integrated efficiently. Namely, an integral with the $G_{\phi\phi}(t_q, \tau)$ component is written as

$$I_3 = C_1 \left[\int_{C_\tau^-(t_q)} G_{\phi\phi}(t_q, \tau) P_e^\phi e^{-j\xi\tau} d\tau + \int_{C_\tau^+(t_q)} (G_{\phi\phi}(t_q, \tau) - B_3\tau - B_4) P_e^\phi e^{-j\xi\tau} d\tau \right. \\ \left. + \int_{C_\tau^+(t_q)} B_3\tau P_e^\phi e^{-j\xi\tau} d\tau + \int_{C_\tau^+(t_q)} B_4 P_e^\phi e^{-j\xi\tau} d\tau \right] . \quad (2.86)$$

As a result of this process, the integrand of the second integral becomes rapidly convergent and can be performed easily using a numerical integration technique. In Figure 2.16, the first plot compares the integrand of (2.86) with the limiting value of $G_{\phi\phi}(t_q, \tau)$ and the second plot illustrates the decaying behavior of the integrand for the second integral in (2.86) for a cylinder with $a = 2.5\lambda_0$, $t_h = 0.06\lambda_0$, $\epsilon_r = 2.33$ and $\alpha = 50^\circ$. The fourth integral has the same form as that of (2.84) and hence is given by (2.85), except B_2 is replaced by B_4 . The only remaining part is the evaluation of the third integral which can be recognized as the Fourier transform of a ramp function and is given by

$$\int_{C_\tau^+(t_q)} B_3\tau e^{-j\xi\tau} d\tau = -B_3 \frac{1}{\xi^2} . \quad (2.87)$$

The Green's function components $G_{\rho z}(t_q, \tau)$ and $G_{\rho\phi}(t_q, \tau)$ are treated in the same fashion as (2.82)-(2.87) since $G_{\rho z}(t_q, \tau)$ exhibits a behavior similar to (2.74) whereas $G_{\rho\phi}(t_q, \tau)$ exhibits a behavior like (2.75).

2.6 Numerical Results

To access the accuracy of this method, numerical results are obtained for the mutual coupling between two tangential (to the surface of the cylinder), and between tangential and normal (ρ -directed) current modes. These results are obtained using

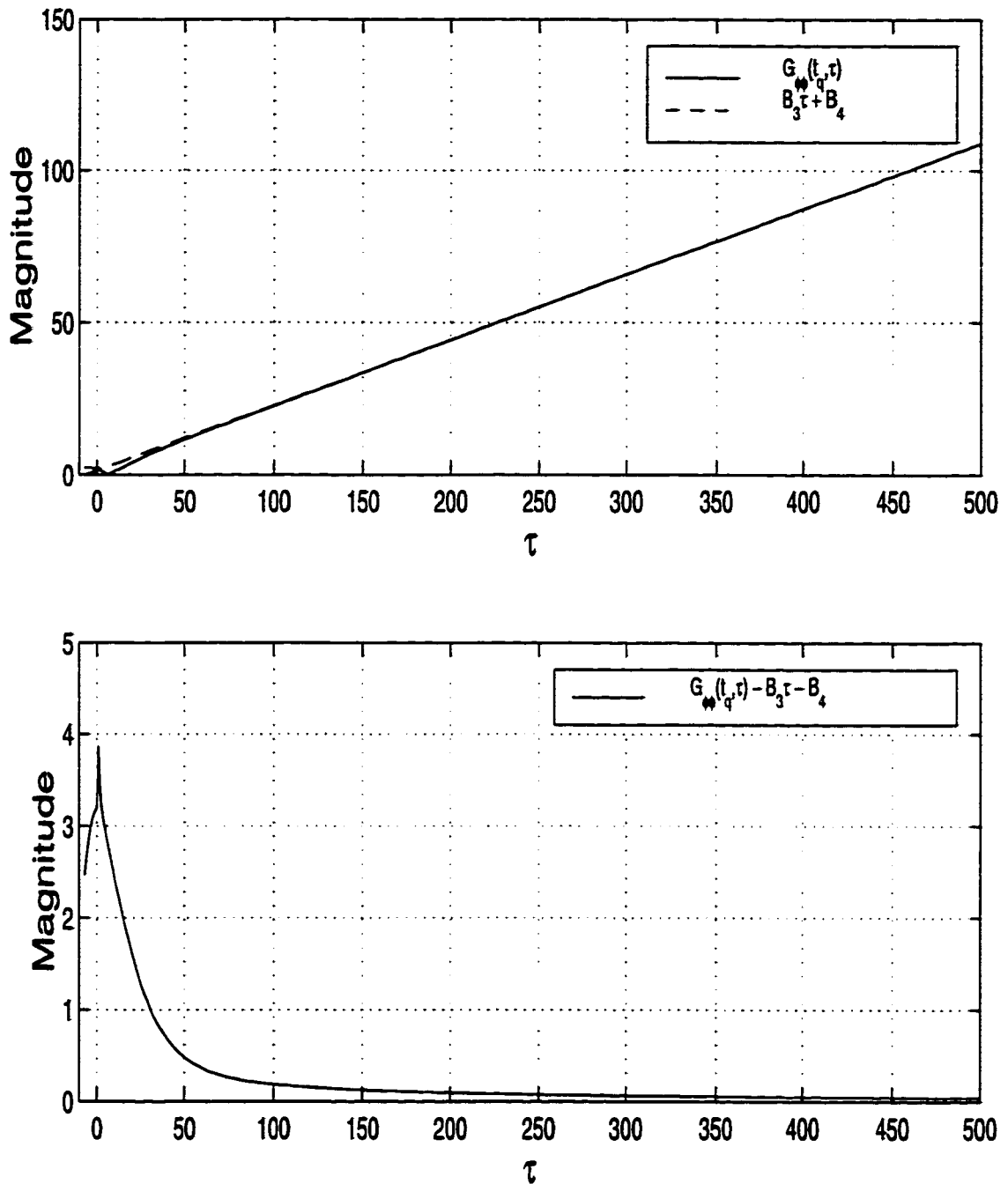


Figure 2.16: Effect of the envelope extraction technique on an integral written in the form of (2.86) for a coated cylinder with $a = 2.5\lambda_0$, $t_h = 0.06\lambda_0$, $\epsilon_r = 2.33$ and $\alpha = 50^\circ$.

(2.51) and compared with the traditional eigenfunction solution given by (2.15) for several cylinders with different coating properties. For the tangential elements, each current mode is defined by a piecewise sinusoid along the direction of the current and by constant along the direction perpendicular to the current. As an example, for a current in the z -direction, the well-known piecewise sinusoid current distribution (except the parameter k_a) is given by [59]

$$PWS(k_a, z_a, z) = \begin{cases} \frac{\sin[k_a(z_a - |z|)]}{2l_a \sin(k_a z_a)} & |z| < z_a \\ 0 & elsewhere \end{cases} \quad (2.88)$$

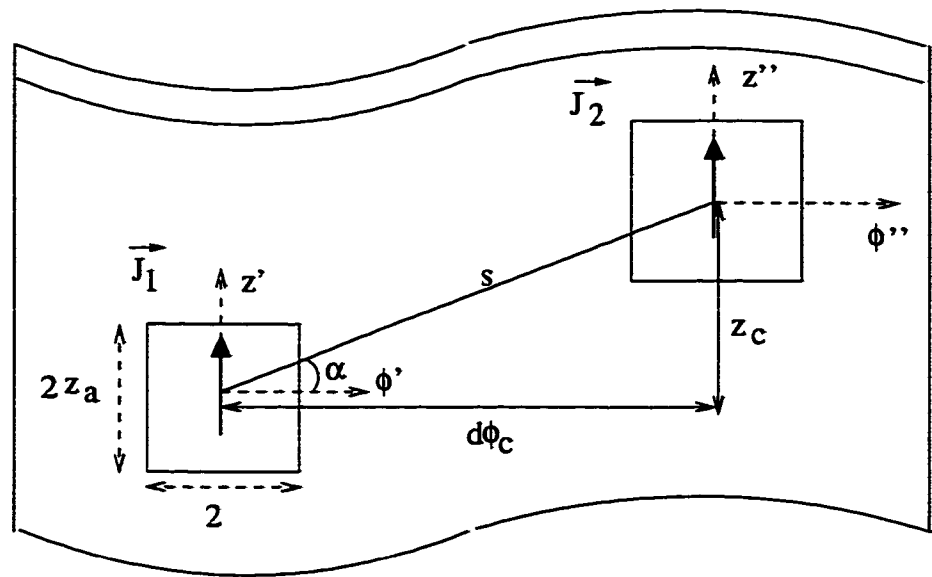
where $k_a = k_0 \sqrt{(\epsilon_r + 1)/2}$, and z_a and l_a are both depicted in Figure 2.17 along with the mutual coupling geometry. Each element has dimensions of $0.05\lambda_0$ (along the direction of current) by $0.02\lambda_0$. This particular choice of current modes guarantees the convergence of the reference (spectral domain) solution for large cylinders, even though the rate of convergence is very slow.

Figure 2.18 shows the real and imaginary parts of the mutual coupling between two identical z -directed current sources for two cylinders whose material parameters are the same. The first cylinder has an inner radius $a = 3\lambda_0$, whereas for the second one, $a = 1.5\lambda_0$. The angle α for these cylinders is chosen to be 55° and 40° , respectively. The real and imaginary parts of the mutual coupling between and a ϕ - and a z -directed current sources for the same cylinders are depicted in Figure 2.19 where the α values are 45° and 25° , respectively. Figure 2.20 show similar results for the coupling between two ϕ -directed current sources on the same cylinders with the α values 40° and 30° , respectively. For the smaller cylinder, for separations larger than $3.5\lambda_0$ (or $3\lambda_0$ depending upon the polarization), the effects of multiple wave encirclements around the coated cylinder may become visible and hence, addition of the $p = |1|$ given

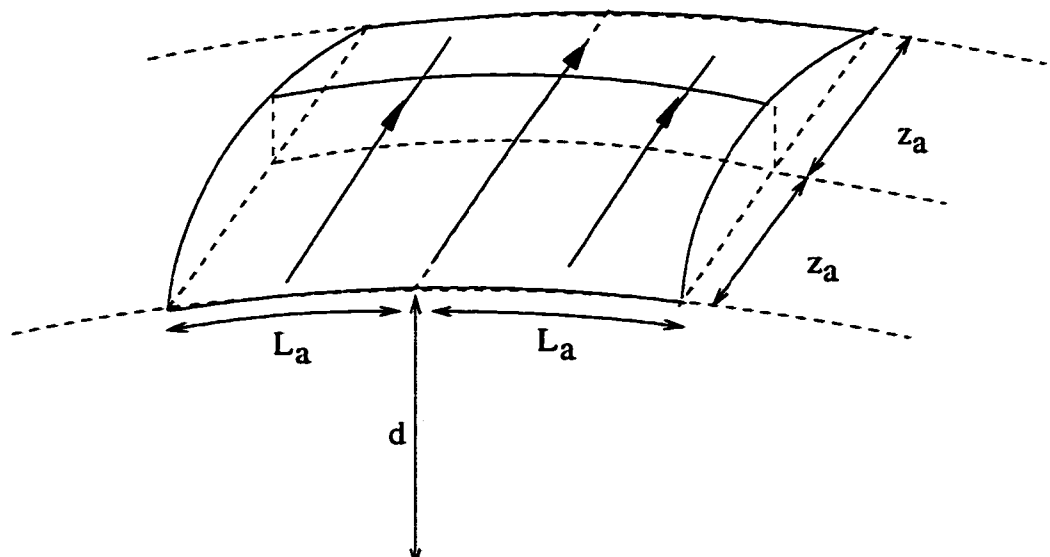
by (2.36) may be necessary. However, multiple wave encirclements are not included in the numerical results, the separation s is stopped either at $3.5\lambda_0$ or $3\lambda_0$ depending upon the polarization. As seen from these figures, excellent agreement is achieved even for separations as small as $0.2\lambda_0$ (even $0.1\lambda_0$ for some cases). Furthermore, the SDP representation is more efficient than the traditional eigenfunction solution. In Figure 2.18(a), the elapsed time for the calculation of the eigenfunction solution is approximately 5 minutes for 50 data points. However, the evaluation of the SDP representation requires approximately 20 to 30 seconds for the same number of data points. Similarly, 5 to 6 minutes are required for the evaluation of the eigenfunction solution in Figures 2.19(a) and 2.20(a) for 50 data points; whereas the elapsed time for the evaluation of the SDP representation is approximately 15 seconds for Figure 2.19(a) and 24 seconds for Figure 2.20(a) for the same number of data points. Note that 1500 terms are included in the summation on the n variable ($500 \times$ radius of the cylinder in wavelengths) for the eigenfunction solution. Therefore, as the electrical size (radius) of the cylinder gets large, the number of terms to be summed in the eigenfunction solution also increases and calculation of mutual coupling for electrically large cylinders using an eigenfunction solution becomes extremely inefficient.

On the other hand, the coupling between a normal and a tangential electric current source are given in Figure 2.21. For a cylinder with $a = 2.0184\lambda_0$, $t_h = 0.0214\lambda_0$, $\epsilon_r = 2.94$, the real and imaginary parts of the mutual coupling between a ϕ - and a ρ -directed sources are depicted in Figure 2.21(a) where $\alpha = 25^\circ$, and the same results are depicted in Figure 2.21(b) for the coupling between a z - and a ρ -directed sources when $\alpha = 40^\circ$.

It should be mentioned at this point that this method has some accuracy problems near the paraxial region, $\alpha \rightarrow 90^\circ$, of the cylinder due to the mapping given by (2.38). This is well-known problem that has been observed for PEC and impedance cylinders in the past where the mapping in (2.38) was used. In Figure 2.22, the real and imaginary parts of the mutual coupling between two tangential current modes (two ϕ -directed current modes in Figure 2.22(a) and two z -directed current modes in Figure 2.22(b)) are depicted for a cylinder with $a = 3\lambda_0$, $t_h = 0.06\lambda_0$ and $\epsilon_r = 3.25$. The angle α is selected as 70° for both cases which is close to the paraxial region and some disagreement between the SDP representation and the eigenfunction solution starts to appear. Valid solutions in the paraxial region will be presented in the following chapter. Note that there is a region where both solutions (i.e. SDP representation and paraxial region solutions) yield almost the same accuracy. This is a desired feature because one can safely switch from one representation to the other in a MoM-based solution where mutual coupling calculations are needed for arbitrary locations of the source and observation points.

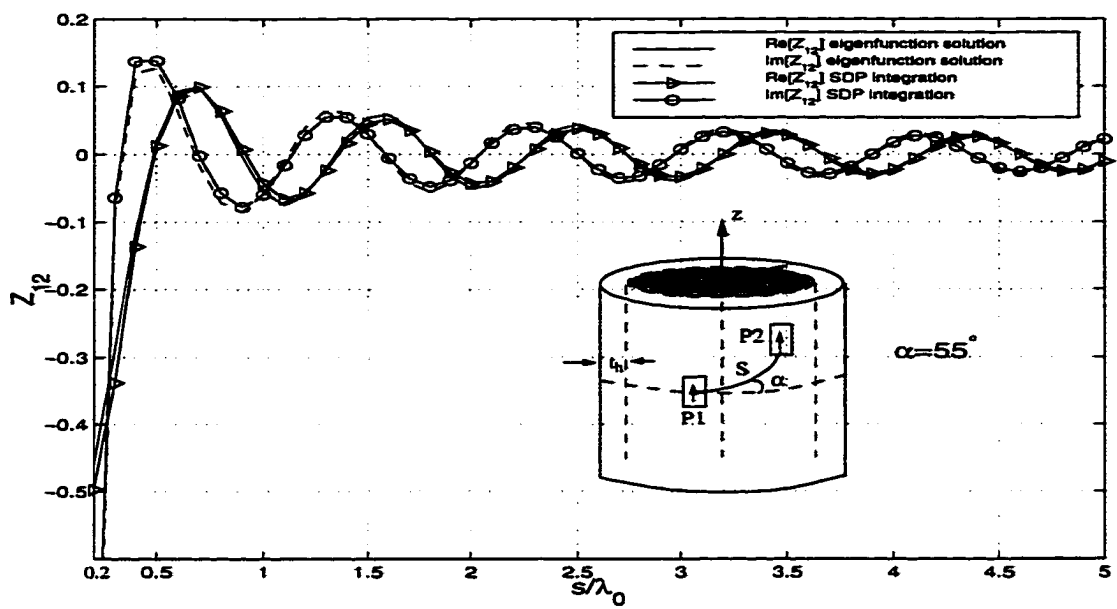


(a)

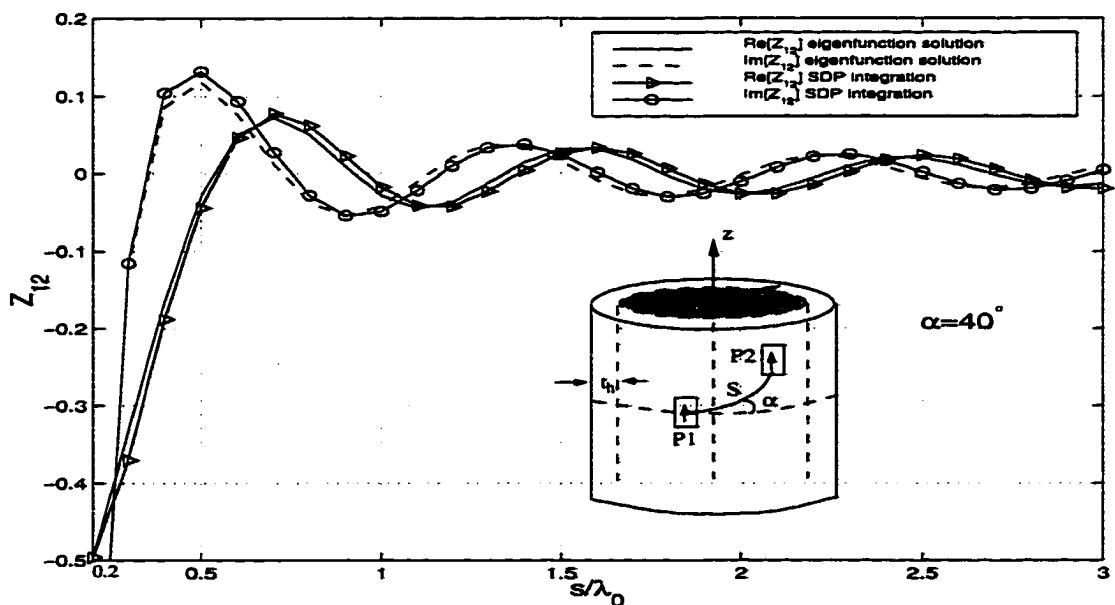


(b)

Figure 2.17: (a) Geometry used for mutual coupling problem (b) Piecewise sinusoidal current distribution on each tangential element.



(a) $a = 3\lambda_0, t_h = 0.06\lambda_0, \epsilon_r = 3.25$



(b) $a = 1.5\lambda_0, t_h = 0.06\lambda_0, \epsilon_r = 3.25$

Figure 2.18: Real and imaginary parts of the mutual coupling between two identical z-directed current sources for two coated cylinders of different radii.

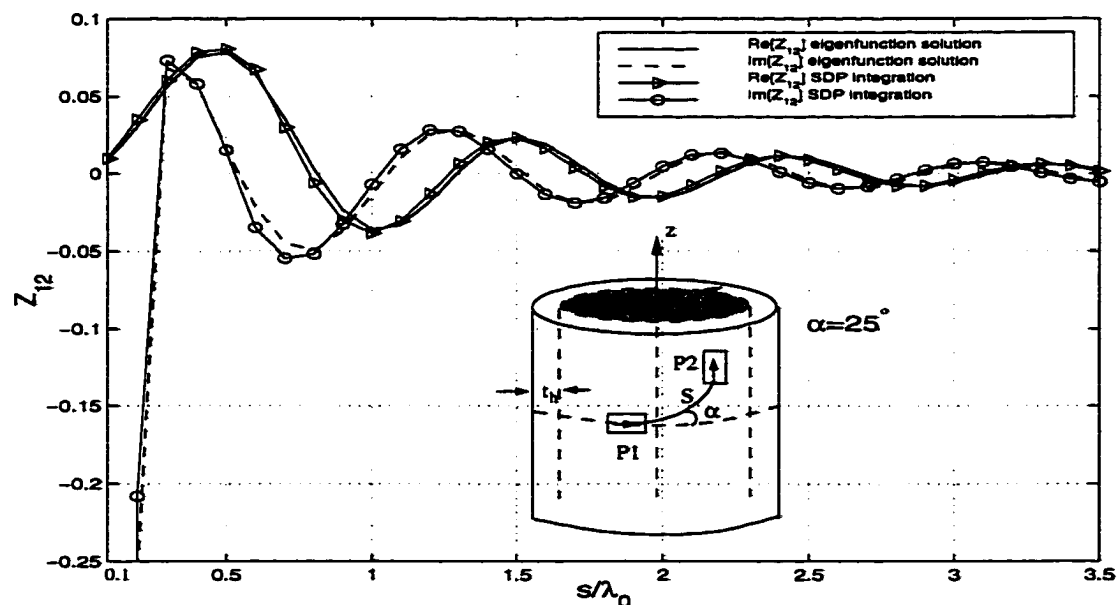
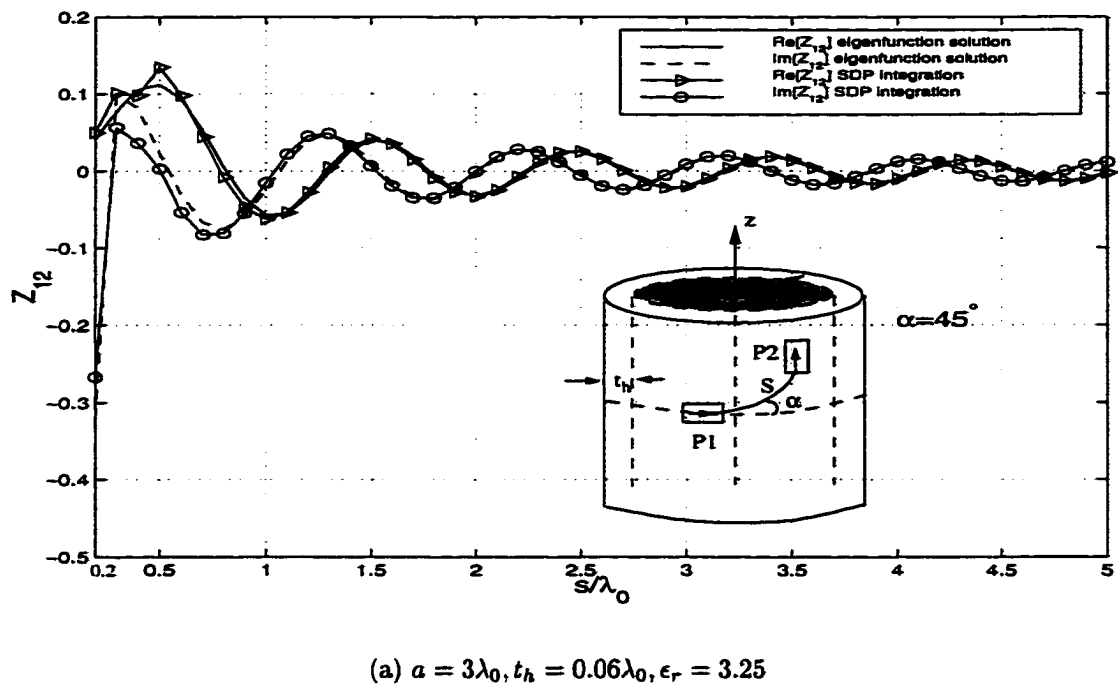
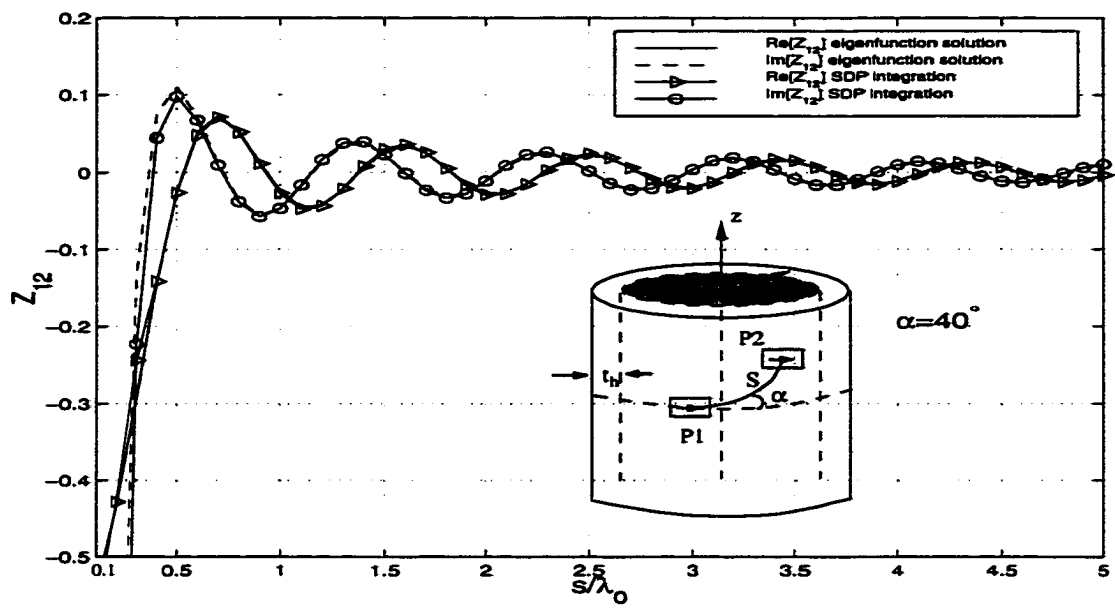
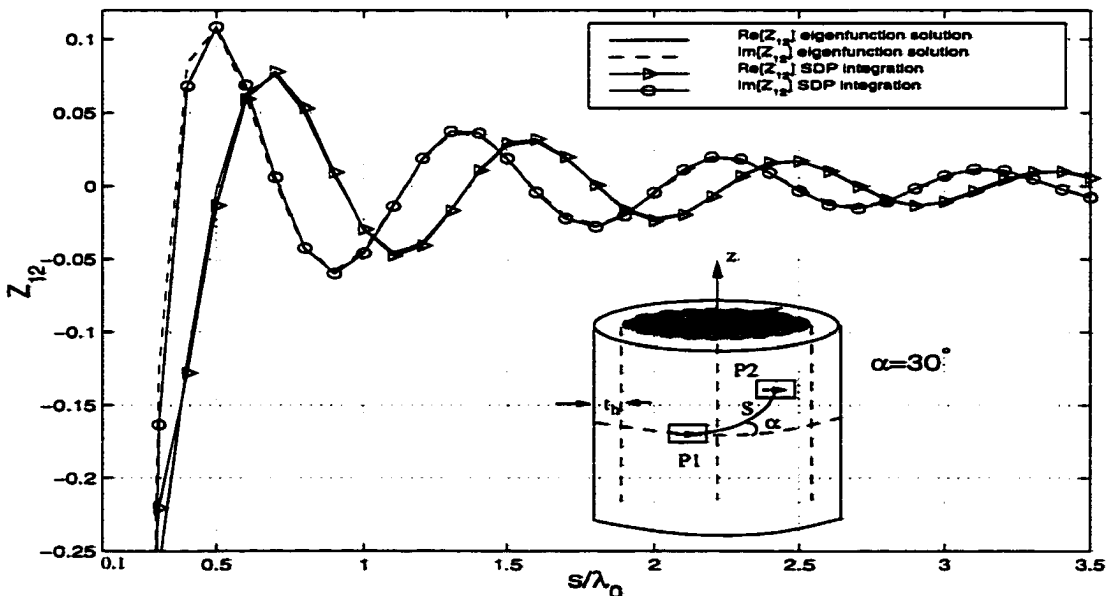


Figure 2.19: Real and imaginary parts of the mutual coupling between ϕ - and z -directed current sources for two coated cylinders of different radii.

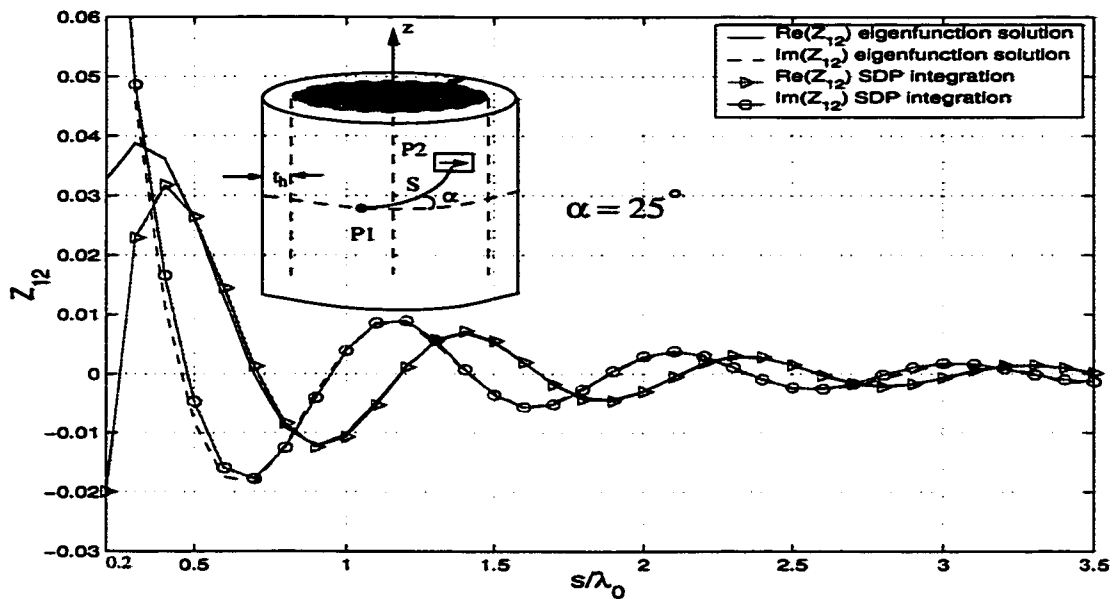


(a) $a = 3\lambda_0, t_h = 0.06\lambda_0, \epsilon_r = 3.25$

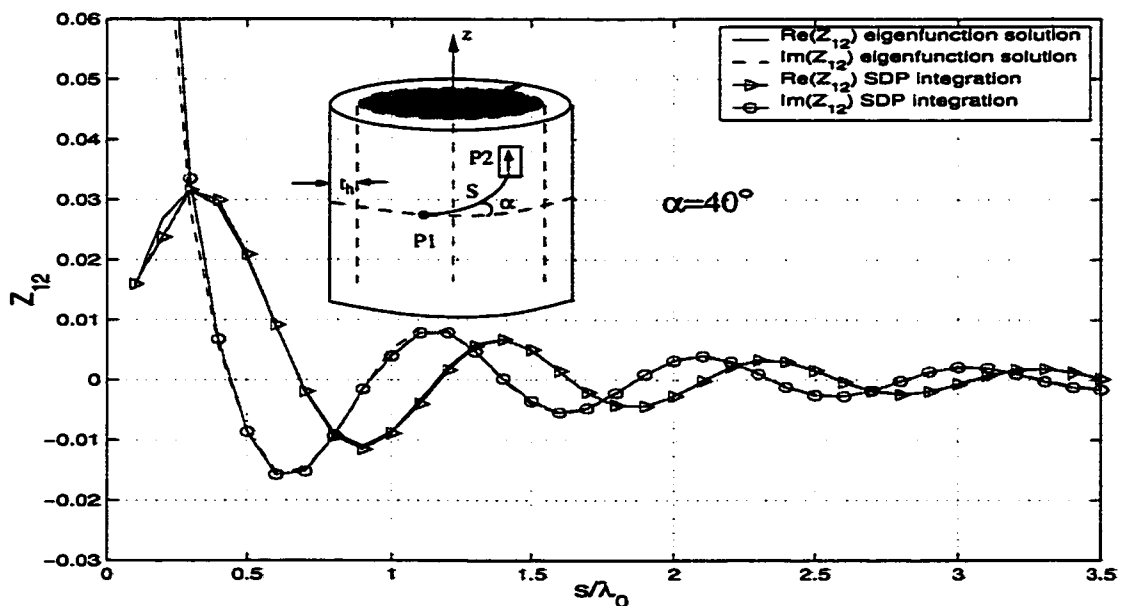


(b) $a = 1.5\lambda_0, t_h = 0.06\lambda_0, \epsilon_r = 3.25$

Figure 2.20: Real and imaginary parts of the mutual coupling between two ϕ -directed current sources for two coated cylinders of different radii.

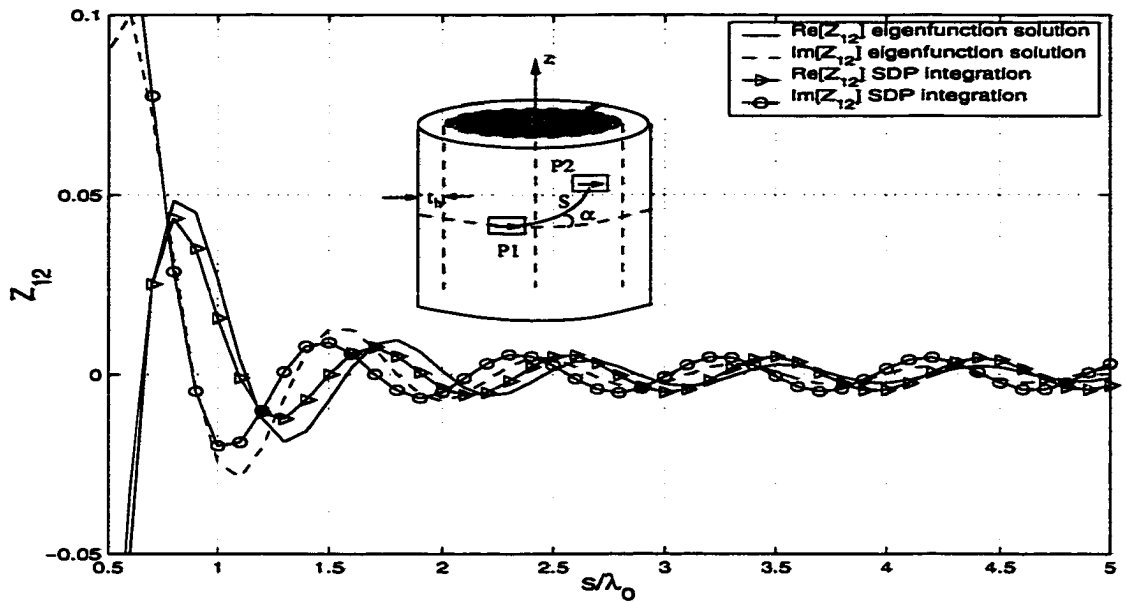


(a) coupling between a ϕ - and a ρ -directed sources

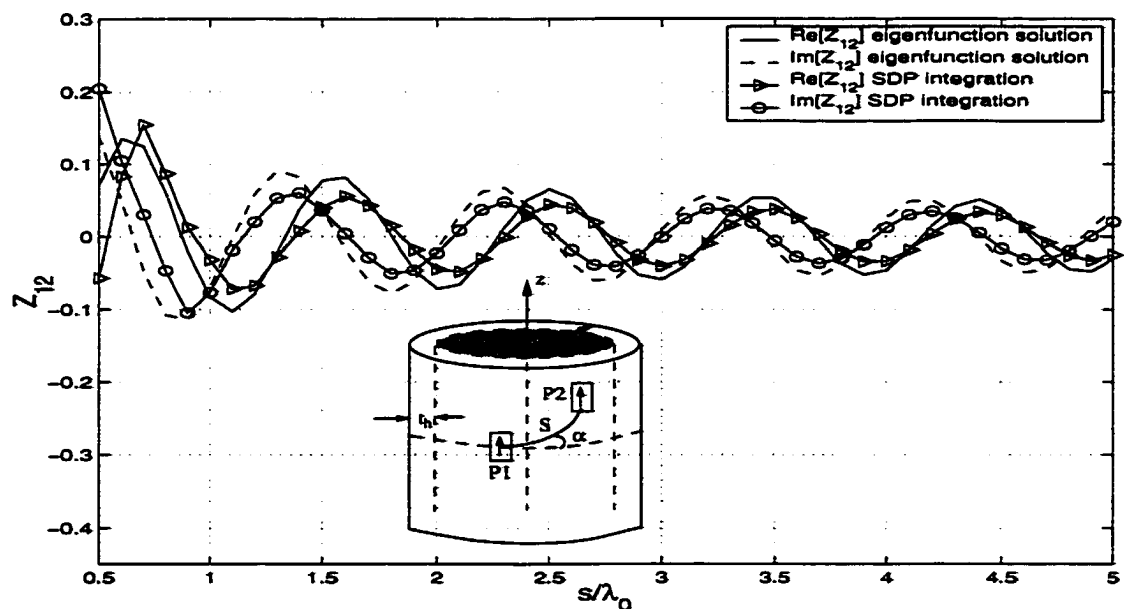


(b) coupling between a z - and a ρ -directed sources

Figure 2.21: Real and imaginary parts of the mutual coupling between a tangential and a ρ -directed current sources for a coated cylinder with $\alpha = 2.0184\lambda_0$, $t_h = 0.0214\lambda_0$, $\epsilon_r = 2.94$



(a) coupling between two ϕ -directed sources



(b) coupling between two z -directed sources

Figure 2.22: Real and imaginary parts of the mutual coupling between two tangential current sources for a coated cylinder with $a = 3.0\lambda_0$, $t_h = 0.06\lambda_0$, $\epsilon_r = 3.25$, $\alpha = 70^\circ$

CHAPTER 3

Paraxial Space-Domain Formulation for Surface Fields on Dielectric Coated Circular Cylinder

3.1 Introduction

The aforementioned Green's function representations (Chapter 2) fail around the paraxial (i.e. near axial) region of the coated circular cylinder due to the mapping given by (2.38). Furthermore, the planar approximations yield inaccurate results in this region as the distance between the source and observation points becomes large since the curvature effects are not taken into account. In this chapter, a novel space-domain representation for the surface fields created by an elementary current source will be presented. These new expressions are valid along the paraxial region and can be made valid away from the paraxial region with some minor modifications. The essence of this formulation is based on the fact that the circumferentially propagating series representation of the appropriate Green's function is periodic in one of its variables, and hence can be approximated by a Fourier series where the coefficients of this series expansion can be efficiently obtained by numerical integration. Based on numerical experimentation, it appears that only the two leading terms of the expansion are necessary in most cases. Furthermore, the accuracy of the Green's

function as well as the ease of its evaluation are determined by the type of algorithm used to calculate the Fourier series coefficients. In Section 3.2, a formulation of the approximate Green's function is discussed. Calculation of the surface fields using these space-domain approximate Green's function representations are explained in Section 3.3 along with the evaluation of the integrals. Numerical results illustrating the accuracy, limitations and some other features of this representation will be presented in Section 3.4.

3.2 Development of the Approximate Green's Function

The approximate space-domain formulation of the surface fields which are valid along the paraxial region are obtained using the algorithm depicted in Figure 3.1. For the sake of clarity, the surface field component in the l -direction ($l = \phi, z$ or ρ) due to a u -directed source ($u = \phi, z$ or ρ) (except the case $l = \rho$ and $u = \rho$), originally given in (2.37) is written again in this chapter, namely

$$E_l(z, \phi) \approx \frac{1}{2\pi} \int_{-\infty}^{\infty} \int_{-\infty-j\epsilon}^{\infty-j\epsilon} \frac{G_{lu}(\nu, k_z)}{2\pi d} e^{-jk_z(z-z')} e^{-j\nu(\phi-\phi')} d\nu dk_z \quad (3.1)$$

where only the leading term of the circumferentially propagating series representation is kept in (3.1).

The integral given by (3.1) can be expressed in polar coordinates by performing the following transformations [59]

$$k_z = -\zeta \cos \psi ; \nu = \mu d \text{ where } \mu = -\zeta \sin \psi , \quad (3.2)$$

and making use of the following geometrical transformations [59]

$$r_l = d(\phi - \phi') = s \sin \delta ; (z - z') = s \cos \delta \quad (3.3)$$

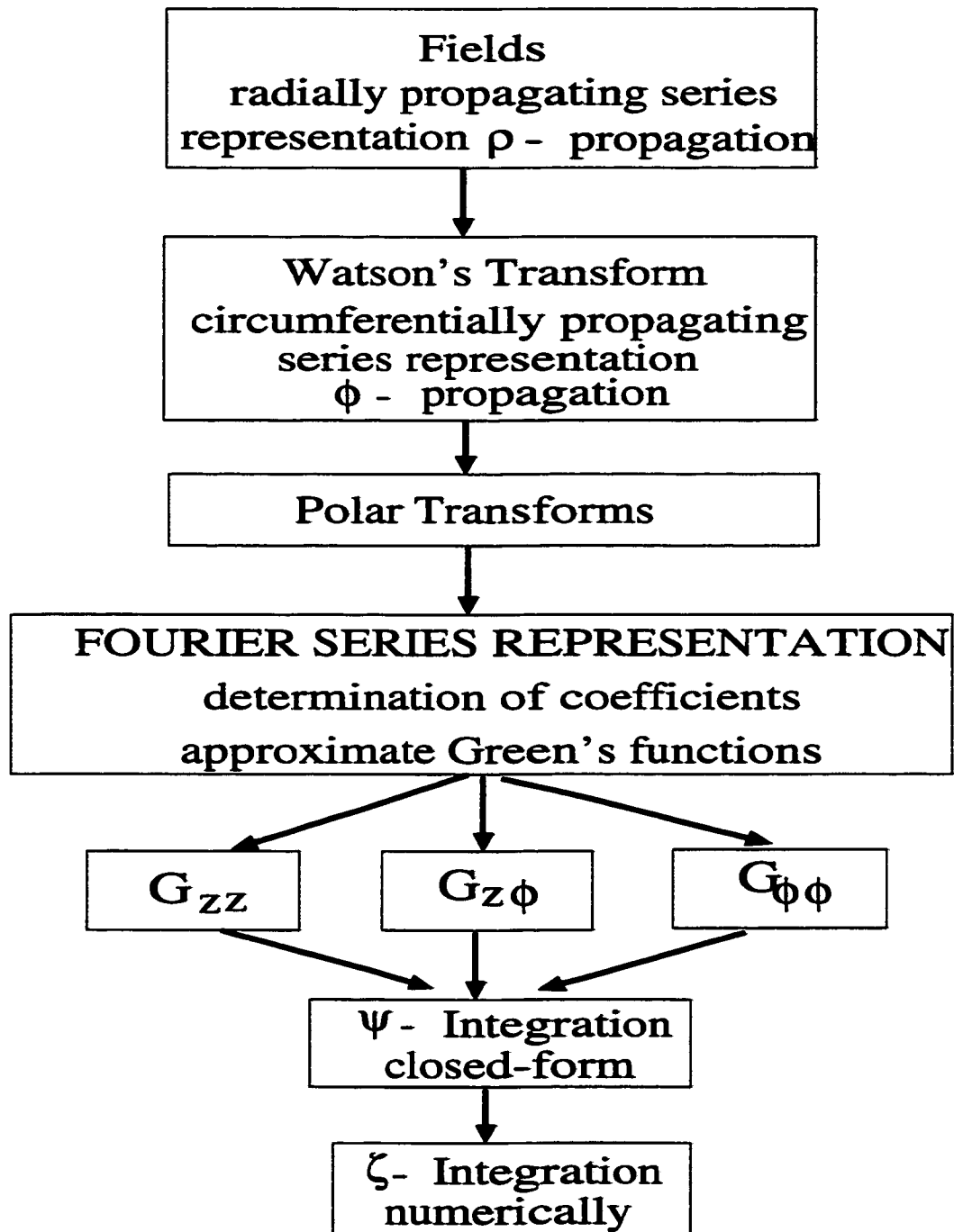


Figure 3.1: The algorithm used to calculate the surface fields accurate around the paraxial region

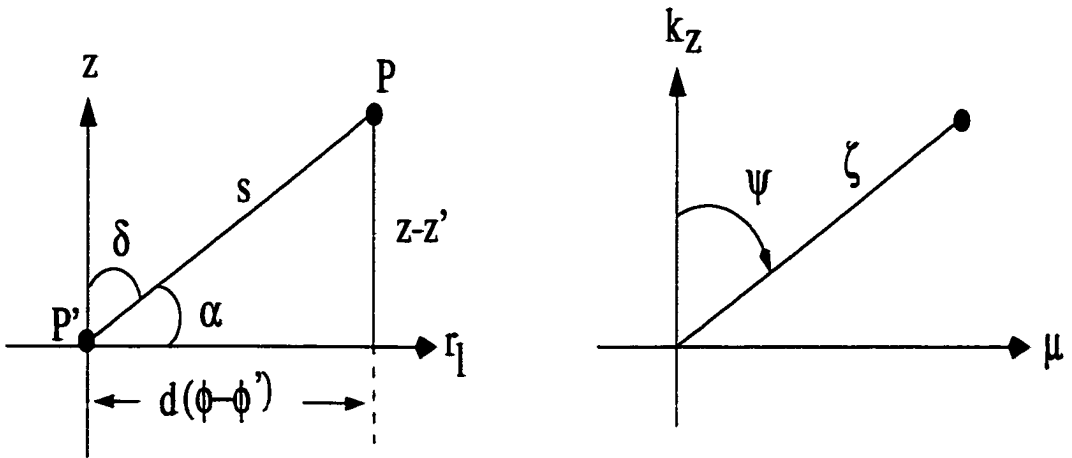


Figure 3.2: Space (s, δ) and spectral (ζ, ψ) polar coordinates after [53]

where the definitions of ψ , δ , s and ζ are shown in Figure 3.2. The result of this procedure is written as

$$E_l(s, \delta) \approx \frac{1}{2\pi} \int_0^{2\pi} \int_0^\infty \frac{G_{lu}(\zeta, \psi)}{2\pi} e^{j\zeta s \cos(\psi - \delta)} \zeta d\zeta d\psi. \quad (3.4)$$

3.2.1 Tangential Components

As in the previous chapter, the tangential components of the surface fields due to the tangential current sources are analyzed first. The ρ -related components of the dyadic Green's function are briefly discussed in Section 3.2.2.

An analysis with respect to ψ reveals that the tangential components of the dyadic Green's function are periodic with π , i.e.

$$G_{zz}(\zeta, \psi) = G_{zz}(\zeta, \psi + \pi) \quad (3.5)$$

$$G_{z\phi}(\zeta, \psi) = G_{z\phi}(\zeta, \psi + \pi) \quad (3.6)$$

$$G_{\phi z}(\zeta, \psi) = G_{\phi z}(\zeta, \psi + \pi) \quad (3.7)$$

and

$$G_{\phi\phi}(\zeta, \psi) = G_{\phi\phi}(\zeta, \psi + \pi). \quad (3.8)$$

Therefore, the Green's function components can be approximated by a Fourier series.

Using (C.1), $G_{lu}(\zeta, \psi)$ can be written as (see Appendix C for details)

$$G_{lu}(\zeta, \psi) = a_0(\zeta) + \sum_{n=1}^{\infty} a_n(\zeta) \cos n2\psi + \sum_{n=1}^{\infty} b_n(\zeta) \sin n2\psi \quad (3.9)$$

where $\omega_0 = 2$ and $a_0(\zeta)$, $a_n(\zeta)$ and $b_n(\zeta)$ are coefficients given by

$$a_0(\zeta) = \frac{1}{\pi} \int_T G_{lu}(\zeta, \psi) d\psi \quad (3.10)$$

$$a_n(\zeta) = \frac{2}{\pi} \int_T G_{lu}(\zeta, \psi) \cos n2\psi d\psi \quad (3.11)$$

and

$$b_n(\zeta) = \frac{2}{\pi} \int_T G_{lu}(\zeta, \psi) \sin n2\psi d\psi. \quad (3.12)$$

As seen in (3.10)-(3.12), the Fourier series coefficients are only functions of ζ . This simplifies the surface field calculations significantly since, in the approximate Green's function representations, the ζ and ψ variables are separated. On the other hand, the integrations given in (3.10)-(3.12) are calculated in closed-form under certain approximations. In the next three subsections, the evaluation of $G_{zz}(\zeta, \psi)$, $G_{z\phi}(\zeta, \psi) = G_{\phi z}(\zeta, \psi)$ and $G_{\phi\phi}(\zeta, \psi)$ components are explained, respectively. Although the essence of the method is the same for all components, each of them has certain unique features and hence, has been treated slightly different as discussed in the following sections.

$G_{zz}(\zeta, \psi)$ Component

In addition to its periodicity, $G_{zz}(\zeta, \psi)$ is even with respect to ψ , i.e.

$$G_{zz}(\zeta, \psi) = G_{zz}(\zeta, -\psi) \quad (3.13)$$

yielding $b_n = 0$ (see Appendix C). Furthermore, based on numerical experimentation, including the leading two terms gives enough accuracy for this component. Consequently, the Fourier series coefficients are given by

$$a_{0_{zz}} = \frac{1}{\pi} \int_0^\pi G_{zz}(\zeta, \psi) d\psi \quad (3.14a)$$

$$a_{1_{zz}} = \frac{4}{\pi} \int_0^\pi G_{zz}(\zeta, \psi) \cos 2\psi d\psi \quad (3.14b)$$

where the even symmetry of $G_{zz}(\zeta, \psi)$ is used (C.6). The coefficients $a_{0_{zz}}$ and $a_{1_{zz}}$ are calculated using numerical integration, namely,

$$a_{0_{zz}}(\zeta) \approx \sum_{p=1}^P w_p G_{zz}(\zeta, \psi_p) \quad (3.15a)$$

$$a_{1_{zz}}(\zeta) \approx \sum_{p=1}^P w_p G_{zz}(\zeta, \psi_p) \cos 2\psi_p \quad (3.15b)$$

where w_p are the appropriate weights. If the abscissas (ψ_p) are chosen to be at $\psi_p = 0, \pi/2, \pi$, the approximate $G_{zz}(\zeta, \psi_p)$ is significantly simplified allowing a simpler numerical integration with respect to ζ in (3.4). Therefore, using a 3-point trapezoidal rule [67] in the interval $[0, \pi]$ in (3.15), the coefficients $a_{0_{zz}}$ and $a_{1_{zz}}$ are given by

$$a_{0_{zz}}(\zeta) \approx \frac{1}{2} \left[G_{zz}(\zeta, \psi = 0) + G_{zz}(\zeta, \psi = \frac{\pi}{2}) \right] \quad (3.16a)$$

$$a_{1_{zz}}(\zeta) \approx \frac{1}{2} \left[G_{zz}(\zeta, \psi = 0) - G_{zz}(\zeta, \psi = \frac{\pi}{2}) \right] \quad (3.16b)$$

where the fact $G_{zz}(\zeta, \psi = \pi) = G_{zz}(\zeta, \psi = 0)$ is made use. Substituting (3.16) into (3.9), the approximate $G_{zz}(\zeta, \psi)$ denoted with $G_{zz}^a(\zeta)$ is given by

$$G_{zz}^a(\zeta, \psi) \approx G_{zz}(\zeta, \psi = \frac{\pi}{2}) + \left[G_{zz}(\zeta, \psi = 0) - G_{zz}(\zeta, \psi = \frac{\pi}{2}) \right] \left(\frac{1 + \cos 2\psi}{2} \right). \quad (3.17)$$

The same approximate form is given in [59] (though, it is not clear how this solution was obtained). This approximate Green's function is supposed to be exact at $\psi = 0$ and $\psi = \pi/2$. As will be seen from the numerical results, using (3.17) in (3.4) yields accurate results around the paraxial region ($\delta \rightarrow 0$ or $\alpha \rightarrow \pi/2$). However, results become inaccurate as δ becomes large for large s values.

$G_{\phi z}(\zeta, \psi) = G_{z\phi}(\zeta, \psi)$ Component

First the $G_{\phi z}(\zeta, \psi)$ component, which is an odd function with respect to ψ , is written as

$$G_{\phi z}(\zeta, \psi) = \frac{\zeta^2 \sin 2\psi}{2} \tilde{G}_{\phi z}(\zeta, \psi) \quad (3.18)$$

where $\tilde{G}_{\phi z}(\zeta, \psi)$ is $G_{\phi z}(\zeta, \psi)$ as defined in (2.18b) except the product $\frac{\nu}{d} k_z = \mu k_z = \frac{\zeta^2 \sin 2\psi}{2}$ is excluded. Next, only the $\tilde{G}_{\phi z}(\zeta, \psi)$ part, which becomes an even function, is approximated with a Fourier series. However, unlike the $G_{zz}(\zeta, \psi)$ case, including only the leading term gives enough accuracy. Therefore, $a_{0_{\phi z}}$ is given by

$$a_{0_{\phi z}} = \frac{1}{\pi} \int_T \tilde{G}_{\phi z}(\zeta, \psi) d\psi. \quad (3.19)$$

Similar to the $G_{zz}(\zeta, \psi)$ component, the Fourier series coefficient is calculated using a numerical integration. The integration interval is chosen as $[0, \pi]$ and the integral is performed using a 2-point trapezoidal rule (so that the approximate Green's function is significantly simplified and has still enough accuracy), then

$$a_{0_{\phi z}} \approx \frac{1}{\pi} \left[\frac{\pi}{2} \left(\tilde{G}_{\phi z}(\zeta, \psi = 0) + \tilde{G}_{\phi z}(\zeta, \psi = \pi) \right) \right] = \tilde{G}_{\phi z}(\zeta, \psi = 0) \quad (3.20)$$

(where the periodicity of $\tilde{G}_{\phi z}(\zeta, \psi)$ is used) yielding an approximate $G_{\phi z}^a(\zeta, \psi)$ given by

$$G_{\phi z}^a(\zeta, \psi) \approx \frac{\zeta^2 \sin 2\psi}{2} \tilde{G}_{\phi z}(\zeta, \psi = 0) \quad (3.21)$$

and is exact at $\psi = 0$. Numerical results reveal that if we use (3.21) in (3.4), accurate results are obtained around the paraxial region $\delta \rightarrow 0$ ($\alpha \rightarrow \pi/2$), but the accuracy gets worse as δ increases for large separations (large s).

$G_{\phi\phi}(\zeta, \psi)$ Component

Evaluation of the $G_{\phi\phi}(\zeta, \psi)$ component differs from the others because the methods used for the calculation of the components $G_{zz}(\zeta, \psi)$ and $G_{z\phi}(\zeta, \psi)$ did not yield results with enough accuracy for this component. Therefore, $G_{\phi\phi}(\zeta, \psi)$ is written as the sum of **planar + curvature correction** terms as explained in detail in Appendix D, namely,

$$G_{\phi\phi}(\zeta, \psi) \approx G_{uu}^p(\zeta, \psi) + G_{\phi\phi}^{cc}(\zeta, \psi) \quad (3.22)$$

where $u = x$ or y and p denotes “planar”, whereas cc stands for “curvature correction”. The planar term $G_{uu}^p(\zeta, \psi)$, which is explicitly given by (D.4) can be written as

$$G_{uu}^p(\zeta, \psi) = G_{uu}^{p1}(\zeta) - G_{uu}^{p2}(\zeta) \left(\frac{1 - \cos 2\psi}{2} \right) \zeta^2. \quad (3.23)$$

Note that the planar term $G_{uu}^p(\zeta, \psi)$ is already written as a two term Fourier series in ψ and no further expansions are needed. On the other hand, the curvature correction term $G_{\phi\phi}^{cc}(\zeta, \psi)$, which is explicitly given by (D.5)-(D.15) is an even function and periodic with $T = \pi$ with respect to ψ . This term is evaluated in the same fashion

as $G_{zz}(\zeta, \psi)$, namely, due to the even symmetry of $G_{\phi\phi}^{cc}(\zeta, \psi)$, $b_n = 0$ and based on numerical experimentation, including the first two terms of the Fourier series expansion gives enough accuracy. After extensive testing of different numerical integration routines and number of sample points, accurate numerical results are obtained for $a_{0_{\phi\phi}}$ and $a_{1_{\phi\phi}}$ with the following algorithm:

$$a_{0_{\phi\phi}} \approx \frac{1}{4} \left[G_{\phi\phi}^{cc}(\zeta, \psi = 0) + G_{\phi\phi}^{cc}(\zeta, \psi = \frac{\pi}{2}) \right] \quad (3.24a)$$

$$a_{1_{\phi\phi}} \approx \frac{1}{4} \left[G_{\phi\phi}^{cc}(\zeta, \psi = 0) - G_{\phi\phi}^{cc}(\zeta, \psi = \frac{\pi}{2}) \right] \quad (3.24b)$$

where we made use of $G_{\phi\phi}^{cc}(\zeta, \psi = \pi) = G_{\phi\phi}^{cc}(\zeta, \psi = 0)$. As a result of this process, the final approximate expression for the curvature correction term becomes

$$\begin{aligned} G_{\phi\phi}^{a,cc}(\zeta, \psi) &\approx \frac{1}{2} \left\{ G_{\phi\phi}^{cc}(\zeta, \psi = 0) \right. \\ &+ \left. \left[G_{\phi\phi}^{cc}(\zeta, \psi = \frac{\pi}{2}) - G_{\phi\phi}^{cc}(\zeta, \psi = 0) \right] \left(\frac{1 - \cos 2\psi}{2} \right) \right\}. \end{aligned} \quad (3.25)$$

and combining (3.23) with (3.25), the approximate Green's function $G_{\phi\phi}^a(\zeta, \psi)$ is given by

$$\begin{aligned} G_{\phi\phi}^a(\zeta, \psi) &\approx G_{uu}^{p1}(\zeta) + \frac{1}{2} G_{\phi\phi}^{cc}(\zeta, \psi = 0) + \left\{ -\zeta^2 G_{uu}^{p2}(\zeta) \right. \\ &+ \left. \frac{1}{2} \left[G_{\phi\phi}^{cc}(\zeta, \psi = \frac{\pi}{2}) - G_{\phi\phi}^{cc}(\zeta, \psi = 0) \right] \left(\frac{1 - \cos 2\psi}{2} \right) \right\}. \end{aligned} \quad (3.26)$$

As in the $G_{zz}(\zeta, \psi)$ case, using (3.26) in (3.4) yields accurate results around the paraxial region ($\delta \rightarrow 0$ or $\alpha \rightarrow \pi/2$), however they lose accuracy as δ becomes large for large s values.

3.2.2 Normal Components

As mentioned in the previous chapter, cylindrical antennas fed via a probe require the ρ -related components of the dyadic Green's function to determine the incident field as well as the input impedance.

An analysis with respect to ψ reveals that the ρ -related components of the dyadic Green's function are periodic with 2π , i.e.

$$G_{\rho z}(\zeta, \psi) = G_{\rho z}(\zeta, \psi + 2\pi) \quad (3.27)$$

and

$$G_{\rho \phi}(\zeta, \psi) = G_{\rho \phi}(\zeta, \psi + 2\pi). \quad (3.28)$$

Therefore, as in the case of tangential components, these components can be approximated by a Fourier series, namely,

$$G_{lu}(\zeta, \psi) = a_0(\zeta) + \sum_{n=1}^{\infty} a_n(\zeta) \cos n\psi + \sum_{n=1}^{\infty} b_n(\zeta) \sin n\psi \quad (3.29)$$

where $\omega_0 = 1$ and $a_0(\zeta)$, $a_n(\zeta)$ and $b_n(\zeta)$ are coefficients given by

$$a_0(\zeta) = \frac{1}{\pi} \int_T G_{lu}(\zeta, \psi) d\psi \quad (3.30)$$

$$a_n(\zeta) = \frac{2}{\pi} \int_T G_{lu}(\zeta, \psi) \cos n\psi d\psi \quad (3.31)$$

and

$$b_n(\zeta) = \frac{2}{\pi} \int_T G_{lu}(\zeta, \psi) \sin n\psi d\psi. \quad (3.32)$$

Similar to the tangential components, the Fourier series coefficients are only functions of ζ which simplifies the surface field calculations significantly because, the ζ

and ψ variables are separated in the approximate Green's function representations. Although the essence of the method is the same as that of the tangential components, numerical calculation of the Fourier series coefficients are not done in this dissertation. Based on the fact that mutual coupling between a normal component and a tangential component is weaker than the mutual coupling between two tangential components, the interactions between two widely separated elements can be ignored. On the other hand, when the separation between the source and observation point is less than $2\lambda_0$, planar approximations yield enough accuracy along the paraxial region for relatively large cylinders ($d > 1.5\lambda_0$).

3.3 Calculation of Surface Fields

Equations (3.17), (3.21) and (3.26) are the components of the approximate space domain Green's function representation which are substituted into (3.4) to find the surface fields due to tangential current elements located on the coating. In all components, the common feature is the separation of the ζ and ψ variables which allows the closed-form integration with respect to ψ in (3.4). Substituting (3.17), (3.21) and (3.26) into (3.4), the surface fields can be written as

$$E_{zz}(\delta, s) \approx \frac{1}{2\pi} \left[\int_0^\infty G_{zz}(\zeta, \psi = \frac{\pi}{2}) \left\{ \int_0^{2\pi} \frac{e^{j\zeta s \cos(\psi-\delta)}}{2\pi} d\psi \right\} \zeta d\zeta + \int_0^\infty (G_{zz}(\zeta, \psi = 0) - G_{zz}(\zeta, \psi = \frac{\pi}{2})) \left\{ \int_0^{2\pi} \left(\frac{1 + \cos 2\psi}{4\pi} \right) e^{j\zeta s \cos(\psi-\delta)} d\psi \right\} \zeta d\zeta \right] \quad (3.33)$$

$$E_{\phi z}(\delta, s) \approx \frac{1}{2\pi} \int_0^\infty \bar{G}_{\phi z}(\zeta, \psi = 0) \zeta^2 \left\{ \int_0^{2\pi} \frac{\sin 2\psi}{4\pi} e^{j\zeta s \cos(\psi-\delta)} d\psi \right\} \zeta d\zeta \quad (3.34)$$

and

$$\begin{aligned}
E_{\phi\phi}(\delta, s) \approx & \frac{1}{2\pi} \left[\int_0^\infty G_{uu}^{pl}(\zeta) \left\{ \int_0^{2\pi} \frac{e^{j\zeta s \cos(\psi-\delta)}}{2\pi} d\psi \right\} \zeta d\zeta \right. \\
& - \int_0^\infty G_{uu}^2(\zeta) \zeta^2 \left\{ \int_0^{2\pi} \left(\frac{1 - \cos 2\psi}{4\pi} \right) e^{j\zeta s \cos(\psi-\delta)} d\psi \right\} \zeta d\zeta \\
& + \frac{1}{2} \int_0^\infty G_{\phi\phi}^{cc}(\zeta, \psi = 0) \left\{ \int_0^{2\pi} \frac{e^{j\zeta s \cos(\psi-\delta)}}{2\pi} d\psi \right\} \zeta d\zeta \\
& \left. + \frac{1}{2} \int_0^\infty \left[G_{\phi\phi}^{cc}(\zeta, \psi = \frac{\pi}{2}) - G_{\phi\phi}^{cc}(\zeta, \psi = 0) \right] \right. \\
& \left. \left\{ \int_0^{2\pi} \left(\frac{1 - \cos 2\psi}{4\pi} \right) e^{j\zeta s \cos(\psi-\delta)} d\psi \right\} \zeta d\zeta \right]. \quad (3.35)
\end{aligned}$$

These ψ integrals are calculated in closed-form [59], namely

$$\int_0^{2\pi} \frac{e^{j\zeta s \cos(\psi-\delta)}}{2\pi} d\psi = J_0(\zeta s) \quad (3.36)$$

$$\int_0^{2\pi} \left(\frac{1 - \cos 2\psi}{4\pi} \right) e^{j\zeta s \cos(\psi-\delta)} d\psi = -\frac{1}{\zeta^2} \frac{\partial^2}{\partial r_l^2} J_0(\zeta s) \quad (3.37)$$

$$\int_0^{2\pi} \left(\frac{1 + \cos 2\psi}{4\pi} \right) e^{j\zeta s \cos(\psi-\delta)} d\psi = -\frac{1}{\zeta^2} \frac{\partial^2}{\partial z^2} J_0(\zeta s) \quad (3.38)$$

and

$$\int_0^{2\pi} \frac{\sin 2\psi}{4\pi} e^{j\zeta s \cos(\psi-\delta)} d\psi = -\frac{1}{\zeta^2} \frac{\partial^2}{\partial z \partial r_l} J_0(\zeta s) \quad (3.39)$$

where $J_0(\zeta s)$ is the zeroth order Bessel function, $r_l = d(\phi - \phi') = s \sin \delta$, $z = s \cos \delta$ and $s = \sqrt{z^2 + r_l^2}$. Finally, substituting (3.36)-(3.39) into (3.33)-(3.35), the following

expressions are obtained for the surface fields:

$$E_{zz}(\delta, s) \approx \frac{-Z_0}{2\pi k_0} \left\{ k_0^2 P(s) + \frac{\partial^2}{\partial z^2} [P(s) - Q(s)] \right\} \quad (3.40)$$

$$E_{\phi z}(\delta, s) \approx \frac{-Z_0}{2\pi k_0} \frac{\partial^2}{\partial z \partial l} \{M(s) - R(s)\} \quad (3.41)$$

and

$$\begin{aligned} E_{\phi\phi}(\delta, s) \approx & \frac{-Z_0}{2\pi k_0} \left\{ k_0^2 U(s) + \frac{\partial^2}{\partial r_l^2} \left[U(s) - \frac{\epsilon_r - 1}{\epsilon_r} W(s) \right] \right\} \\ & + \frac{j Z_0}{2\pi k_0} \left\{ S(s) + \frac{\partial^2}{\partial r_l^2} T(s) \right\} \end{aligned} \quad (3.42)$$

where $P(s)$, $Q(s)$, $M(s)$, $R(s)$, $U(s)$, $W(s)$, $S(s)$, $T(s)$ are given by (E.1a) through (E.23), respectively, in Appendix E. Note that, $U(s)$ and $W(s)$ are exactly the same special functions defined in [7] (special functions used for the Sommerfeld integral representation for the single layer microstrip dyadic Green's function) for the planar case.

The integrals are evaluated numerically along the real axis using a Gaussian quadrature algorithm. Evaluation of $U(s)$ and $W(s)$ is explained in detail in [7], whereas the details about the evaluation of $P(s)$ and $Q(s)$ are given in [59]. Both [7] and [59] use an envelope extraction technique to overcome the difficulties in the numerical integration arising from their oscillatory behavior as well as slowly decaying amplitude. Furthermore, the singularities which are on the real axis (for lossless case) along the path of integration are handled by regularizing the integrands. Additional details, such as the limiting values and the regularization process, can be found in [59] for $P(s)$ and $Q(s)$ and in [7] for $U(s)$ and $W(s)$. Regarding $M(s)$, it has a behavior similar to the function $Q(s)$ (the pole location ζ_p is the same for both functions

and the integrands of both functions show a similar behavior for large ζ values) and hence, a similar approach is followed in its evaluation. The main difference between these two functions is the limiting value of their integrands (excluding $J_0(\zeta s)$) when $\zeta \rightarrow \infty$. This limiting value for the function $M(s)$ is $\frac{i}{\epsilon_r+1}$, whereas it is given as $\frac{i\epsilon_r-1}{2\epsilon_r+1}$ for the function $Q(s)$ as explained in [59]. Finally, the numerical evaluation of the special functions $R(s)$, $S(s)$ and $T(s)$ is slightly simpler. The integrands of these functions (excluding $J_0(\zeta s)$) show a $\frac{1}{\zeta^2}$ type variation for large ζ values and they are relatively smooth compared to the aforementioned functions. Therefore, the use of an envelope extraction technique to integrate these functions is not required. However, these functions exhibit a pole on the real axis (like $Q(s)$) which is handled again by regularizing their integrands. Barkeshli [7] explains how the integrands are regularized in detail. Note that a Newton-Raphson method [69] is used to find the singularities on the real axis for the aforementioned functions.

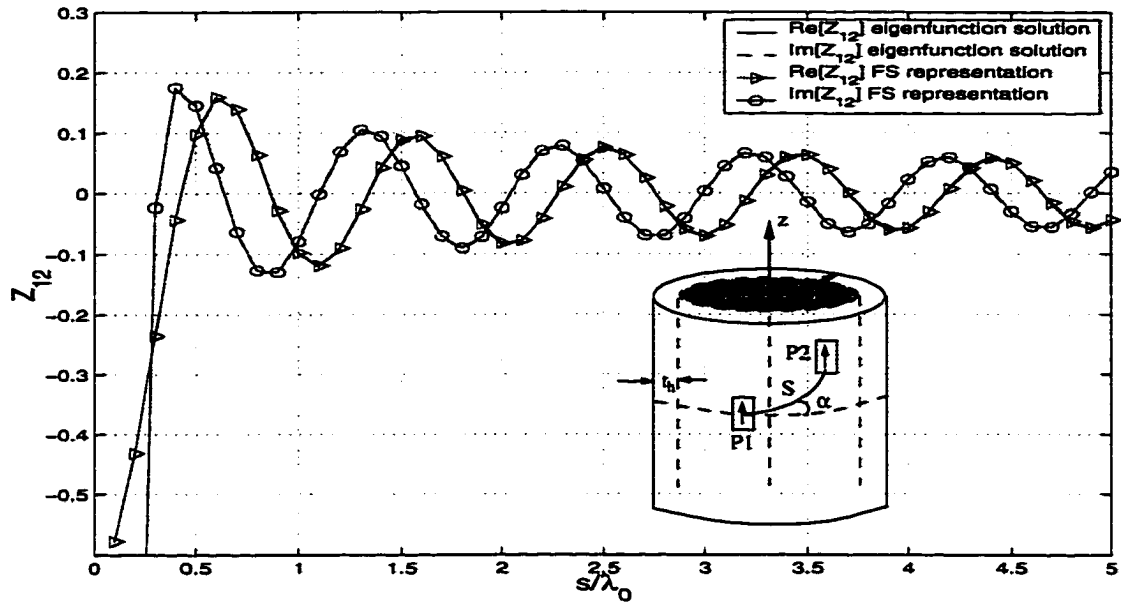
3.4 Numerical Results

As was done in the previous chapter, numerical results for the mutual coupling between two tangential modes are obtained using (3.40)-(3.42) and compared with the traditional eigenfunction solution given by (2.15) for various size of cylinders with different coating properties. The same type of current distribution (given by (2.88)) with the same dimensions ($0.05\lambda_0$ (along the direction of current) by $0.02\lambda_0$) as in Chapter 2 is chosen in this chapter to obtain numerical results. Figure 3.3 shows the real and imaginary parts of the mutual coupling between two identical z -directed current sources for a cylinder having an inner radius $a = 3\lambda_0$, thickness $t_h = 0.06\lambda_0$ and $\epsilon_r = 3.25$. The angle α is 90° and 70° , respectively (with $\alpha = 90^\circ$ being the

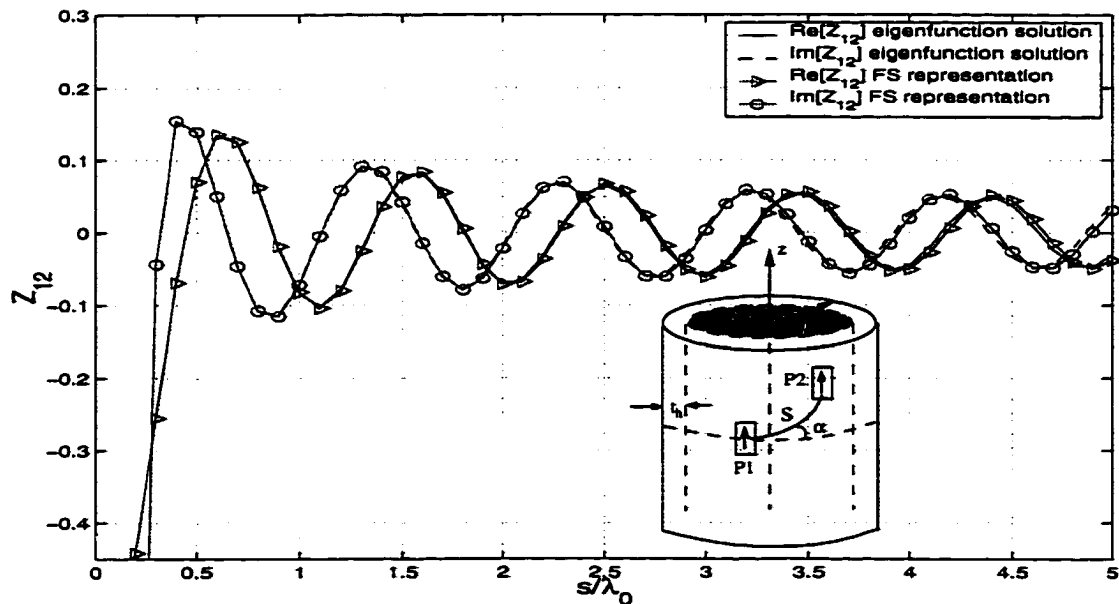
axial direction). Similar results are depicted in Figure 3.4 for another cylinder with $\epsilon_r = 2.94$, $a = 2.0184\lambda_0$ and $t_h = 0.0216\lambda_0$ where the angle α is chosen to be 85° and 75° , respectively. For the same cylinders, the real and imaginary parts of the mutual coupling between and a ϕ - and a z -directed current sources are depicted in Figure 3.5 and Figure 3.6, respectively, where $\alpha = 88^\circ$ and $\alpha = 75^\circ$ for the larger cylinder ($a = 3\lambda_0$) whereas, $\alpha = 85^\circ$ and $\alpha = 70^\circ$ for the relatively small one ($a = 2.0184\lambda_0$). Figures 3.7 and 3.8 show the real and imaginary parts of the mutual coupling between two identical ϕ -directed current sources on the larger cylinder for $\alpha = 90^\circ$, 88° , 85° and 70° . Similar results have been depicted in Figure 3.9 for the relatively smaller cylinder for $\alpha = 80^\circ$ and 55° values. As seen from these numerical results, the surface field expressions obtained using the Fourier series representation of the appropriate Green's function yield very accurate results along the paraxial region for both arbitrarily small and large separations. When α becomes small (i.e. away from the paraxial region), the paraxial space-domain formulation lose accuracy for large separations between the source and observation points. For example, in Figure 3.3(b), the paraxial space-domain solution starts to lose its accuracy when the separation s is larger than $4 - 4.5\lambda_0$. Similar behavior can be observed for the other examples given in this section.

3.4.1 Expressions for regions away from the paraxial region

The new space-domain representations, introduced above, can be made valid away from the paraxial region by changing either the numerical integration routine or the integration interval (or both) used to calculate the Fourier series coefficients. For the $G_{\phi z}(\zeta, \psi)$ component of the dyadic Green's function, if the integration interval is

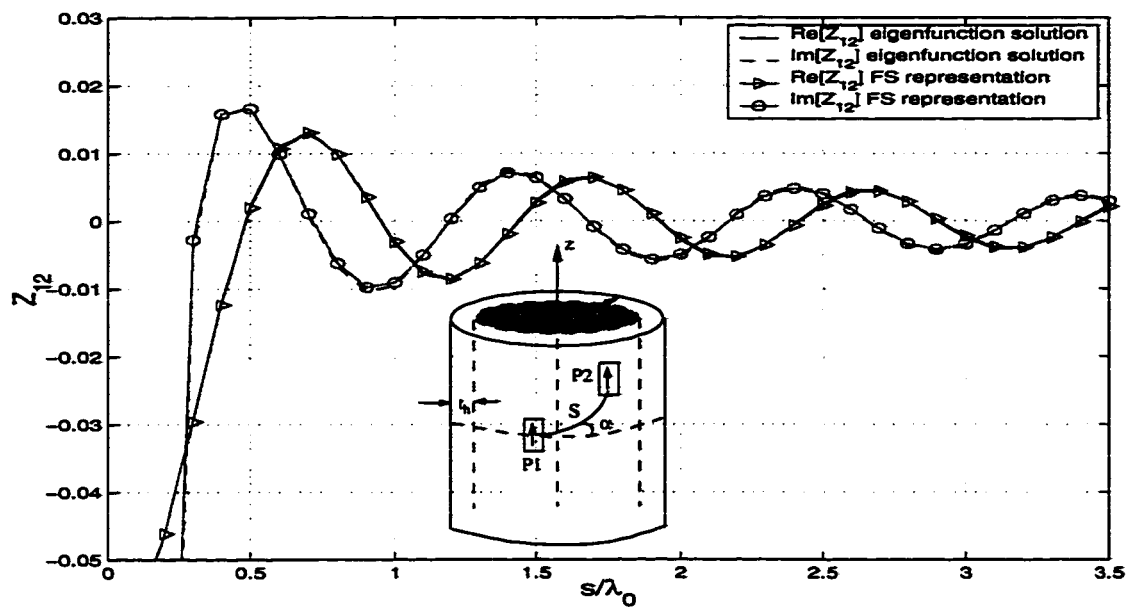


(a) $\alpha = 3\lambda_0$, $t_h = 0.06\lambda_0$, $\epsilon_r = 3.25$, $\alpha = 90^\circ$

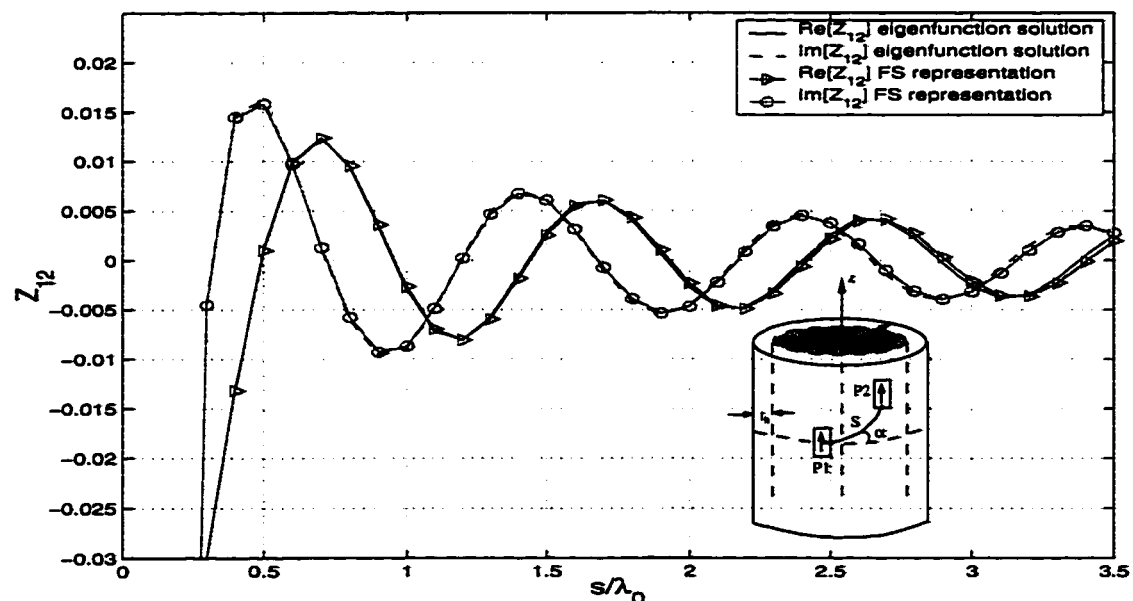


(b) $\alpha = 3\lambda_0$, $t_h = 0.06\lambda_0$, $\epsilon_r = 3.25$, $\alpha = 70^\circ$

Figure 3.3: Real and imaginary parts of the mutual coupling between two identical z -directed current sources.

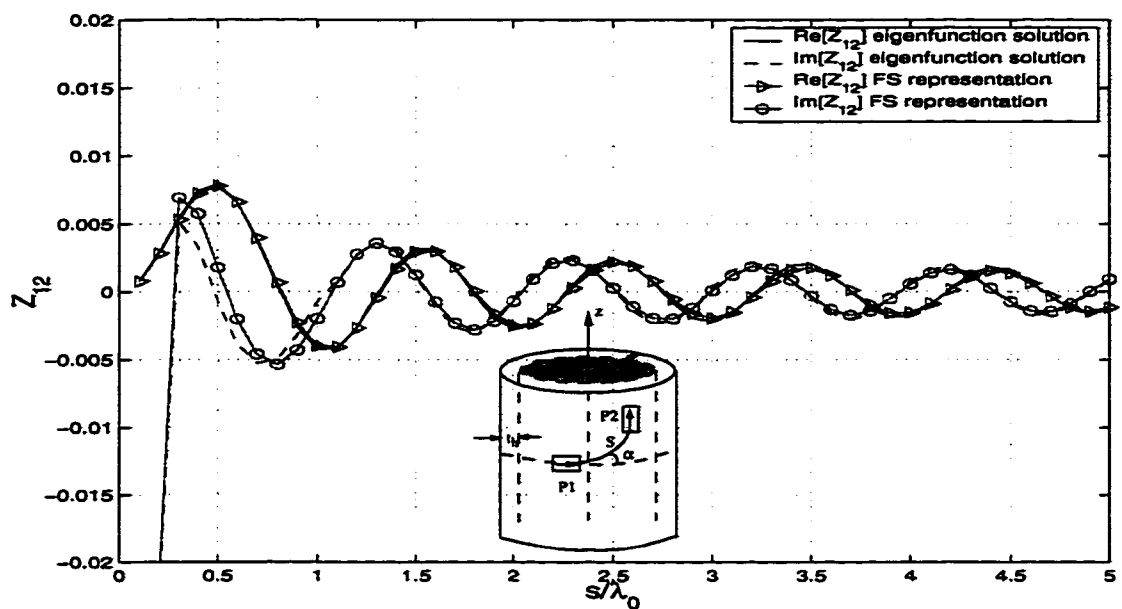


(a) $a = 2.0184\lambda_0, t_h = 0.0216\lambda_0, \epsilon_r = 2.94, \alpha = 85^\circ$

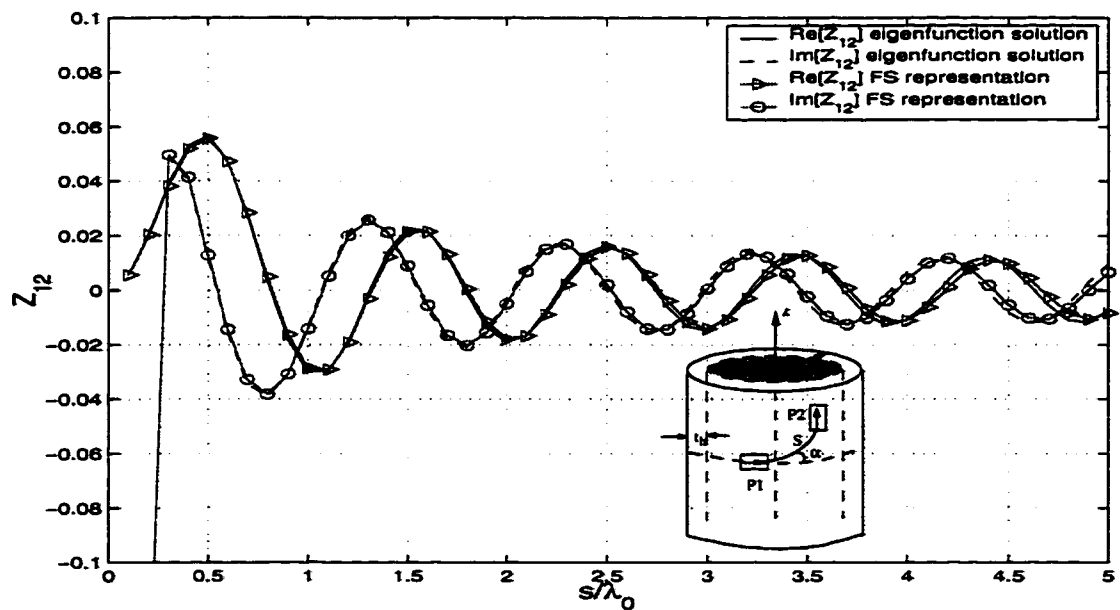


(b) $a = 2.0184\lambda_0, t_h = 0.0216\lambda_0, \epsilon_r = 2.94, \alpha = 75^\circ$

Figure 3.4: Real and imaginary parts of the mutual coupling between two identical z-directed current sources.

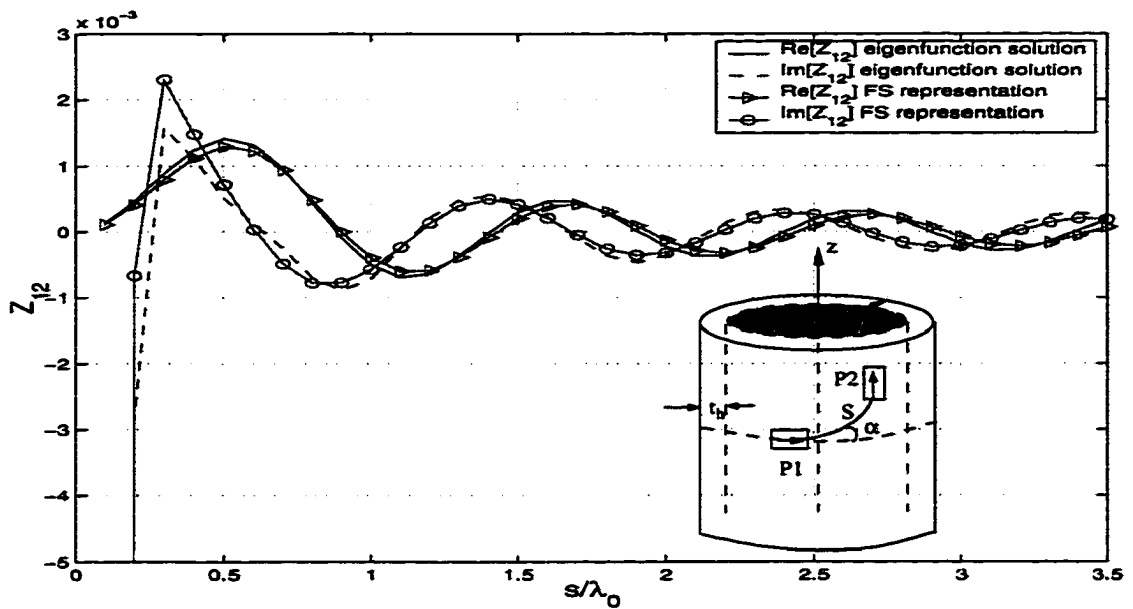


(a) $\alpha = 3\lambda_0, t_h = 0.06\lambda_0, \epsilon_r = 3.25, \alpha = 88^\circ$

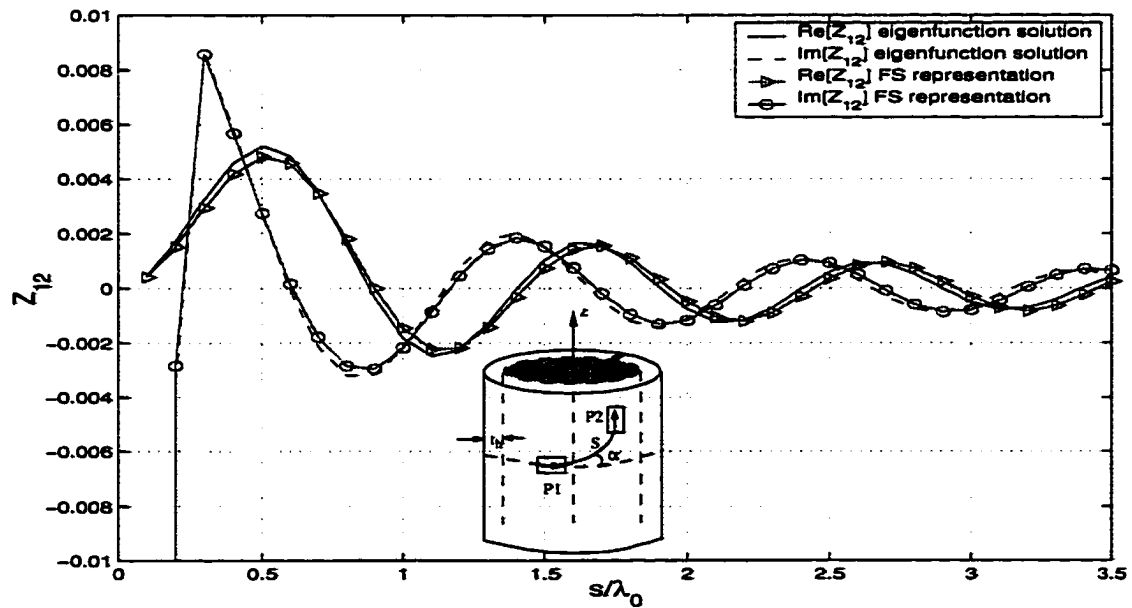


(b) $\alpha = 3\lambda_0, t_h = 0.06\lambda_0, \epsilon_r = 3.25, \alpha = 75^\circ$

Figure 3.5: Real and imaginary parts of the mutual coupling between ϕ - and z -directed current sources.

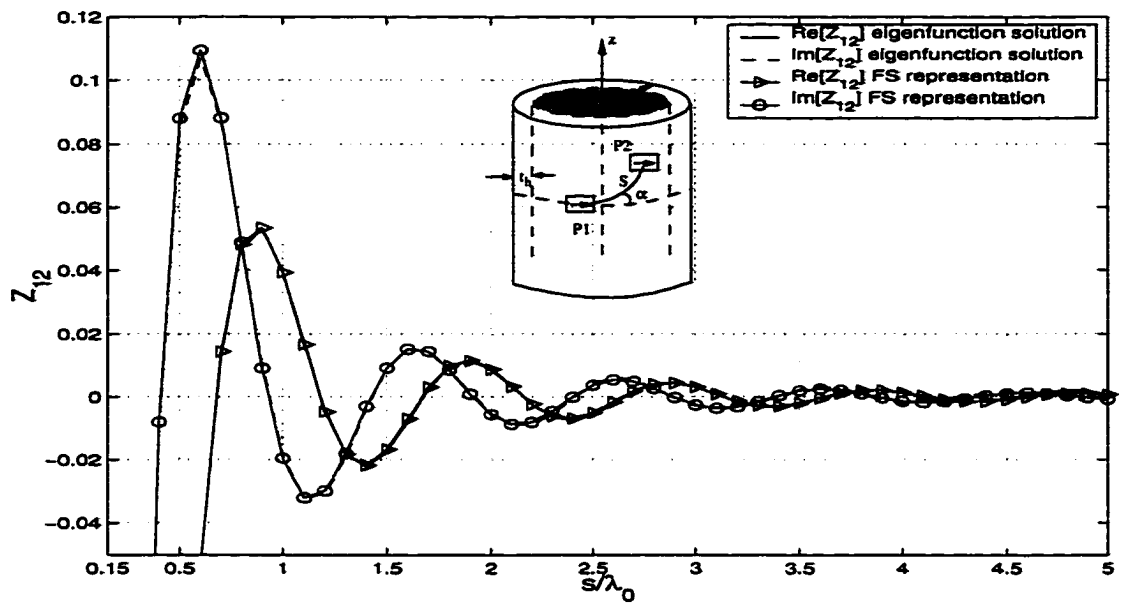


(a) $a = 2.0184\lambda_0, t_h = 0.0216\lambda_0, \epsilon_r = 2.94, \alpha = 85^\circ$

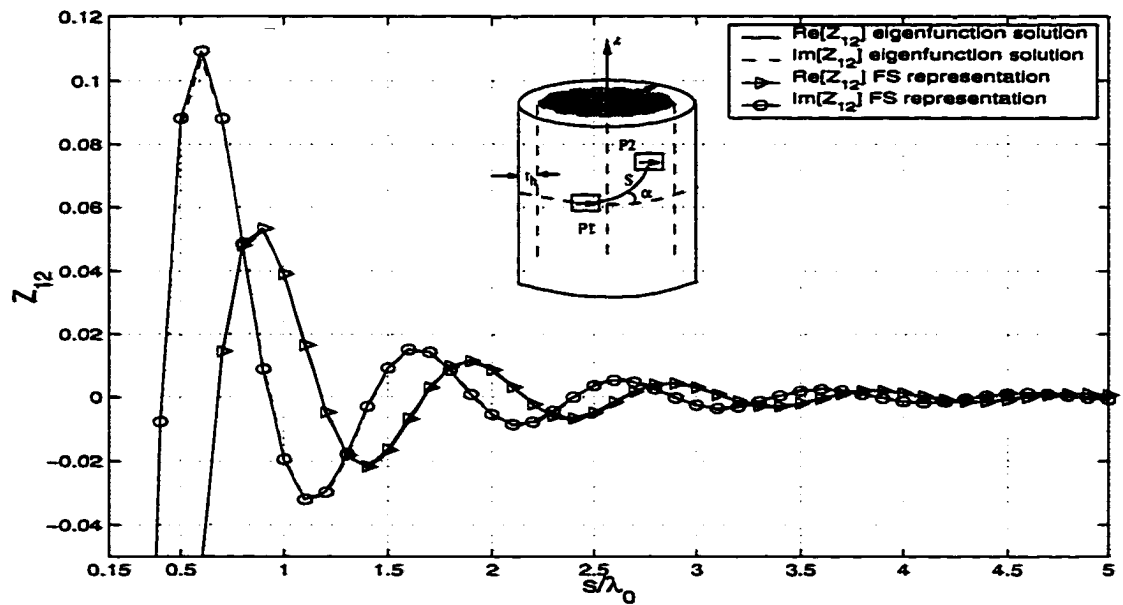


(b) $a = 2.0184\lambda_0, t_h = 0.0216\lambda_0, \epsilon_r = 2.94, \alpha = 70^\circ$

Figure 3.6: Real and imaginary parts of the mutual coupling between ϕ - and z -directed current sources.

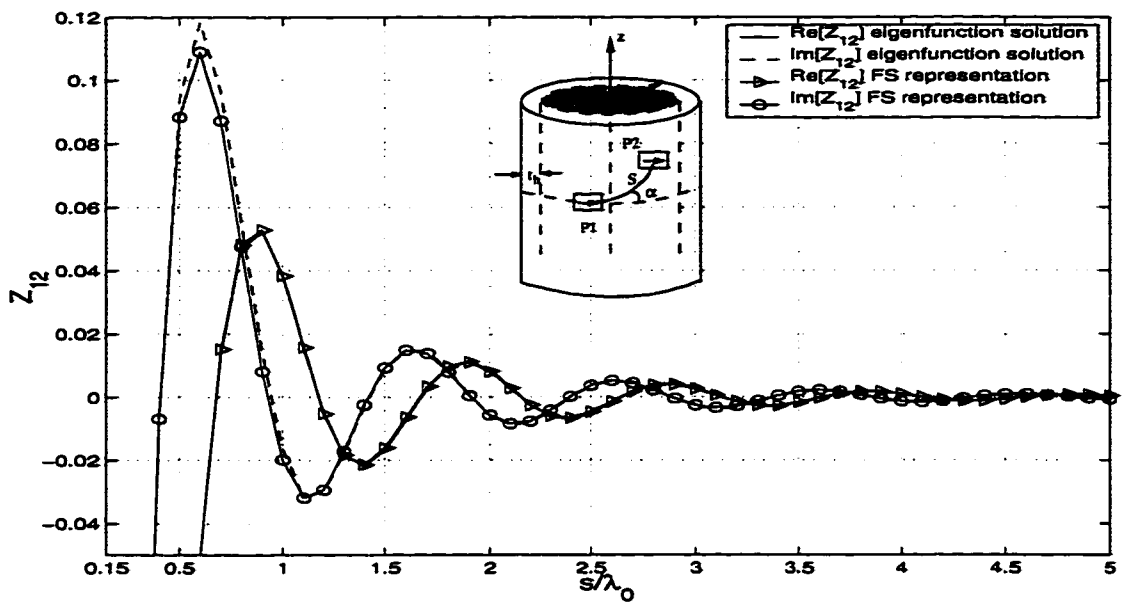


(a) $\alpha = 3\lambda_0$, $t_h = 0.06\lambda_0$, $\epsilon_r = 3.25$, $\alpha = 90^\circ$

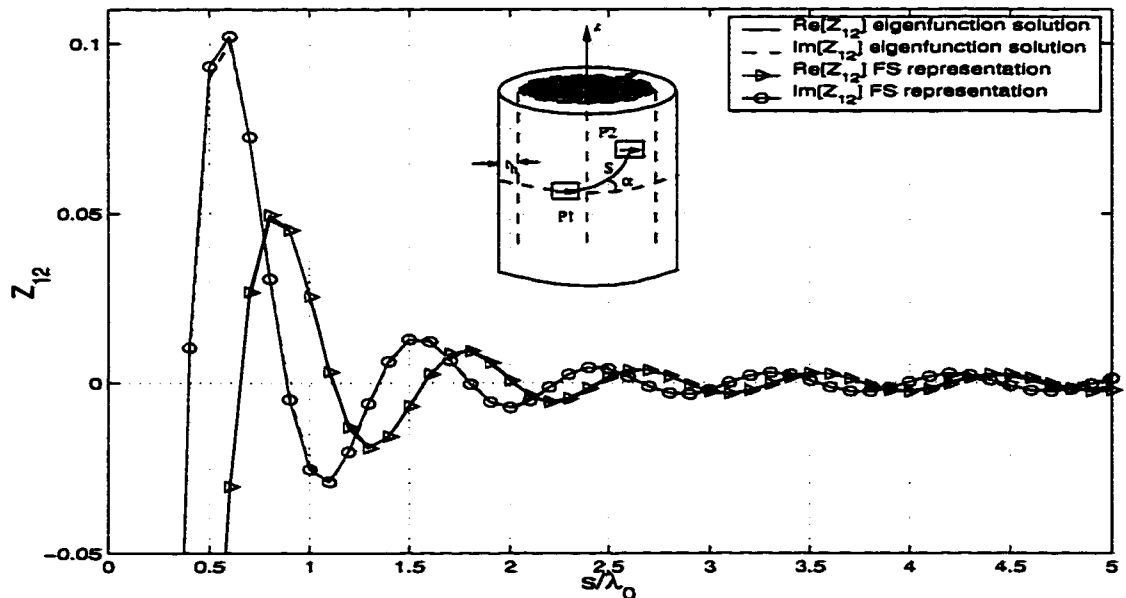


(b) $\alpha = 3\lambda_0$, $t_h = 0.06\lambda_0$, $\epsilon_r = 3.25$, $\alpha = 88^\circ$

Figure 3.7: Real and imaginary parts of the mutual coupling between two ϕ -directed current sources.

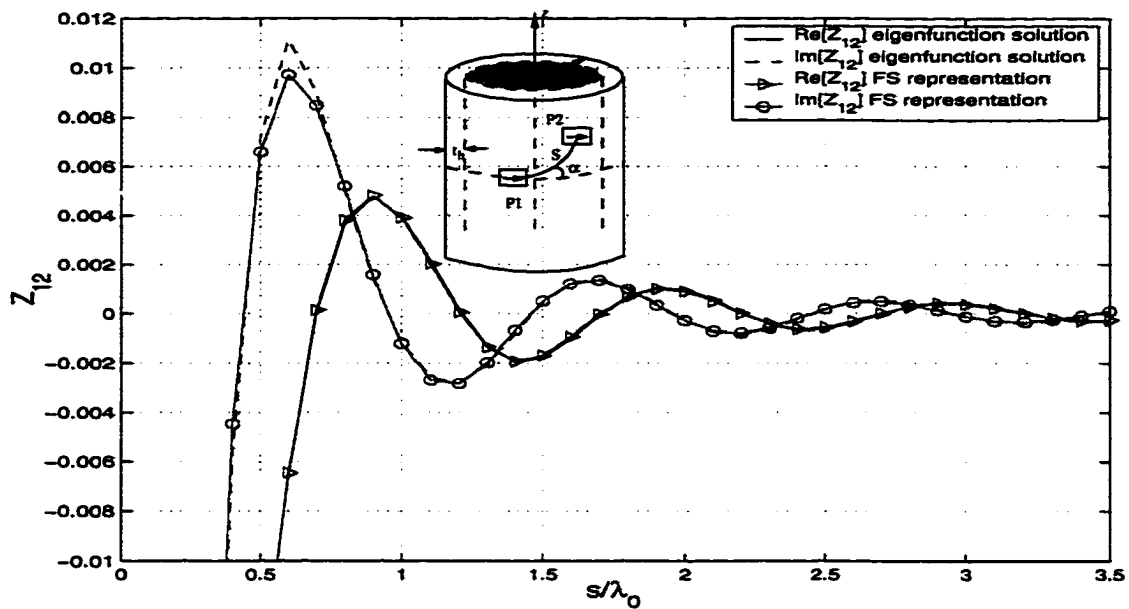


(a) $\alpha = 3\lambda_0, t_h = 0.06\lambda_0, \epsilon_r = 3.25, \alpha = 85^\circ$

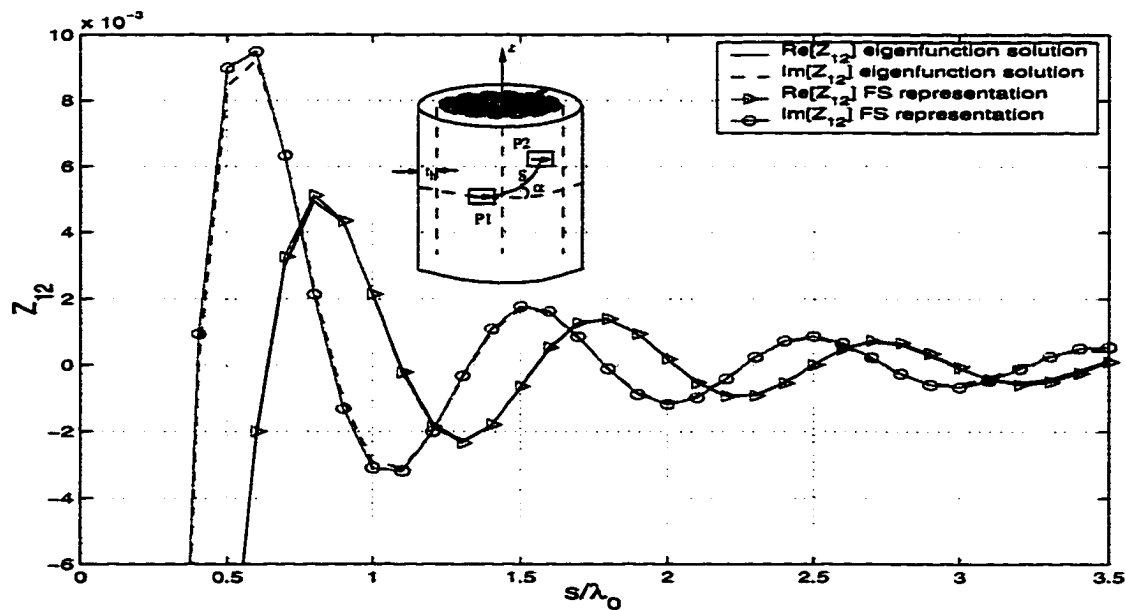


(b) $\alpha = 3\lambda_0, t_h = 0.06\lambda_0, \epsilon_r = 3.25, \alpha = 70^\circ$

Figure 3.8: Real and imaginary parts of the mutual coupling between two ϕ -directed current sources.



(a) $a = 2.0184\lambda_0, t_h = 0.0216\lambda_0, \epsilon_r = 2.94, \alpha = 80^\circ$



(b) $a = 2.0184\lambda_0, t_h = 0.0216\lambda_0, \epsilon_r = 2.94, \alpha = 55^\circ$

Figure 3.9: Real and imaginary parts of the mutual coupling between two ϕ -directed current sources.

chosen as $[-\frac{\pi}{2}, \frac{\pi}{2}]$ and the integral is performed using a 2-point trapezoidal rule, then

$$a_{0_{\phi z}} \approx \frac{1}{\pi} \left[\frac{\pi}{2} \left(\tilde{G}_{\phi z}(\zeta, \psi = -\frac{\pi}{2}) + \tilde{G}_{\phi z}(\zeta, \psi = \frac{\pi}{2}) \right) \right] = \tilde{G}_{\phi z}(\zeta, \psi = \frac{\pi}{2}) \quad (3.43)$$

yielding an approximate expression for $G_{\phi z}^{a2}(\zeta, \psi)$ given by

$$G_{\phi z}^{a2}(\zeta, \psi) \approx \frac{\zeta^2 \sin 2\psi}{2} \tilde{G}_{\phi z}(\zeta, \psi = \pi/2). \quad (3.44)$$

This is the same expression given in [59] and is exact at $\psi = \pi/2$. If one uses (3.44) as the approximate Green's function in (3.4), accurate results are obtained around the region where $\delta \rightarrow \pi/2$ ($\alpha \rightarrow 0$ away from the paraxial region), although the results along the paraxial region are inaccurate, in particular for large s values. Moreover, if the integration interval is chosen as $[0, \pi]$ and integral is performed using a 3-point trapezoidal rule, then

$$a_{0_{\phi z}} \approx \frac{\tilde{G}_{\phi z}(\zeta, \psi = 0) + \tilde{G}_{\phi z}(\zeta, \psi = \frac{\pi}{2})}{2} \quad (3.45)$$

and yields an approximate $G_{\phi z}^{a3}(\zeta, \psi)$ given by

$$G_{\phi z}^{a3}(\zeta, \psi) \approx \frac{\zeta^2 \sin 2\psi}{2} \left[\frac{\tilde{G}_{\phi z}(\zeta, \psi = 0) + \tilde{G}_{\phi z}(\zeta, \psi = \pi/2)}{2} \right] \quad (3.46)$$

and is accurate around $\delta = \pi/4$ ($\alpha = \pi/4$).

Similar modifications are applied to the curvature correction term of the $G_{\phi\phi}(\zeta, \psi)$ component of the dyadic Green's function, namely, if a 3-point trapezoidal rule is used for the evaluation of the Fourier series coefficients, then the final expression for the approximate curvature correction term becomes

$$G_{\phi\phi}^{a2,cc}(\zeta, \psi) \approx G_{\phi\phi}^{cc}(\zeta, \psi = 0) + \left[G_{\phi\phi}^{cc}(\zeta, \psi = \frac{\pi}{2}) - G_{\phi\phi}^{cc}(\zeta, \psi = 0) \right] \left(\frac{1 - \cos 2\psi}{2} \right) \quad (3.47)$$

yielding accurate results in the region ($\delta \rightarrow 90^\circ$ or $\alpha \rightarrow 0$) when combined with (3.23) and used in (3.4). Finally, based on some numerical experimentation (trying different

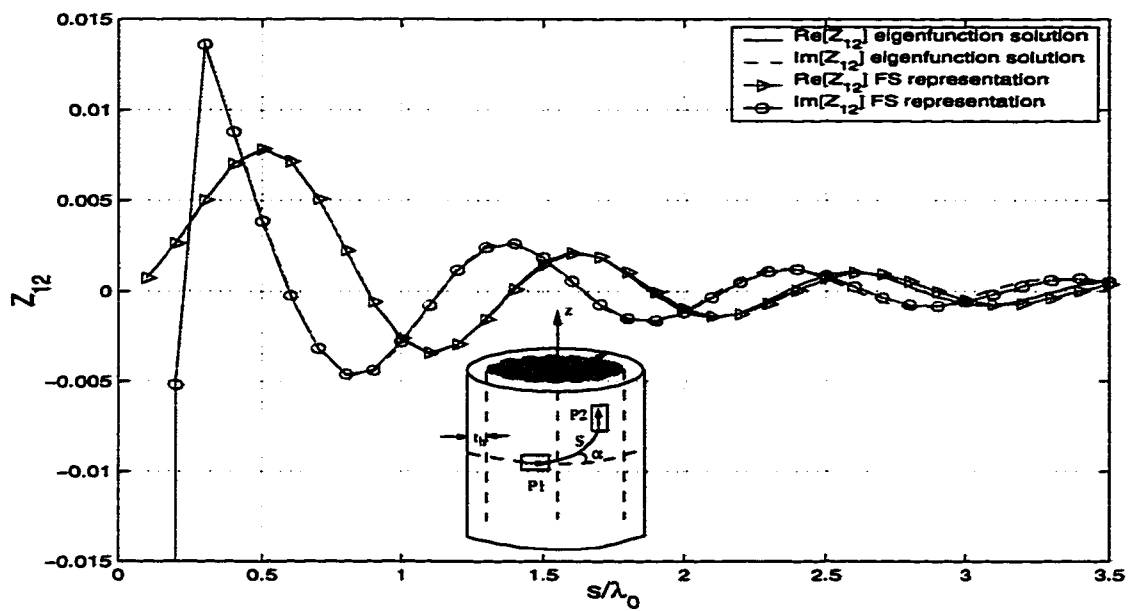
numerical integration routines with a different number of sample points) an extra 2/3 factor for the Fourier series coefficients was obtained yielding an approximate correction term given by

$$G_{\phi\phi}^{a3,cc}(\zeta, \psi) \approx \frac{3}{4} \left\{ G_{\phi\phi}^{cc}(\zeta, \psi = 0) \right. \\ \left. + \left[G_{\phi\phi}^{cc}(\zeta, \psi = \frac{\pi}{2}) - G_{\phi\phi}^{cc}(\zeta, \psi = 0) \right] \left(\frac{1 - \cos 2\psi}{2} \right) \right\}. \quad (3.48)$$

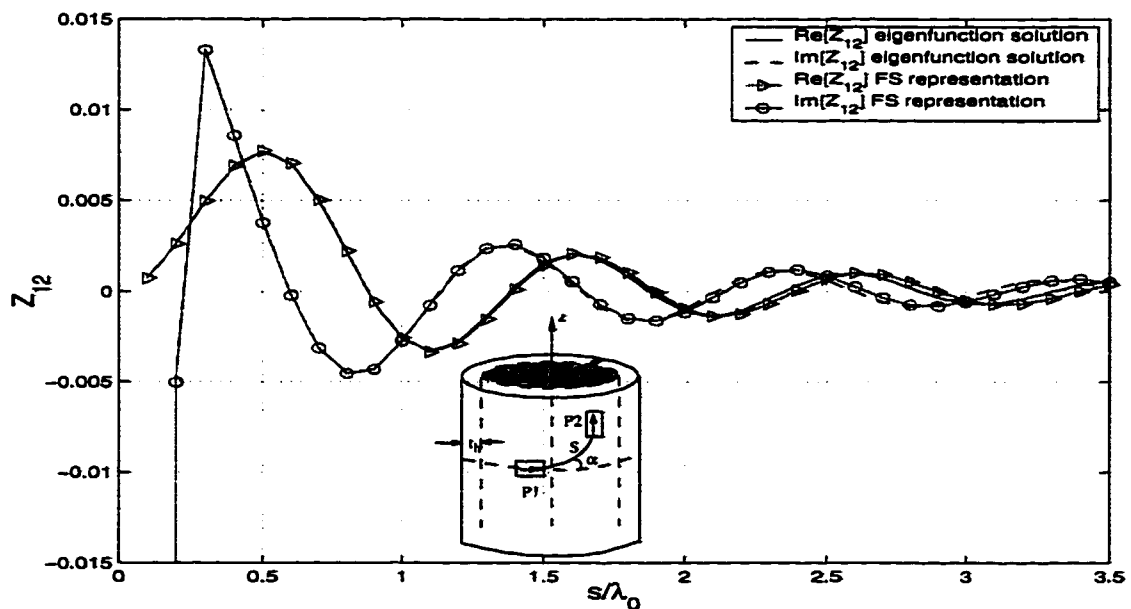
This expression combined with (3.23) and used in (3.4), yields accurate results around $\delta = \alpha = \pi/4$.

The following figures illustrate the accuracy of these new space-domain expressions when the observation point is away from the paraxial region of the source. In Figure 3.10, the coupling between a ϕ - and a z -directed current sources are shown for $\alpha = 45^\circ$ and $\alpha = 40^\circ$, whereas, similar results for the same angles are given for the coupling between two identical ϕ -directed current sources in Figure 3.11 for the cylinder having $\epsilon_r = 2.94$, $a = 2.0184\lambda_0$ and $t_h = 0.0216\lambda_0$. These results justify the accuracy of the approximate Green's function representations given by (3.46) and (3.48), respectively.

Finally, to access the accuracy of (3.44) and (3.47), real and imaginary parts of the mutual coupling between a ϕ - and a z -directed and two identical ϕ -directed current sources are depicted in Figures 3.12 and 3.13, respectively, for a the same cylinder ($\epsilon_r = 2.94, a = 2.0184\lambda_0$ and $t_h = 0.0216\lambda_0$). In Figure 3.12, the α values are 5° and 15° ; whereas, in Figure 3.13, they are 0° and 10° . It should be noted that, the surface field expressions given in this chapter are complementary to the ones given in

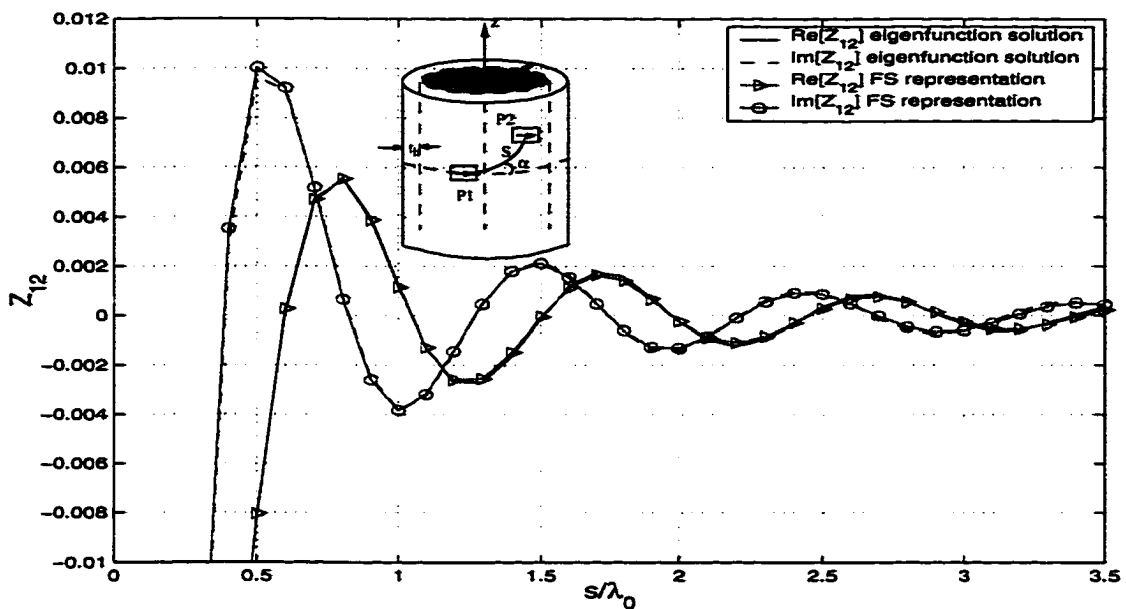


(a) $a = 2.0184\lambda_0, t_h = 0.0216\lambda_0, \epsilon_r = 2.94, \alpha = 45^\circ$

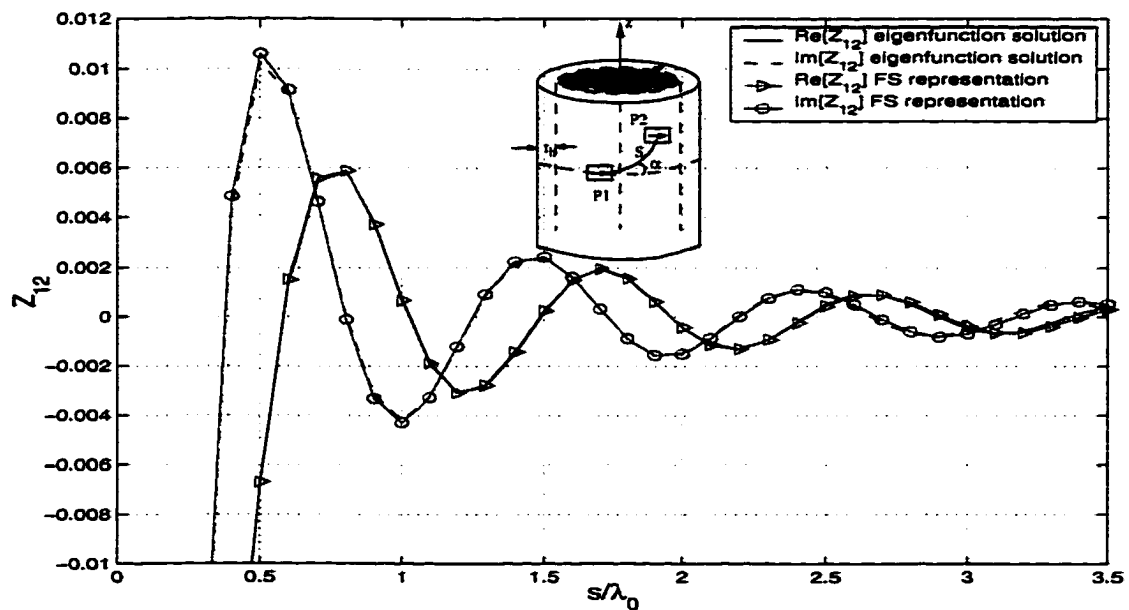


(b) $a = 2.0184\lambda_0, t_h = 0.0216\lambda_0, \epsilon_r = 2.94, \alpha = 40^\circ$

Figure 3.10: Real and imaginary parts of the mutual coupling between ϕ - and z -directed current sources.

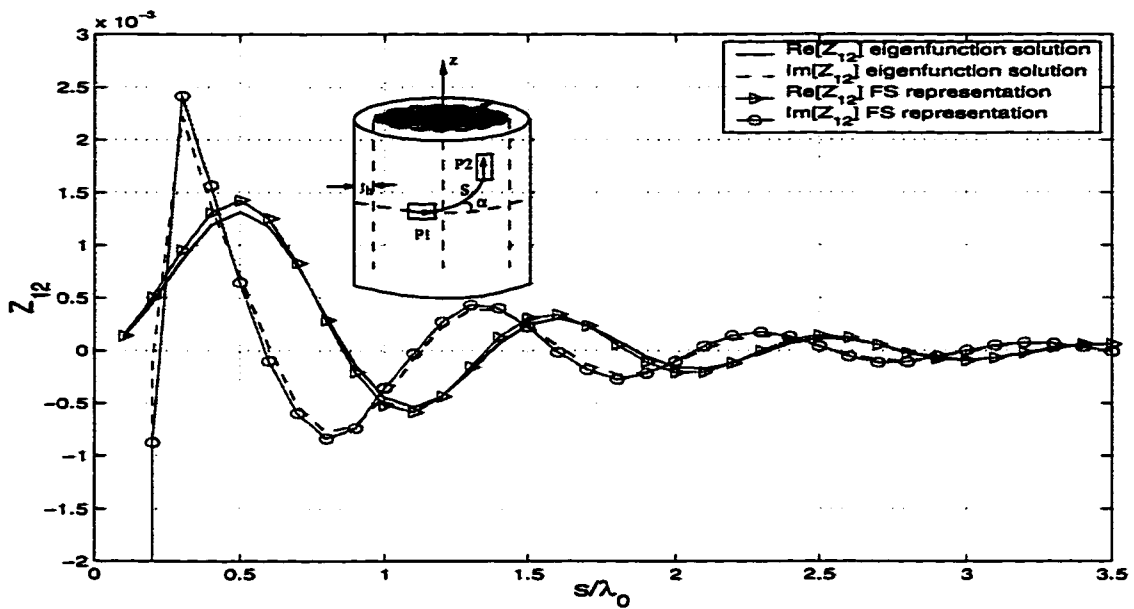


(a) $a = 2.0184\lambda_0, t_h = 0.0216\lambda_0, \epsilon_r = 2.94, \alpha = 45^\circ$

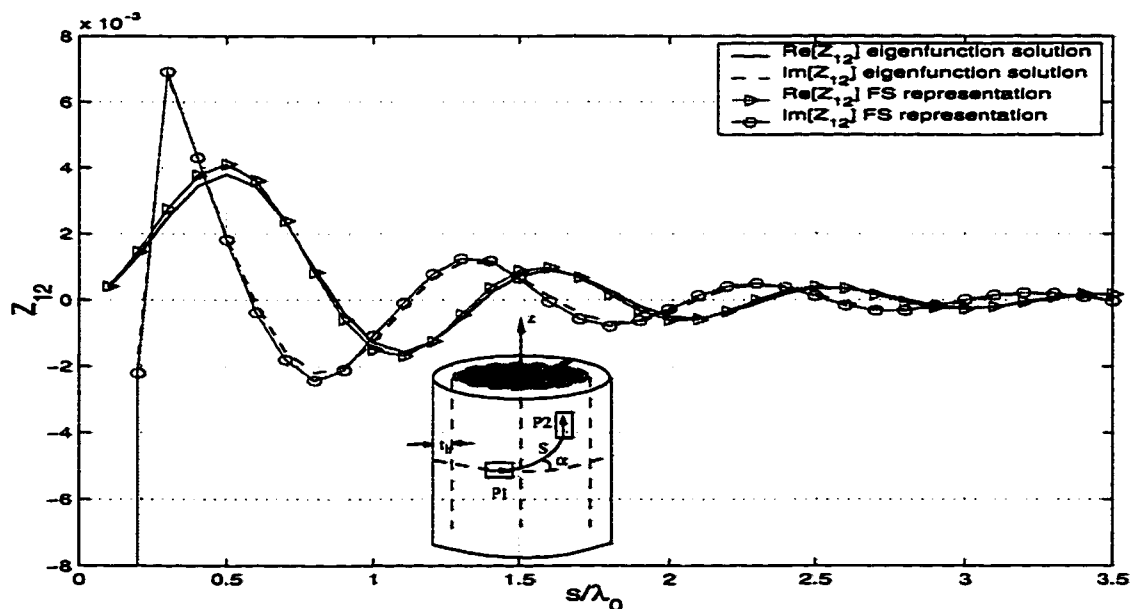


(b) $a = 2.0184\lambda_0, t_h = 0.0216\lambda_0, \epsilon_r = 2.94, \alpha = 40^\circ$

Figure 3.11: Real and imaginary parts of the mutual coupling between two ϕ -directed current sources.

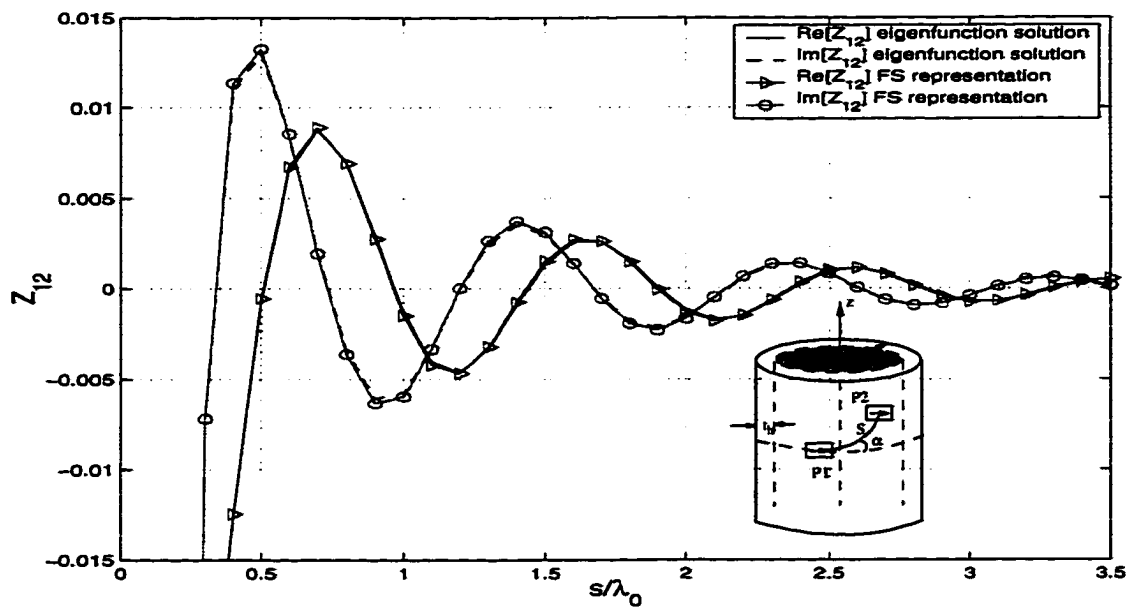


(a) $a = 2.0184\lambda_0, t_h = 0.0216\lambda_0, \epsilon_r = 2.94, \alpha = 5^\circ$

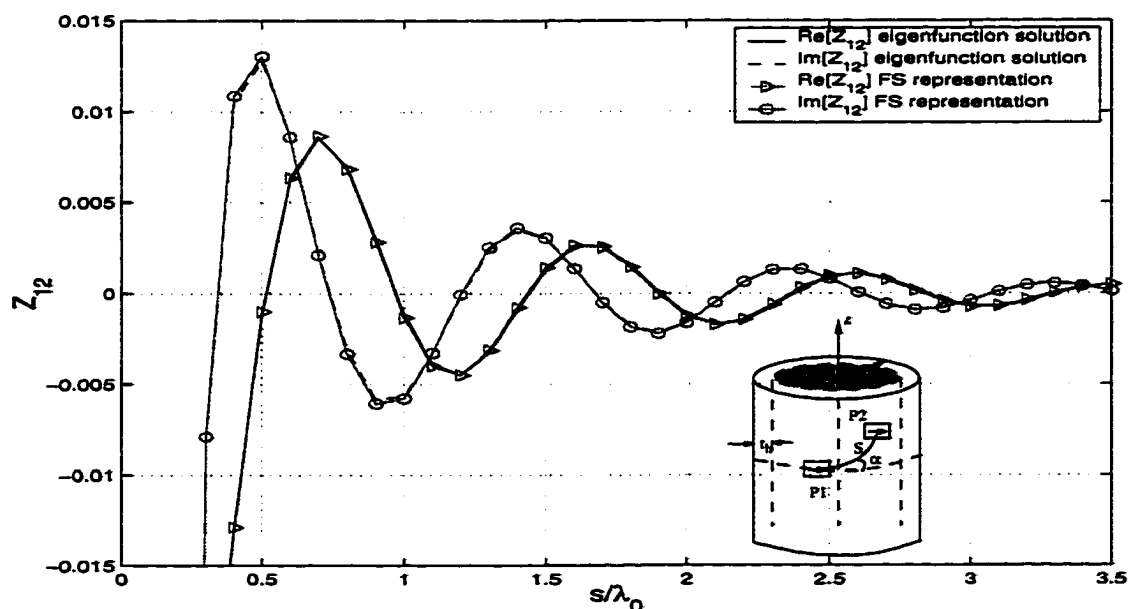


(b) $a = 2.0184\lambda_0, t_h = 0.0216\lambda_0, \epsilon_r = 2.94, \alpha = 15^\circ$

Figure 3.12: Real and imaginary parts of the mutual coupling between ϕ - and z -directed current sources.



(a) $a = 2.0184\lambda_0$, $t_h = 0.0216\lambda_0$, $\epsilon_r = 2.94$, $\alpha = 0^\circ$



(b) $a = 2.0184\lambda_0$, $t_h = 0.0216\lambda_0$, $\epsilon_r = 2.94$, $\alpha = 10^\circ$

Figure 3.13: Real and imaginary parts of the mutual coupling between two ϕ -directed current sources.

the previous chapter. Furthermore, the region where these representations produce accurate results overlap and hence, one can safely switch from one representation to the other in a MoM based solution.

CHAPTER 4

The MoM/Green's Function Solution

4.1 Introduction

In this chapter, the results derived in the previous chapters are used to formulate MoM based solutions for microstrip antennas and array elements conformal to material coated electrically large cylinders. This method is also referred to as a hybrid MoM/Green's function method [2]. Briefly, an exact integral equation for the unknown equivalent currents representing only the microstrip patches on the top of the substrate is formulated. The kernel of this integral equation is the special Green's function, developed in the previous chapters (which satisfies the boundary conditions of a dielectric coated PEC circular cylinder). Since the solutions presented here are valid for electrically large cylinders ($d > 1\lambda_0$), the Green's function for the cylinder is approximated by the Green's function of a cylinder with an infinite radius (planar approximations) [7] when the distance between the source and observation points is less than $0.2\lambda_0$ (or basically, for the self and neighboring terms). The unknown equivalent currents are then solved using the MoM procedure. Namely, they are expanded as a finite sum of N basis functions, and N weighted averages (Galerkin's method) of the integral equation are enforced on the microstrip patches, transforming the integral

equation into a matrix equation whose order is N . Finally, the matrix equation is solved for the N coefficients in the expansion for the current on the metallic portions. In Section 4.2, an integral equation is developed and the MoM solution for this problem is briefly explained in Section 4.3. To validate the proposed method, numerical results involving the input impedance of a microstrip antenna, as well as mutual coupling between two microstrip antennas conformal to an electrically large circular cylinder are presented and compared with the available results in the literature in Section 4.4.

4.2 Development of Integral Equation

Figure 4.1(a) shows a microstrip antenna element mounted on a dielectric coated PEC circular cylinder. The antenna is fed via a probe. Using Schelkunoff's surface equivalence principle [73], an equivalent problem can be obtained as depicted in Figure 4.1(b), where the conducting patch is replaced with the equivalent induced currents which are unknown and are to be solved via MoM.

One starts with

$$\vec{E}(\vec{r}) = \vec{E}^i(\vec{r}) + \vec{E}^s(\vec{r}) \quad (4.1)$$

where $\vec{E}^i(\vec{r})$ is the field generated by a known probe current density $\vec{J}^i(\vec{r}')$ in the presence of a dielectric coated PEC circular cylinder and is given by

$$\vec{E}^i(\vec{r}) = \iint_{S_{source}} \overline{\overline{G}}(\vec{r}/\vec{r}') \cdot \vec{J}^i(\vec{r}') ds'. \quad (4.2)$$

Similarly, $\vec{E}^s(\vec{r})$ is the scattered field and is given by

$$\vec{E}^s(\vec{r}) = \iint_{S_{patch}} \overline{\overline{G}}(\vec{r}/\vec{r}') \cdot \vec{J}^s(\vec{r}') ds'. \quad (4.3)$$

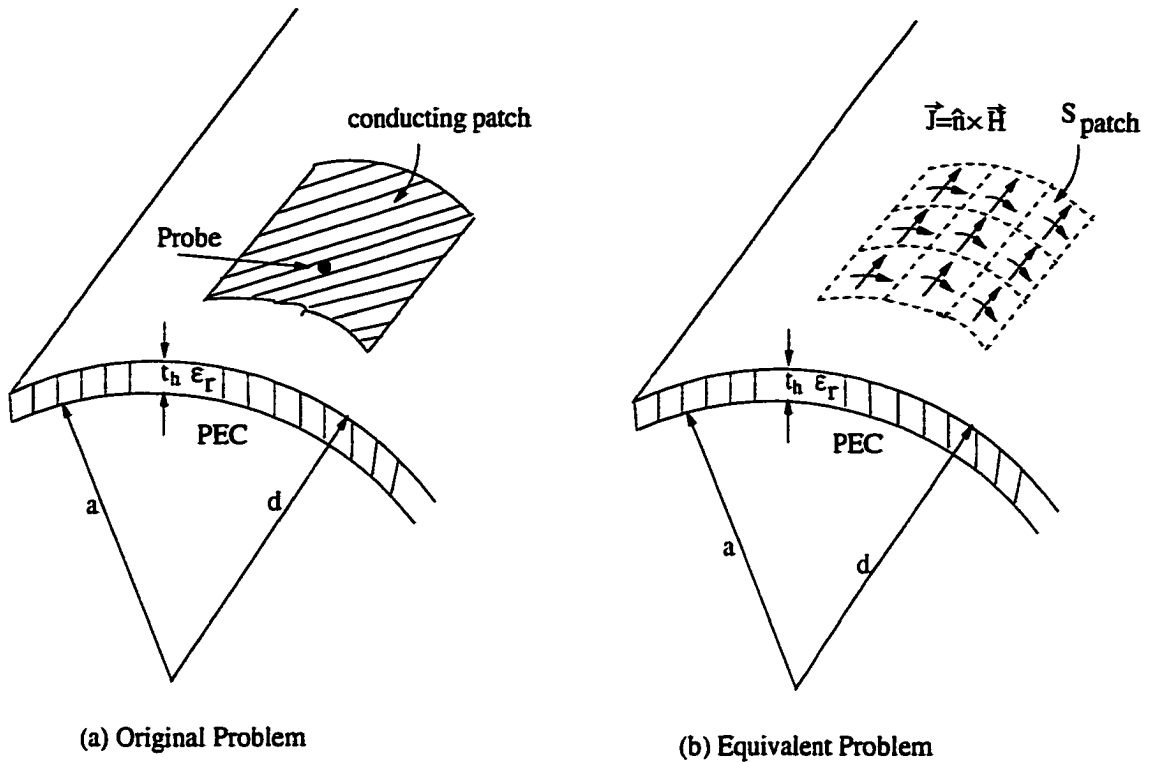


Figure 4.1: Equivalence Principle

where $\vec{J}^s(\vec{r}')$ is the unknown induced current to be determined. The electric field integral equation (EFIE) is a statement of the boundary condition that the total electric field (4.1) tangential to the surface covered by the metallic microstrip patch should vanish such that

$$\hat{n} \times \vec{E}(\vec{r}) = \hat{n} \times [\vec{E}^i(\vec{r}) + \vec{E}^s(\vec{r})] = 0 \quad \text{on } S_{patch} \quad (4.4)$$

Then,

$$\iint_{S_{patch}} \hat{n} \times \bar{\bar{G}}(\vec{r}/\vec{r}') \cdot \vec{J}^s(\vec{r}') d\vec{s}' = - \iint_{S_{source}} \hat{n} \times \bar{\bar{G}}(\vec{r}/\vec{r}') \cdot \vec{J}^i(\vec{r}') d\vec{s}' . \quad (4.5)$$

This is the EFIE to be solved via the MoM for the unknown currents $\vec{J}^s(\vec{r}')$. The appropriate Green's function is denoted by $\bar{\bar{G}}(\vec{r}/\vec{r}')$, where the primed coordinates

represent the source and the unprimed coordinates represent the observation point. The unit normal to the surface is denoted by \hat{n} which is \hat{p} for this problem.

At this point, it should be noted that the EFIE seems to be a natural choice for the microstrip antenna problems among the other integral equations. The magnetic field integral equation (MFIE), which is a statement of the surface equivalent theorem, can not be used for an open surface (as in the case of microstrip antenna problems) and hence, the combined field integral equation (CFIE) which is a linear combination of EFIE and MFIE can not be used as well. However, for implementation purposes, it is sometimes convenient to convert the EFIE into the form of a mixed-potential integral equation (MPIE) [74], [75] where the scattered field $\vec{E}^s(\vec{r})$ can be derived from a scalar potential V and a vector potential \vec{A} as

$$\vec{E}^s(\vec{r}) = -j\omega \vec{A}(\vec{r}) - \nabla V(\vec{r}) \quad (4.6)$$

where

$$V(\vec{r}) = \iint_S G_V(\vec{r}/\vec{r}') q_s(\vec{r}') ds' \quad (4.7)$$

and

$$\vec{A}(\vec{r}) = \iint_S \bar{\bar{G}}_A(\vec{r}/\vec{r}') \cdot \vec{J}^s(\vec{r}') ds' \quad (4.8)$$

with $S = S_{patch}$, q_s and \vec{J}^s are the charge and current densities, respectively. Substituting (4.7) and (4.8) into (4.6) and substituting the resultant equation into (4.4), the MPIE can be written as

$$\hat{n} \times \left[j\omega \iint_S \bar{\bar{G}}_A(\vec{r}/\vec{r}') \cdot \vec{J}^s(\vec{r}') ds' + \nabla \iint_S G_V(\vec{r}/\vec{r}') q_s(\vec{r}') ds' \right] = \hat{n} \times \vec{E}^i(\vec{r}) \quad (4.9)$$

where charge and current densities are related through the continuity equation, namely,

$$\nabla \cdot \vec{J}_s + j\omega q_s = 0 . \quad - \quad (4.10)$$

As seen from (4.9), the MPIE involves both the vector and scalar potentials; the former expressed in terms of the induced currents, and the latter in terms of the induced charge. Although the MPIE formulation requires more effort to set up the corresponding integral equation, it may be preferable to the EFIE because it requires only the potential forms of the Green's functions which are less singular than their derivatives needed in the EFIE. Moreover, the convergence of potential forms of the Green's functions are better than the field forms, in particular for layered medium due to the fact that the Green's functions in layered media comprise Sommerfeld-type integrals, which are difficult to evaluate [76].

In this dissertation the standard EFIE is used throughout. However, the EFIE exhibits an internal resonance problem for closed bodies which yields a high condition number [77]. The same problem appears even if one uses the MPIE. This may create problems during the matrix inversions.

4.3 Moment Method Solution

The conventional MoM procedure starts with expansion of $\vec{J}^s(\vec{r})$ in terms of a finite set of subsectional basis functions:

$$\vec{J}^s(\vec{r}) = \sum_{n=1}^N a_n \vec{J}_n(\vec{r}) \quad (4.11)$$

where

$$\vec{J}(\vec{r}) = \begin{cases} f_p(\vec{r}) \hat{z}, & p = 1, \dots, P \text{ on the patch} \\ g_k(\vec{r}) \hat{\phi}, & k = 1, \dots, K \text{ on the patch} \end{cases} \quad (4.12)$$

with $N = P+K$, a_n being the unknowns to be solved, and

$$\vec{J}_n(\vec{r}) \neq 0 \text{ only if } \vec{r} \in S_n; \quad \bigcup_{n=1}^N S_n = S_{patch}. \quad (4.13)$$

Substituting (4.12) and (4.11) into (4.5), one obtains a single vector equation with N unknowns. Using a set of weighting functions (testing functions) denoted by $\vec{w}_m(\vec{r})$ ($m = 1, \dots, N$), we test the resulting equation to obtain the matrix equation,

$$[Z] I = V \quad (4.14)$$

where

$$Z_{mn} = \iint_{S_m} ds_m \vec{w}_m(\vec{r}_m) \cdot \left(\iint_{S_n} ds_n \bar{\bar{G}}(\vec{r}_m/\vec{r}_n) \cdot \vec{J}_n(\vec{r}_n) \right) \quad (4.15)$$

$$I_n = a_n \quad (4.16)$$

$$V_m = - \iint_{S_m} ds_m \vec{w}(\vec{r}_m) \cdot \vec{E}^i(\vec{r}_m) \quad (4.17)$$

where $m, n = 1, \dots, N$

This matrix equation can be solved using direct solution methods such as Gaussian elimination or LU-decomposition or iterative schemes like conjugate gradient method. Once the matrix equation is solved, the induced current can be reconstructed via (4.11).

The weighting functions are chosen to be identical to the expansion basis functions and this testing method is called Galerkin's method. In the literature it is shown that the Galerkin's testing method is a variational method [1], which implies that good accuracy and quick convergence may be expected.

The rate of convergence of the MoM procedure can significantly be increased by choosing basis functions whose properties coincide with the properties of the actual solution. In other words, less number of basis functions will be sufficient to approximate the actual solution. Besides, the accuracy of the desired solution, the ease

of evaluating the matrix elements, the size of the matrix and resulting conditioned numbers of the MoM matrix [\mathbf{Z}] are important aspects to be considered in choosing the expansion and weighting basis functions. Therefore, subsectional basis functions such as piecewise sinusoids (PWS) and/or entire domain basis (EB) functions can be chosen based on the application. In this dissertation, each current mode is defined by a piecewise sinusoid along the direction of the current and constant in the orthogonal direction to the current as depicted in Figure 2.17 and described in (2.88). The reason behind such a choice is that subsectional basis functions are better suited to model arbitrary geometries in the MoM procedure.

4.4 Numerical Results

Numerical results for the surface fields on a dielectric coated circular cylinder have already been presented in Chapters 2 and 3 where SDP and paraxial representations of the special Green's function are compared with the traditional eigenfunction solution for different size of cylinders with different coating properties. In all the aforementioned numerical results, the variation of the surface fields with the distance between the source and observation points are illustrated. In this section, the first set of numerical results will illustrate the mutual coupling as a function of α for fixed separations between the source and observation points. In Figure 4.2, the mutual coupling between two identical z -directed current modes are calculated where the SDP and the paraxial representations are combined and the result is compared with the eigenfunction solution for a cylinder with $a = 3\lambda_0$, $t_h = 0.06\lambda_0$, $\epsilon_r = 3.25$. As seen from the figure, the SDP and the paraxial representations complement each other and yields good agreement with the eigenfunction solution. A similar result is illustrated

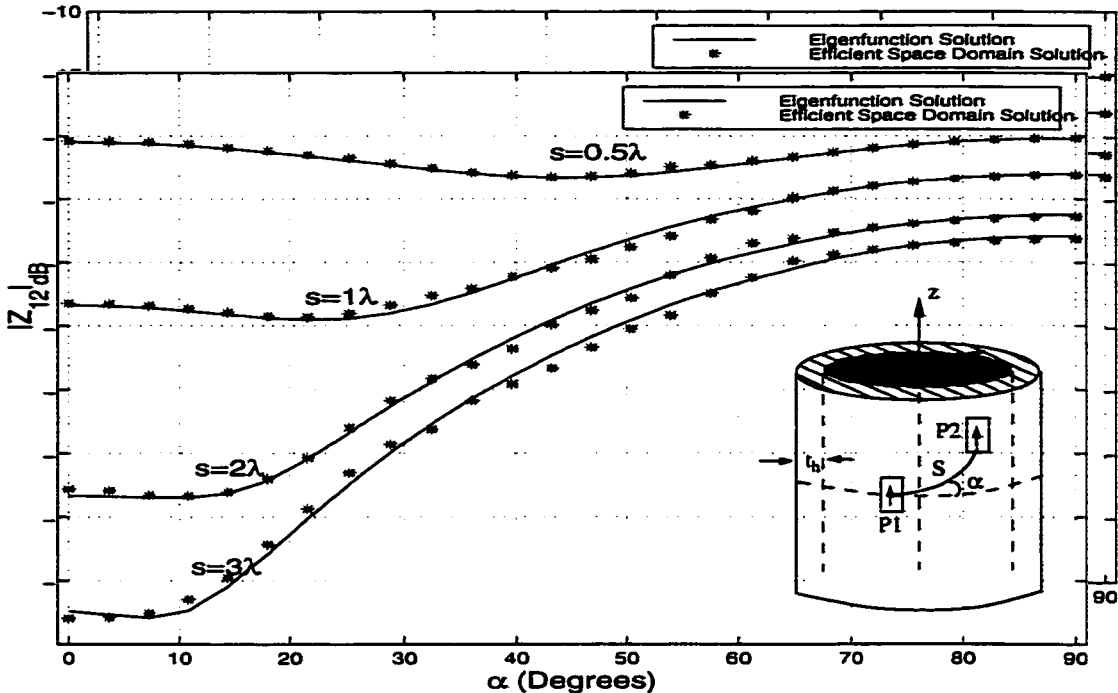


Figure 4.2: Mutual coupling (Z_{12}) between two identical z -directed current modes for a coated cylinder with $a = 3\lambda_0$, $t_h = 0.06\lambda_0$, $\epsilon_r = 3.25$.

in Figure 4.3 for the mutual coupling between ϕ - and z -directed current modes for the same cylinder. The reason the zero coupling occurs is that at $\alpha = 0, \pi/2$ the cross-polar component of the surface field exhibits a $\sin 2\alpha$ type pattern which is similar to the planar case as shown in [78]. The mutual coupling between two ϕ -directed current modes are calculated and compared with the eigenfunction solution in Figure 4.4 for the same cylinder. Finally, to show the limitation of the SDP and paraxial representations, the mutual coupling between two z -directed and two ϕ -directed current modes are calculated in Figures 4.5 and 4.6, respectively, using the SDP and paraxial representations in the entire angular domain ($0 \leq \alpha \leq 90^\circ$). The angle α is varied for a fixed separation $s = 3\lambda$. As seen from the figures, the

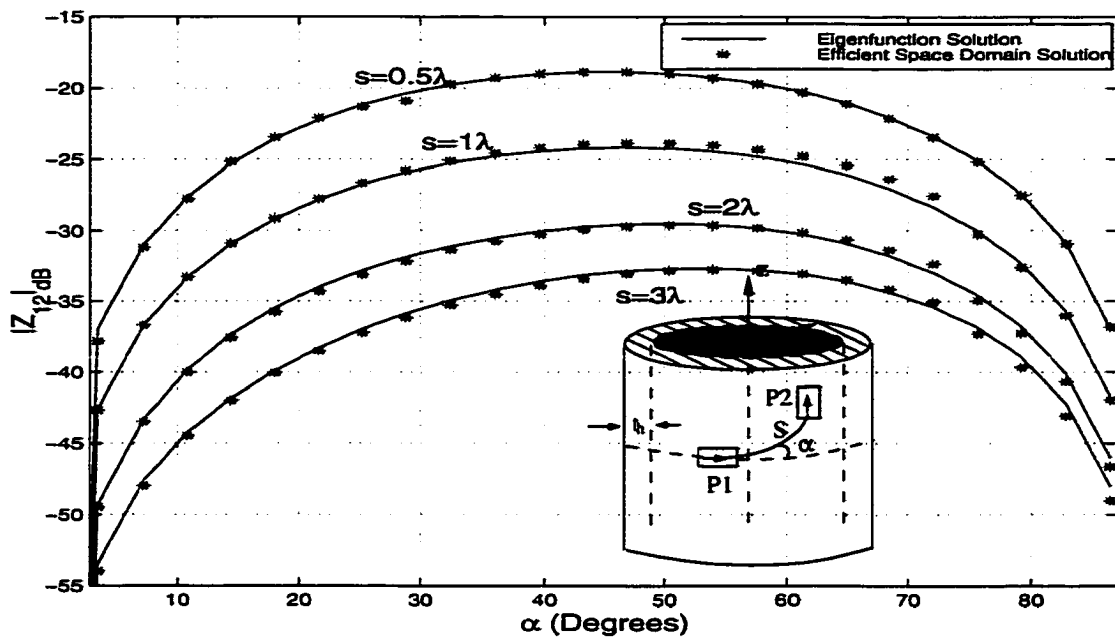


Figure 4.3: Mutual coupling (Z_{12}) between ϕ and z -directed current modes for a coated cylinder with $a = 3\lambda_0$, $t_h = 0.06\lambda_0$, $\epsilon_r = 3.25$.

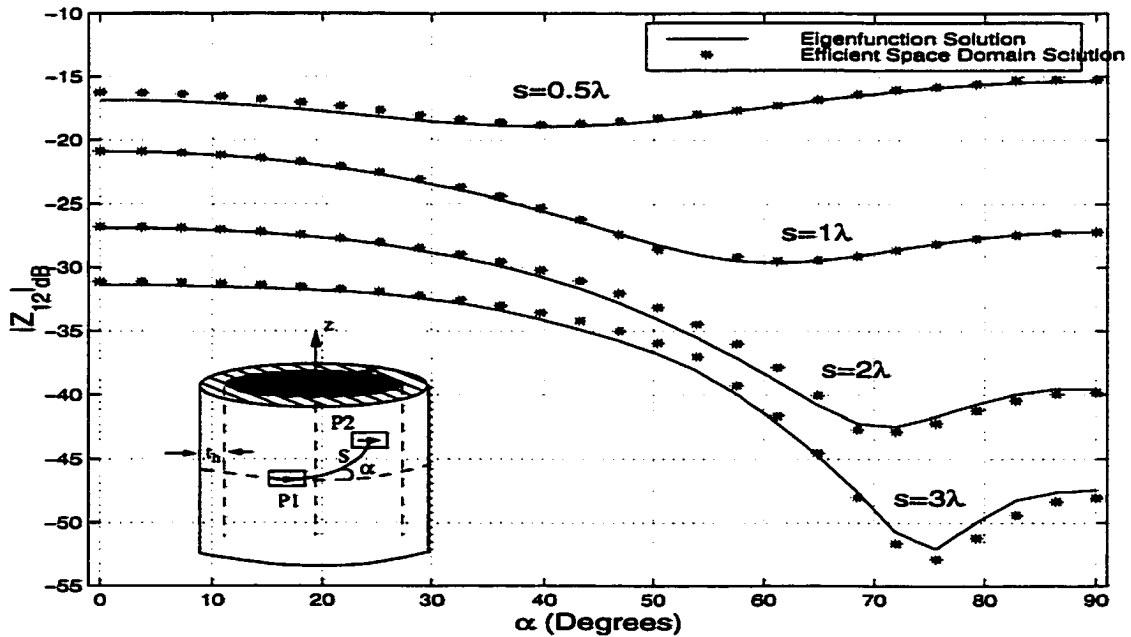


Figure 4.4: Mutual coupling (Z_{12}) between two ϕ -directed current modes for a coated cylinder with $a = 3\lambda_0$, $t_h = 0.06\lambda_0$, $\epsilon_r = 3.25$.

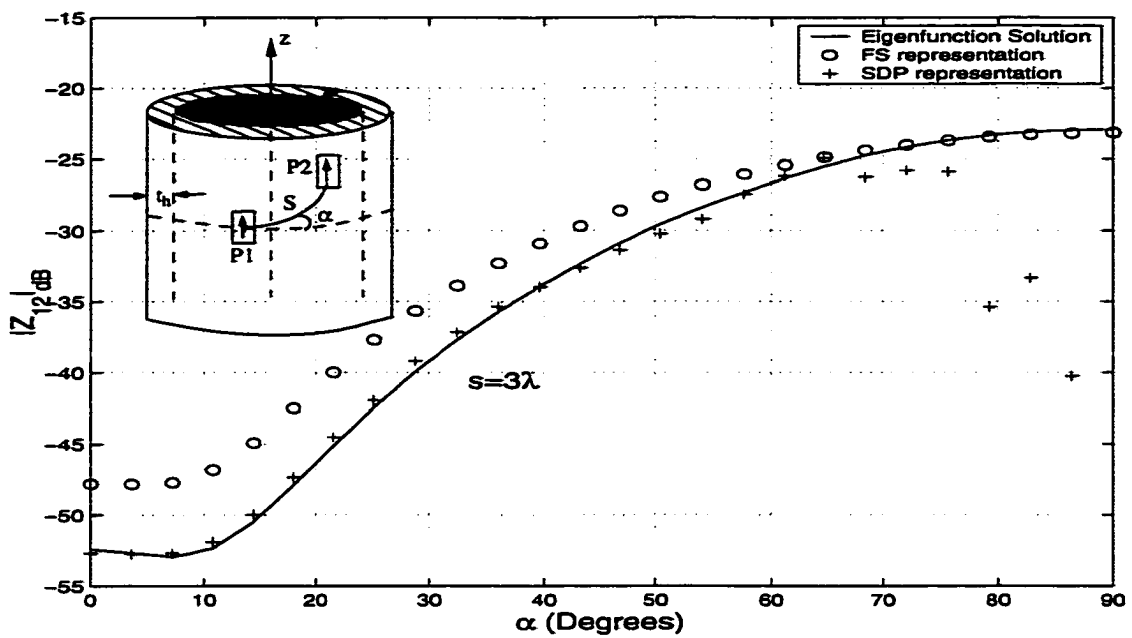


Figure 4.5: Mutual coupling (Z_{12}) between two identical z -directed current modes for a coated cylinder with $a = 3\lambda_0$, $t_h = 0.06\lambda_0$, $\epsilon_r = 3.25$.

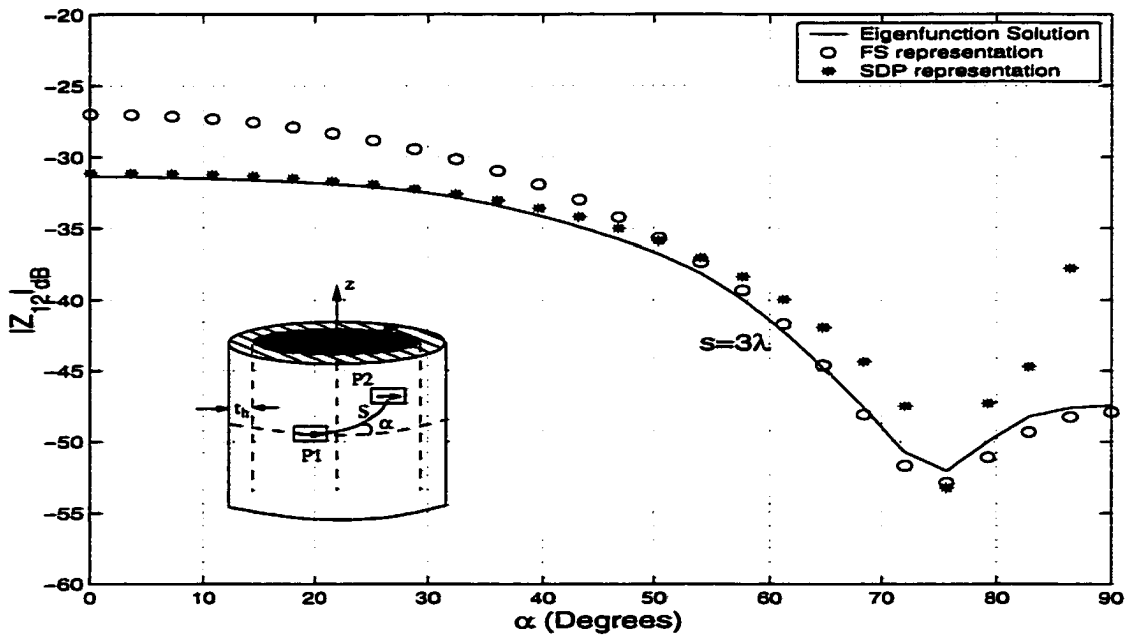


Figure 4.6: Mutual coupling (Z_{12}) between two identical ϕ -directed current modes for a coated cylinder with $a = 3\lambda_0$, $t_h = 0.06\lambda_0$, $\epsilon_r = 3.25$.

SDP representation loses its accuracy as the angle α approaches to 90° ; whereas, the paraxial representation is not very accurate for small α values.

The next set of numerical results that will be presented are MoM-based results where more useful quantities, such as input impedance of a microstrip antenna and the mutual coupling between two identical microstrip patches on a coated large circular cylinder are calculated.

Figure 4.7(a) shows the geometry of a probe-fed rectangular microstrip antenna whereas Figure 4.7(b) illustrates the geometry of two probe-fed rectangular microstrip antennas on the outer surface of a cylindrically shaped dielectric substrate with the thickness t_h and relative permittivity $\epsilon_r > 1$. The substrate is backed by a perfectly conducting, cylindrically shaped ground plane. Both the ground plane and cylinder are assumed to be infinite in the z -direction. Let's first consider the two antenna configuration (4.7(b)). The antennas are fed at the feed locations (z_{f_i}, r_{f_i}) where $i = 1$ is the first port and $i = 2$ is the second one. Based on the two-port configuration of Figure 4.7(c), we can write

$$V_1 = Z_{11}^p I_1 + Z_{12}^p I_2 \quad (4.18)$$

$$V_2 = Z_{21}^p I_1 + Z_{22}^p I_2 \quad (4.19)$$

where

$$Z_{11}^p = \frac{V_1}{I_1} \Big|_{I_2=0} \quad (4.20)$$

$$Z_{22}^p = \frac{V_2}{I_2} \Big|_{I_1=0} \quad (4.21)$$

and

$$Z_{12}^p = \frac{V_1}{I_2} \Big|_{I_1=0} \quad (4.22)$$

$$Z_{21}^p = \frac{V_2}{I_1} \Big|_{I_2=0} \quad (4.23)$$

Z_{11}^p is the input impedance of element one with element two open-circuited (the superscript p stands for port), and can be written as [79]

$$Z_{11}^p = \frac{-\int_v \vec{E}^{(1)} \cdot \vec{J}_i^{(1)} dv}{(I_i)^2} \quad (4.24)$$

where $\vec{E}^{(1)}$ is the total electric field from the N expansion modes induced by the impressed source current $\vec{J}_i^{(1)}$ at port one, and I_i is the terminal current of the source (1 Amp in this case). The use of (4.17) then gives

$$Z_{11}^p = - \sum_{n=1}^N I_n V_n^{(1)} \quad (4.25)$$

where I_n are the expansion mode currents found from (4.14) and $V_n^{(1)}$ are the voltages due to the currents J_n . A similar expression can be used to calculate Z_{22}^p .

The mutual impedance between ports one and two, namely, Z_{21}^p can be written as [79]

$$Z_{21}^p = \frac{-\int_v \vec{E}^{(2)} \cdot \vec{J}_i^{(1)} dv}{(I_i)^2} \quad (4.26)$$

where $\vec{E}^{(2)}$ is the total electric field induced by the current $\vec{J}_i^{(2)}$ at port two with port one open. Using (4.17) yields

$$Z_{21}^p = - \sum_{n=1}^N I_n V_n^{(2)} \quad (4.27)$$

where $V_n^{(2)}$ are the voltages due to the currents J_n . It should be kept in mind that $Z_{21}^p = Z_{12}^p$ as a result of the reciprocity theorem. The input impedance for the single antenna depicted in Figure 4.7(a) can be calculated using (4.25) where the second antenna has been removed.

The first numerical example is given for a single rectangular microstrip patch mounted on a dielectric coated circular cylinder with $a = 20 \text{ cm}$, $\epsilon_r = 2.32$, $t_h = 0.795 \text{ mm}$. The patch is excited with a TM_{01} mode and has the following dimensions: $L = 3 \text{ cm}$, $W = 4 \text{ cm}$. Figure 4.8 shows the input impedance (real and imaginary part) of this cylindrical-rectangular antenna versus frequency where the MoM result is compared with the result given in [80] which is obtained using the GTLM method. To compare the MoM solution with the result given in [80], the antenna is fed via a probe at the feed location $(z_f, r l_f) = (0.5\text{cm}, 2\text{cm})$ as seen in Figure 4.8. The overall agreement is good except for a small frequency shift (less than 1%). The same antenna is fed at $(z_f, r l_f) = (0.95\text{cm}, 2\text{cm})$ so that a 50Ω input impedance is obtained at the resonance frequency $f = 3185 \text{ MHz}$ as depicted in Figure 4.9. In both results the basis functions are selected to be piecewise sinusoidal along the direction of the current and constant in the direction perpendicular to the current. Each element has a dimension of $0.1\lambda_0$ by $0.1\lambda_0$ at the highest frequency simulated. As a result, the number of basis functions N is 31 for this example (15 basis functions along the z -direction ($P = 15$) and 16 basis functions along the ϕ -direction (K)).

Finally, two identical antennas are mounted on the same cylinder and the calculated E-plane and H-plane mutual coupling coefficients versus the edge to edge spacing S between them are presented in Figures 4.10 and 4.11, respectively. In Figures 4.10 and 4.11, the edge to edge spacing is normalized with respect to the

free-space wavelength λ_0 . The operating frequency is $3185MHz$ where the TM_{01} mode is excited. Note that the mutual coupling coefficient can be calculated from [81]

$$s_{12} = \frac{2Z_{12}Z_0}{(Z_{11} + Z_0)(Z_{22} + Z_0) - Z_{12}Z_{21}} \quad (4.28)$$

where Z_0 is the characteristic impedance of the feeding coaxial cable (assumed to be 50Ω here). As in the case of a single patch, 31 basis functions are used for each antenna, yielding an impedance matrix having $N = 62$ basis functions.

Another way to access the accuracy of the MoM solutions is to perform a convergence test. Thus, a convergence test is performed for a single frequency $f = 3175MHz$ for the example of Figure 4.8. Based on this test, if the size of basis functions along the ϕ -direction decreases (keeping the size of the z -directed basis functions constant), convergence is achieved after $N = 31$ as illustrated in Figure 4.12. However, if the size of basis functions along the z -direction decreases, the input impedance first converges around $N = 31$, but then diverges as the size of basis functions along the z -direction decreases further as depicted in Figure 4.13. In both Figures, N is the total number of basis functions (size of the impedance matrix).

As a second numerical example, the mutual coupling coefficients versus the edge to edge spacing S between two identical patches are calculated with the current method and compared with the measured results given in [81] for a cylinder with the following parameters: $a = 40$ cm, $\epsilon_r = 2.98$, $t_h = 0.762$ mm. The dimensions of the patches are $L = 6$ cm, $W = 4$ cm yielding a resonance at $1.45GHz$ where the TM_{01} mode is excited. First, the feed position is adjusted until one obtains a 50Ω input impedance for a single patch. The input impedance (real and imaginary parts) versus frequency of this antenna at the 50Ω feed location $(z_f, rl_f) = (2.1cm, 2cm)$ is given in Figure

4.14. Regarding the mutual coupling between these two identical antennas, Figures 4.15 and 4.16 present the calculated and the measured E-plane and H-plane mutual coupling coefficients versus S , respectively. In this example, the number of basis functions for a single patch is 38 (20 basis functions along the z -direction ($P = 20$) and 18 basis functions along the ϕ -direction (K)). Therefore, $N = 38$ for Figure 4.14; whereas, $N = 76$ for Figures 4.15 and 4.16. In both cases the comparison between measured and calculated results is very good and thus verifies the solutions developed in this dissertation.

It can be observed in all mutual coupling results that the H -plane coupling is always weaker than the E -plane coupling because a stronger surface wave is excited for the E -plane case. Similar phenomena is also observed in planar cases [79].

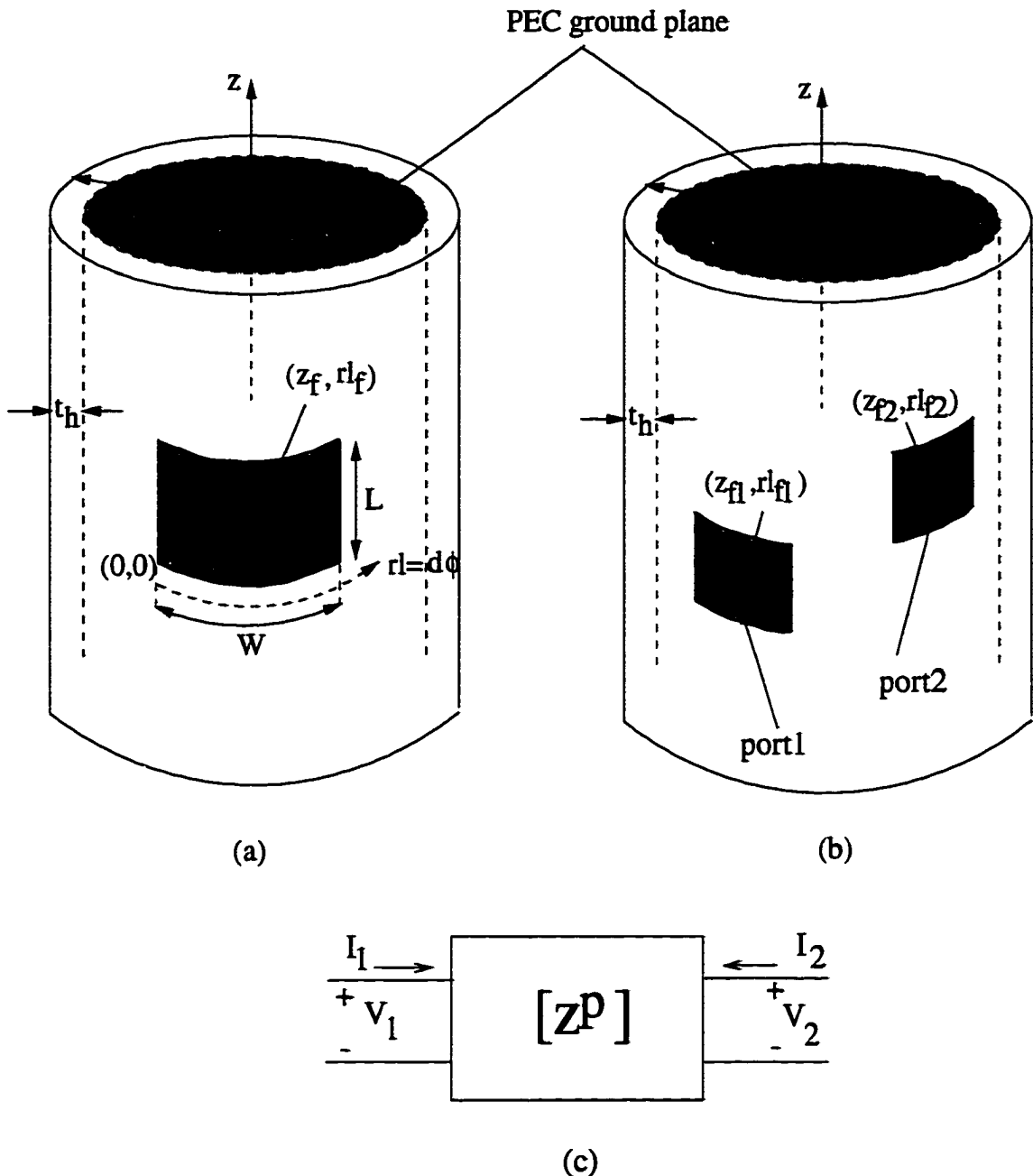


Figure 4.7: The geometry for the (a) input impedance and (b) the mutual coupling problems. (c) Definitions of two-port voltages and currents.

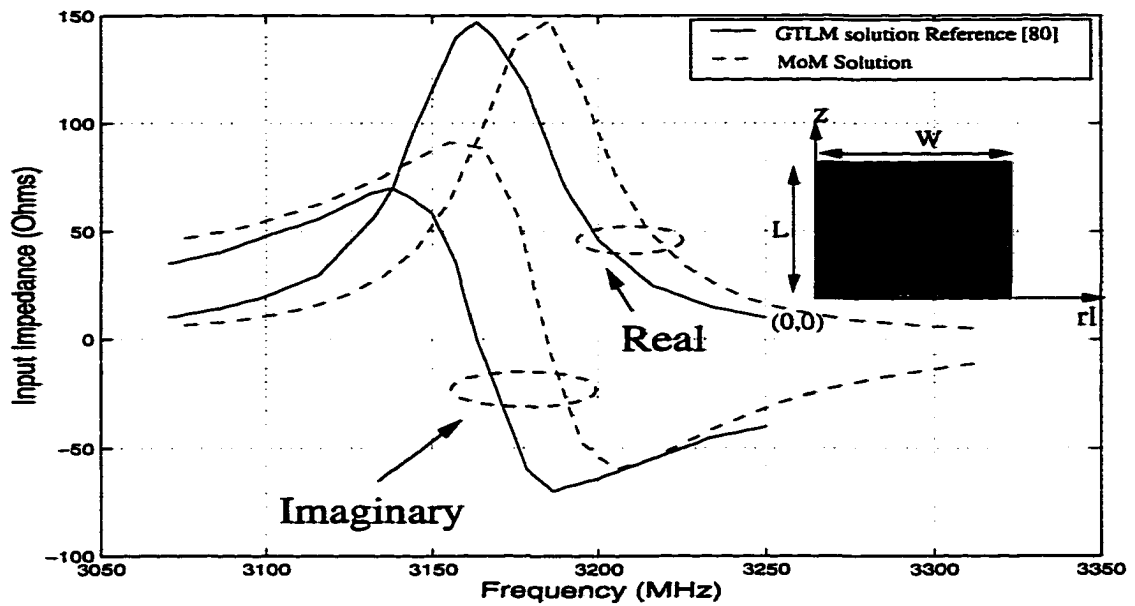


Figure 4.8: Input impedance versus frequency for the patch excited with a TM_{01} mode; $a = 20$ cm, $\epsilon_r = 2.32$, $t_h = 0.795$ mm, $L = 3$ cm, $W = 4$ cm with $(z_f, rl_f) = (0.5\text{cm}, 2\text{cm})$

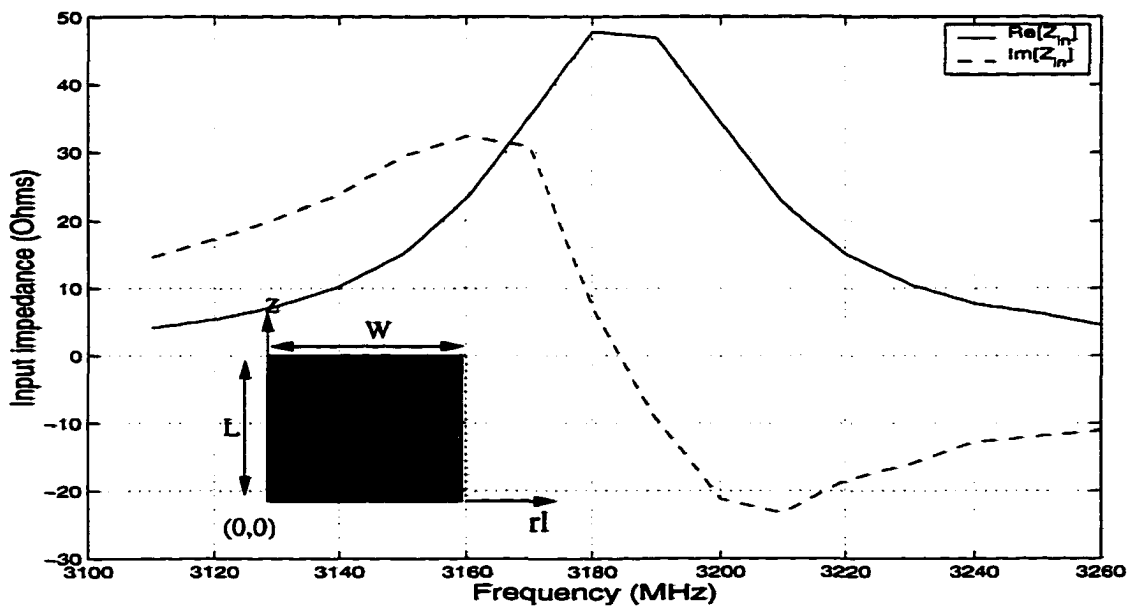


Figure 4.9: Input impedance versus frequency for the patch excited with a TM_{01} mode; $a = 20$ cm, $\epsilon_r = 2.32$, $t_h = 0.795$ mm, $L = 3$ cm, $W = 4$ cm with $(z_f, rl_f) = (0.95\text{cm}, 2\text{cm})$

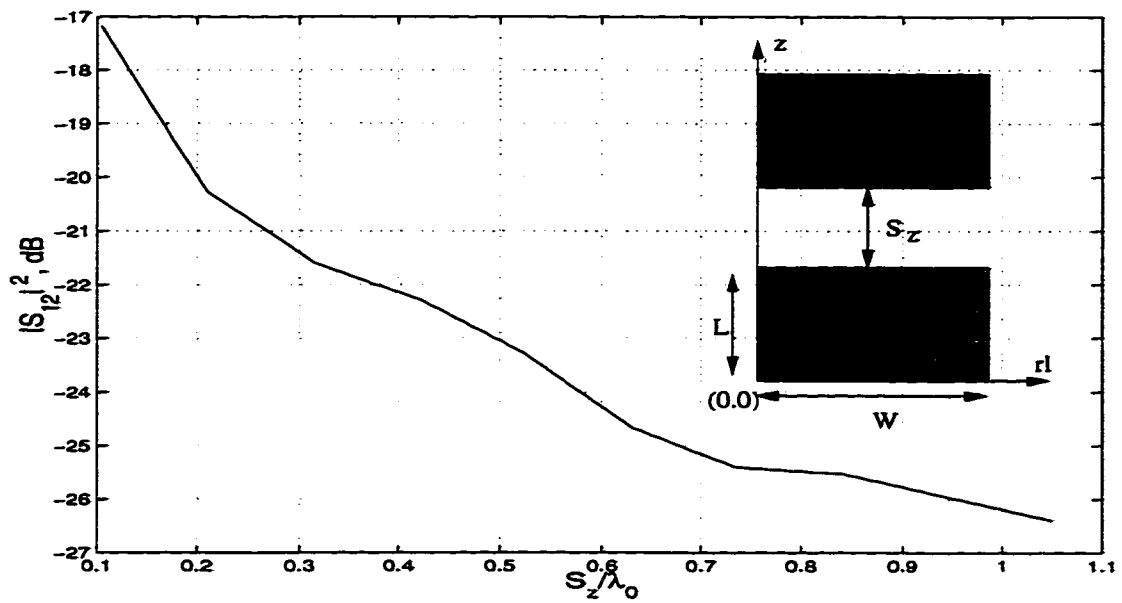


Figure 4.10: Mutual coupling coefficient s_{12} for the E-plane coupling case, the antenna parameters are the same as given in Fig. 4.9

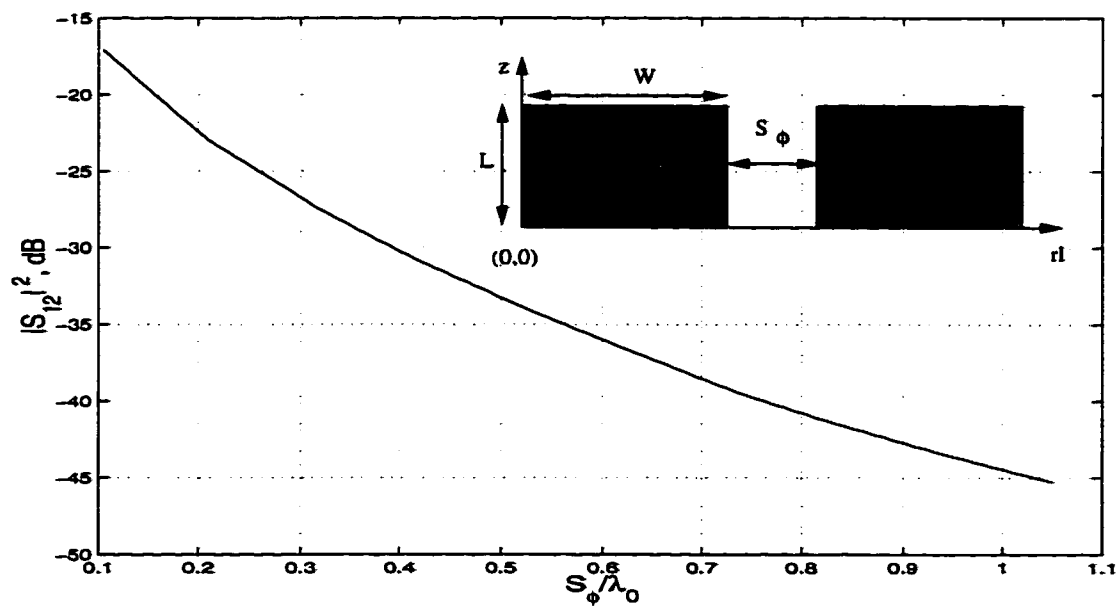


Figure 4.11: Mutual coupling coefficient s_{12} for the H-plane coupling case, the antenna parameters are the same as given in Fig. 4.9

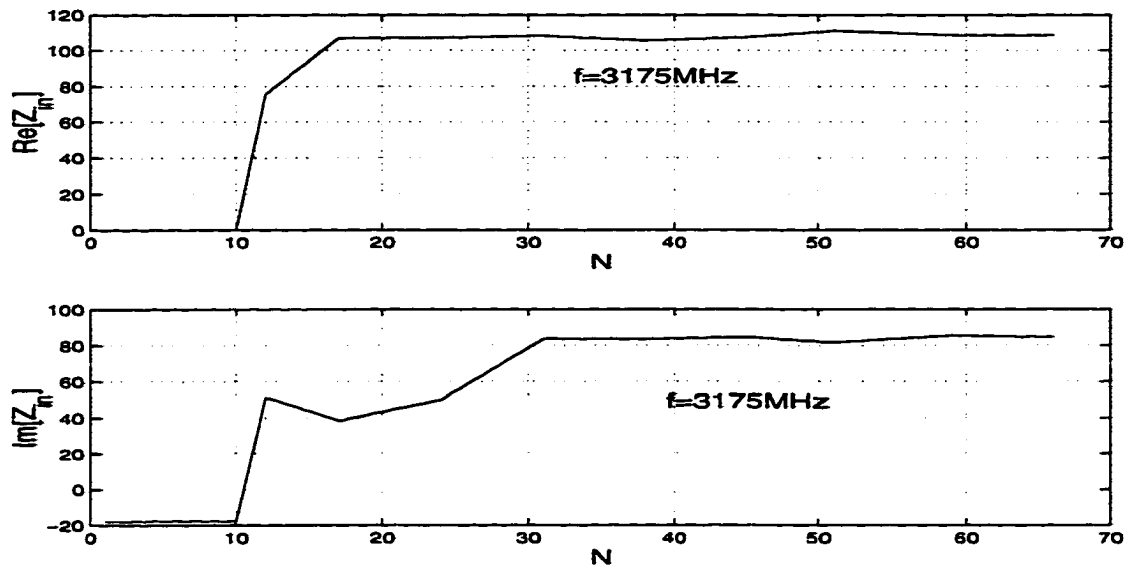


Figure 4.12: Convergence curve for input impedance at $f = 3175\text{MHz}$. The antenna parameters are: $a = 20 \text{ cm}$, $\epsilon_r = 2.32$, $t_h = 0.795 \text{ mm}$, $L = 3 \text{ cm}$, $W = 4 \text{ cm}$. Size of basis functions along the ϕ -direction is decreased while the size of the z -directed basis functions is kept constant.

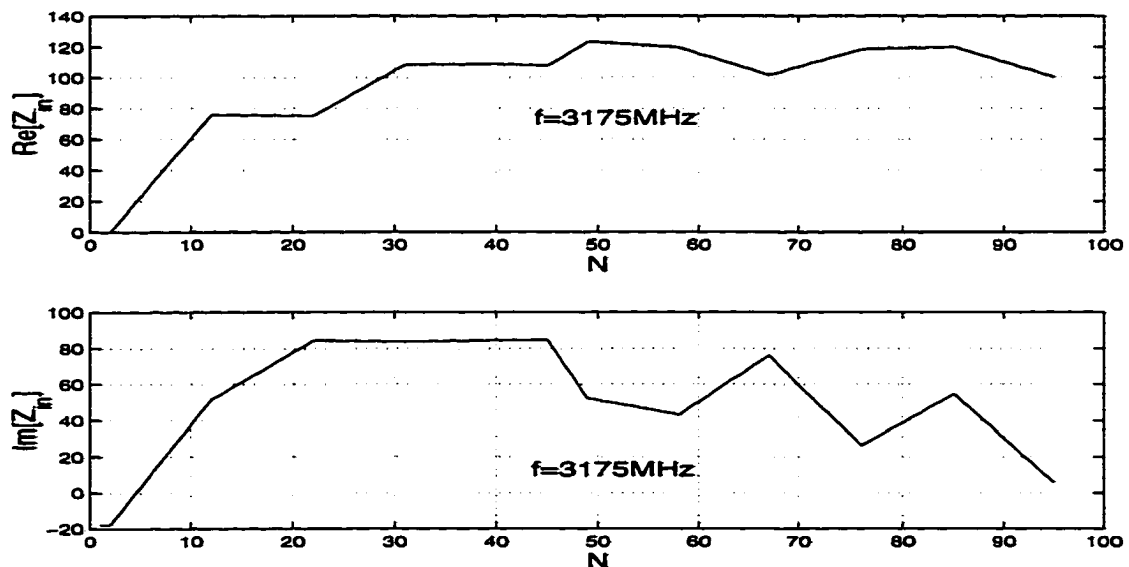


Figure 4.13: Convergence curve for input impedance at $f = 3175\text{MHz}$. The antenna parameters are: $a = 20 \text{ cm}$, $\epsilon_r = 2.32$, $t_h = 0.795 \text{ mm}$, $L = 3 \text{ cm}$, $W = 4 \text{ cm}$. Size of basis functions along the z -direction is decreased while the size of the ϕ -directed basis functions is kept constant.

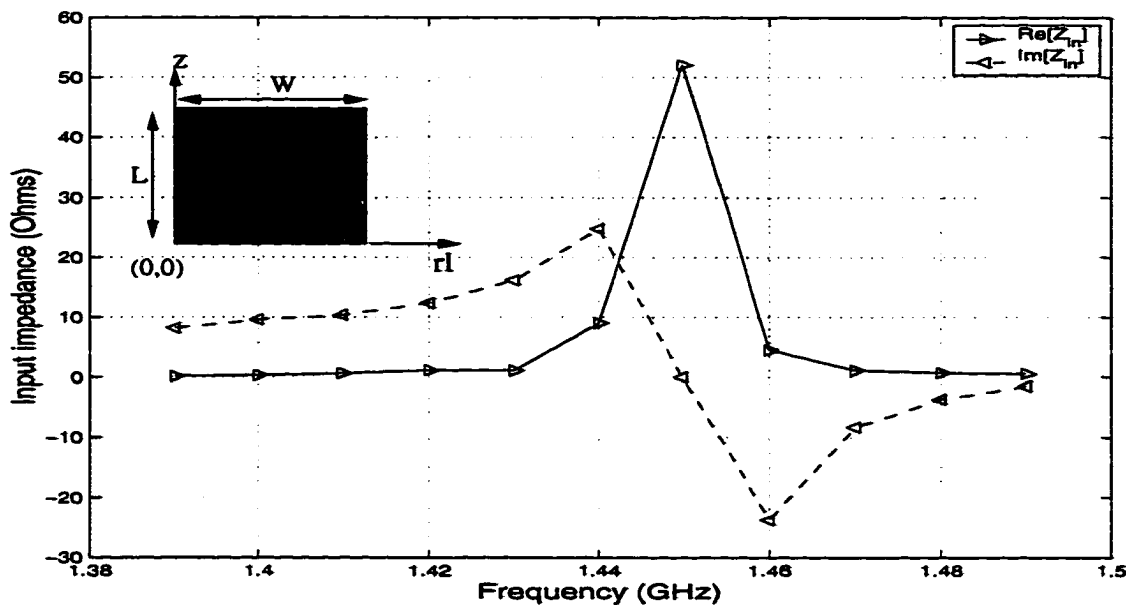


Figure 4.14: Input impedance versus frequency for the patch excited at the TM_{01} mode. The antenna parameters are: $a = 40$ cm, $\epsilon_r = 2.98$, $t_h = 0.762$ mm, $L = 6$ cm, $W = 4$ cm.

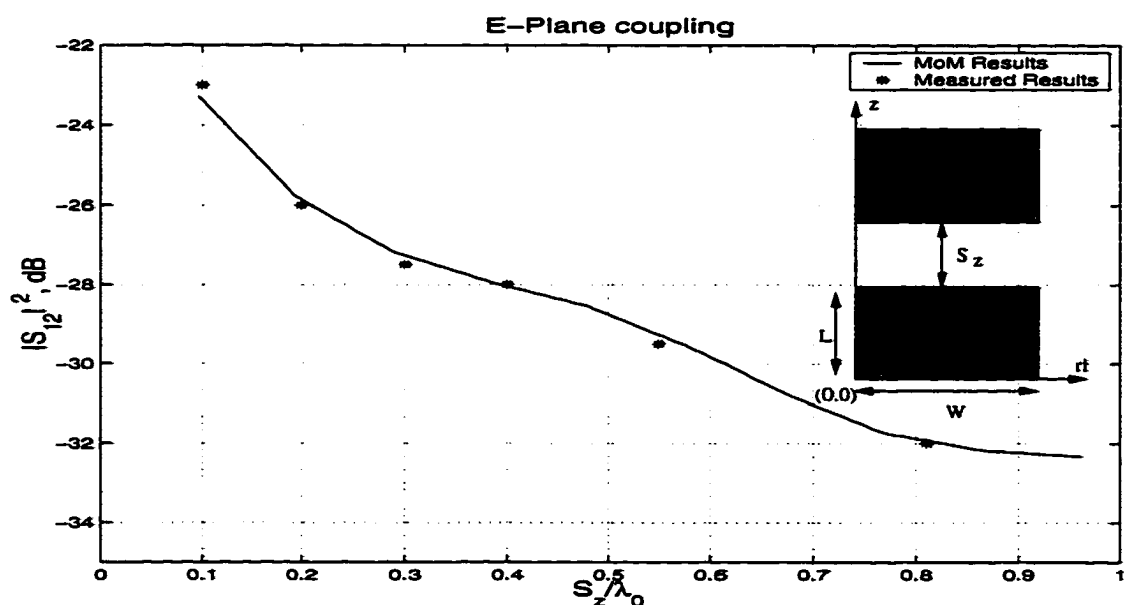


Figure 4.15: Mutual coupling coefficient s_{12} for the E-plane coupling case where the antenna parameters are the same as given in Fig. 4.14

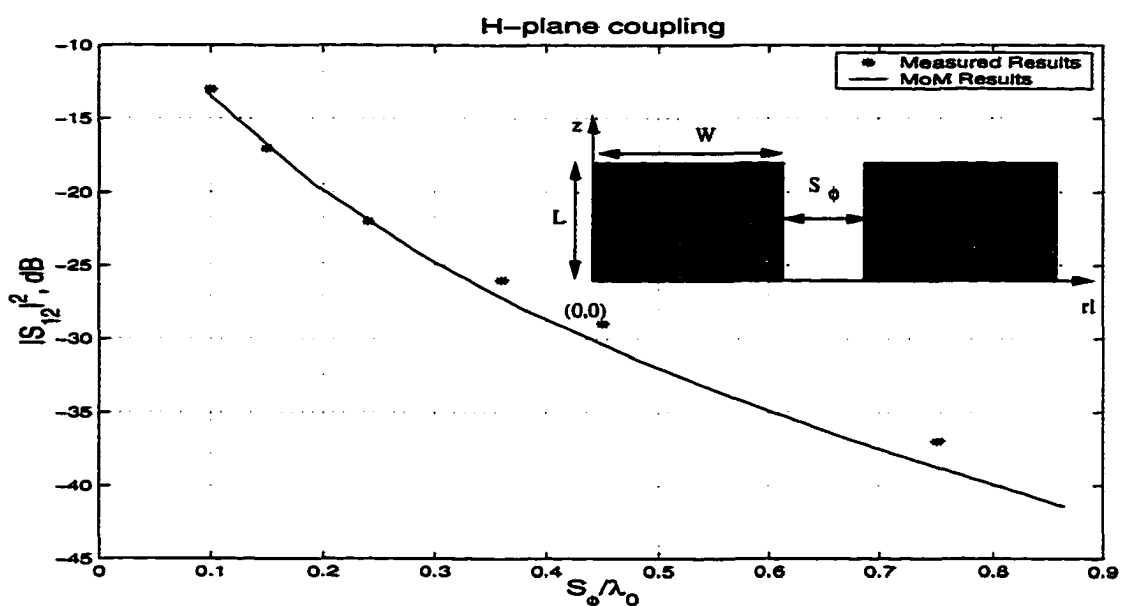


Figure 4.16: Mutual coupling coefficient s_{12} for the H-plane coupling case where the antenna parameters are the same as given in Fig. 4.14

CHAPTER 5

Conclusion

An efficient and accurate hybrid method based on the combination of the method of moments (MoM) with a special Green's function in the space domain is presented to analyze antennas and array elements conformal to material coated large circular cylinders. This method can be used for the analysis and design of microstrip structures mounted on aircraft, spacecraft and mobile communication applications where low cost, light weight and direct integrability with other devices are important. The efficiency and accuracy of the method strongly depends on the computation of the Green's function which is the kernel of the integral equation solved via the MoM for the unknown equivalent currents induced on the microstrip patches. Three types of space domain Green's function representations are used interchangeably, based on the computational efficiency of their calculation and the region where they remain highly accurate. The first one is the SDP representation of the special Green's function which is developed by obtaining a circumferentially propagating series representation of the appropriate Green's function from its radially propagating counterpart, and it is numerically evaluated along a steepest descent path (SDP) on which the integrand decays most rapidly. In this method, as the separation between the source and field point decreases, the numerical integration becomes faster and easier to perform.

The method reduces to the leading term of the saddle point integration (UTD-based Green's functions) considered in [4], [5] and [6] for the limiting case of large separations. However, in contrast to most asymptotic solutions, the results obtained in this method are valid for very small separations between source and field points. The diagonal as well as the near the diagonal elements of the MoM impedance matrix are obtained using an efficient integral representation of the planar microstrip dyadic Green's function derived by Barkeshli [7]. One can assume that for small separations between source and observation points on an electrically large dielectric coated circular cylinder, the surface of the cylinder can be considered to be locally flat. To calculate the mutual coupling between two current modes in the paraxial region, a novel space domain representation is obtained based on the fact that the circumferentially propagating series representation of the appropriate Green's function is periodic, and hence can be approximated by a Fourier series where only the leading two terms are included.

Consequently, besides the development of a MoM/Green's function scheme to obtain a computationally optimized analysis tool for conformal microstrip antennas, new asymptotic space domain Green's function representations are derived for cases in which previously derived solutions did not yield accurate results. These new solutions may be useful in the development of asymptotic solutions valid for arbitrary smooth coated surfaces. Input impedance of various microstrip antennas and mutual coupling between two identical antennas have been calculated and compared with published results to assess the accuracy of this hybrid method. The results were excellent and verified the analysis provided in this dissertation.

APPENDIX A

Limiting Case of the SDP Integral Representation of the Surface Fields for a Dielectric Coated Circular Cylinder

In the following appendix, it will be shown that the limiting case of the SDP integral representation recovers the saddle point integration covered in [4], [5] (or [72]) and [6] (which is valid for large separations between source and observation points). The UTD-based surface fields due to a tangential point electric current source located on the surface of a dielectric coated circular PEC cylinder were constructed in [4] using the algorithm depicted in Figure A.1. Although this algorithm yields the same leading terms as those of a conventional method where high-frequency based asymptotic expressions for the fields are calculated directly from their eigenfunction counterparts without going through the potentials, higher order terms (terms having $1/s^2$, $1/s^3$, etc.) obtained from this algorithm are different. Here, we show that in the limiting case of (2.70)-(2.72) where $Q = 1$, $t_1 = 0$ and $w_1 = \sqrt{\pi}$, equation (2.70)-(2.72) recovers the leading terms of the UTD-based surface fields given by [72] (equations (2.55) and (2.56)) (or by [4] equations (G.28) and (G.29)) (in this appendix, only the tangential components are considered). Note that, the higher order terms are usually important for small separations between the source and observations points. However, the accuracy of the higher order terms given by [4] is questionable. Furthermore, the

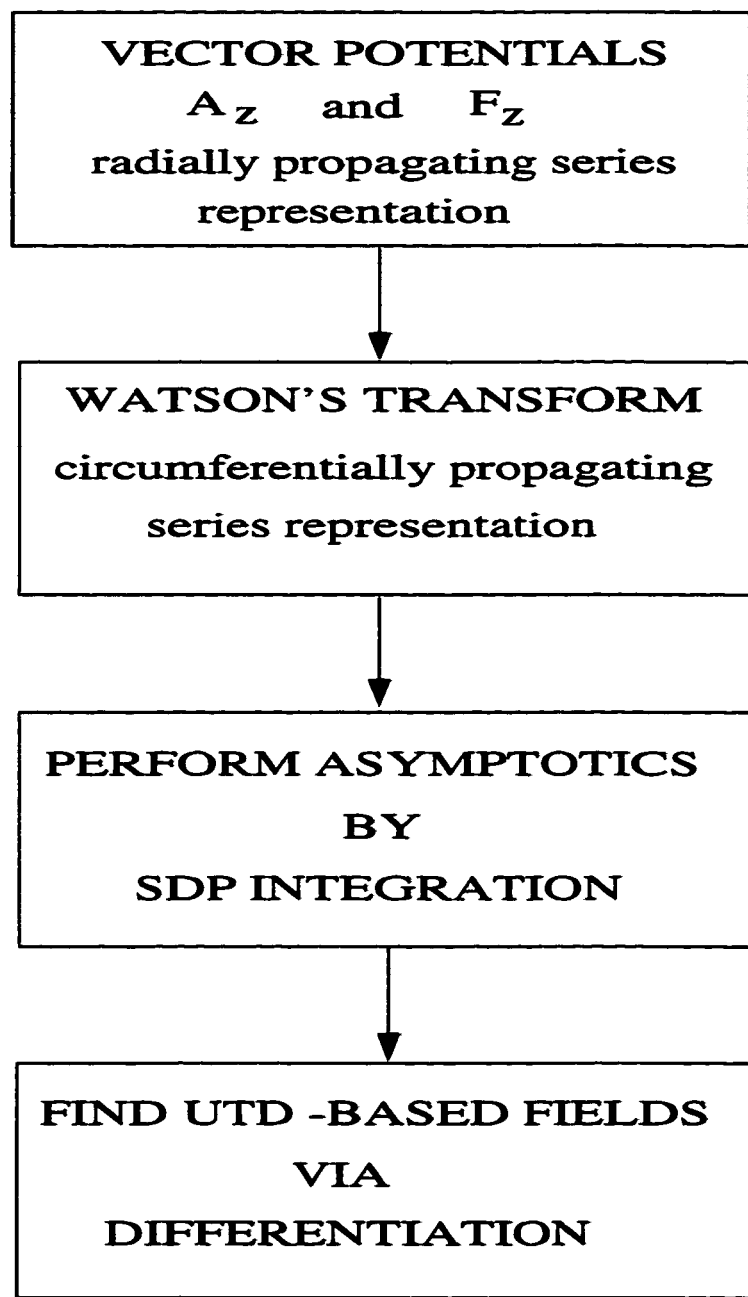


Figure A.1: High frequency method used by [3] to find the UTD-based radiated and surface fields

surface field E_z due to P_e^ϕ is not equal to E_ϕ due to P_e^z ($G_{z\phi} \neq G_{\phi z}$) when the higher order terms are included, though they are identical when the leading terms are considered only. Nevertheless, the SDP integral representation of the Green's function already yields good results for arbitrary small separations (up to $0.1\lambda_0$). In Section A, (2.71) will be analytically matched to the leading term of the surface field expression given by [72] (equation (2.55)) (or equation (G.28) in [4]). In a similar fashion, (2.70) will be matched to the leading term of the surface field expression given by [72] (equation (2.56)) (or equation (G.29) in [4]) in Section A.2.

A.1 The Limiting Expression for $E_z(\alpha, s)$

Consider (2.71) in the limiting case given by

$$E_z(\alpha, s) \approx \frac{\sqrt{2} e^{j3\pi/4}}{4\pi^2 d} \frac{e^{-jk_0 s}}{\sqrt{k_0 s}} \sqrt{\pi} k_0 \cos \alpha m_t \left[\int_{C_\tau(0)} (G_{z\phi}(\tau, 0) P_e^\phi + G_{zz}(\tau, 0) P_e^z) e^{-j\xi\tau} d\tau \right] \quad (\text{A.1})$$

which can be written as

$$E_z(\alpha, s) \approx \frac{jZ_0}{k_0} \frac{\sqrt{2\pi} e^{j3\pi/4}}{4\pi^2 d} \frac{e^{-jk_0 s}}{\sqrt{k_0 s}} k_{t0}^2 m_t \left\{ \int_{-\infty}^{\infty} \left[k_{t0} \frac{T_e}{T} P_e^z + \frac{\nu k_z}{d} \frac{k_{t0}}{k_{tl}^2} \frac{(C_\nu^e - k_{t0} R_\nu)}{T} P_e^\phi \right] e^{-j\xi\tau} d\tau \right\} \quad (\text{A.2})$$

where we made use of $\psi(0) = \alpha$ (see (2.49)) and $C_\tau(0)$ is simply from $-\infty$ to ∞ .

Now consider the leading term of (2.55) given by [72] where the angle δ is defined as $\frac{\pi}{2} - \alpha$ (here we rewrite the final expression in terms of α)

$$E_z(\alpha, s) \approx Z_0^2 G(k_0 s) \cos^2 \alpha \left[P_e^z V^e(\xi) + P_e^\phi (-\sin \alpha \cos \alpha) \frac{k_0^2}{k_{tl}^2} V_1^e(\xi) \right] \quad (\text{A.3})$$

where

$$G(K_0 s) \equiv \frac{k_0 Y_0}{2\pi j} \frac{e^{-jk_0 s}}{s} \quad (\text{A.4})$$

$$V^e(\xi) \equiv \sqrt{\frac{j\xi}{4\pi}} \int_{-\infty}^{\infty} d\tau e^{-j\xi\tau} \left(\frac{-1}{m_t}\right) \frac{H_{\nu}^{(2)}(K_{t0}d)}{D(\nu)} \Gamma_2^e(\nu) \quad (\text{A.5a})$$

$$V_1^e(\xi) \equiv \sqrt{\frac{j\xi}{4\pi}} \int_{-\infty}^{\infty} d\tau e^{-j\xi\tau} \left(\frac{-1}{m_t}\right) \frac{H_{\nu}^{(2)}(K_{t0}d)}{D(\nu)} \Gamma_1^e(\nu) . \quad (\text{A.5b})$$

In (A.5a) and (A.5b)

$$D(\nu) = \Gamma_2^e(\nu) \Gamma_2^h(\nu) - f_{\nu}^e, \quad (\text{A.6})$$

$$f_{\nu}^e \equiv \frac{k_z^2 \left(\frac{\nu}{d}\right)^2 k_{t0}^2}{k_0^2} \left[\frac{1}{k_{t1}^2} - \frac{1}{k_{t0}^2} \right]^2 \left(H_{\nu}^{(2)}(k_{t0}d) \right)^2, \quad (\text{A.7})$$

$$\Gamma_i^{(e)}(\nu) \equiv H_{\nu}^{(2)\prime}(k_{t0}d) - \Lambda_i^{(e)}(\nu) H_{\nu}^{(2)}(k_{t0}d), \quad (\text{A.8})$$

and (for $i = 1, 2$)

$$\Lambda_1^{(e)}(\nu) \equiv \frac{k_1 k_{t1}}{k_0 k_{t0}} Z_{(0)} Y_{(1)} C_{\nu}^{(e)}(a) \quad (\text{A.9a})$$

$$\Lambda_2^{(e)}(\nu) \equiv \frac{k_1 k_{t0}}{k_0 k_{t1}} Z_{(1)} Y_{(0)} C_{\nu}^{(e)}(a). \quad (\text{A.9b})$$

with the functions $C_{\nu}^{(e)}(a)$ are defined as

$$C_{\nu}^e(a) \equiv \frac{J'_{\nu}(k_{t1}a) H_{\nu}^{(2)\prime}(k_{t1}d) - J'_{\nu}(k_{t1}d) H_{\nu}^{(2)\prime}(k_{t1}a)}{J'_{\nu}(k_{t1}a) H_{\nu}^{(2)}(k_{t1}d) - J_{\nu}(k_{t1}d) H_{\nu}^{(2)\prime}(k_{t1}a)} \quad (\text{A.10a})$$

$$C_{\nu}^h(a) \equiv \frac{J_{\nu}(k_{t1}a) H_{\nu}^{(2)\prime}(k_{t1}d) - J'_{\nu}(k_{t1}d) H_{\nu}^{(2)}(k_{t1}a)}{J_{\nu}(k_{t1}a) H_{\nu}^{(2)}(k_{t1}d) - J_{\nu}(k_{t1}d) H_{\nu}^{(2)}(k_{t1}a)} . \quad (\text{A.10b})$$

Note that the expressions $C_\nu^{(\epsilon)}(a)$ are defined slightly different than $C_\nu^{(h)}$ which are defined in (2.22). Now, the above expressions ((A.6)-(A.9)) given by [4] can be recognized as,

$$\Lambda_1^e(\nu) \equiv \frac{C_\nu^e}{k_{t0}} , \quad (\text{A.11a})$$

$$\Lambda_2^e(\nu) \equiv \frac{k_{t0} C_\nu^e}{k_{t1}^2} , \quad (\text{A.11b})$$

$$\Lambda_2^h(\nu) \equiv \epsilon_r \frac{k_{t0} C_\nu^m}{k_{t1}^2} , \quad (\text{A.11c})$$

$$f_\nu^c \equiv \left(\frac{H_\nu^{(2)}}{k_{t0}} \right)^2 T_c^2 \quad (\text{A.12})$$

resulting

$$\Gamma_1^e \equiv \frac{H_\nu^{(2)}(k_{t0}d)}{k_{t0}} (k_{t0} R_\nu - C_\nu^e) \quad (\text{A.13a})$$

$$\Gamma_2^e \equiv \frac{H_\nu^{(2)}(k_{t0}d)}{k_{t0}} T_e \quad (\text{A.13b})$$

$$\Gamma_2^h \equiv \frac{H_\nu^{(2)}(k_{t0}d)}{k_{t0}} T_m \quad (\text{A.13c})$$

and

$$D(\nu) \equiv \left(\frac{H_\nu^{(2)}}{k_{t0}} \right)^2 T . \quad (\text{A.14})$$

Consequently, the special functions $V^e(\xi)$ and $V_1^e(\xi)$ can be written as

$$V^e(\xi) \equiv \sqrt{\frac{j\xi}{4\pi}} \left(\frac{-1}{m_t} \right) \int_{-\infty}^{\infty} d\tau e^{-j\xi\tau} k_{t0} \frac{T_e}{T} \quad (\text{A.15a})$$

$$V_1^e(\xi) \equiv \sqrt{\frac{j\xi}{4\pi}} \left(\frac{-1}{m_t} \right) \int_{-\infty}^{\infty} d\tau e^{-j\xi\tau} k_{t0} \frac{(k_{t0}R_\nu - C_\nu^e)}{T} \quad (\text{A.15b})$$

On the other hand, using some algebra, the coefficient in front of (A.2) can be written as

$$\frac{jZ_0}{k_0} \frac{\sqrt{2\pi} e^{j3\pi/4}}{4\pi^2 d} \frac{e^{-jk_0 s}}{\sqrt{k_0 s}} k_{t0}^2 m_t = Z_0^2 G(k_0 s) \left(\frac{-1}{m_t} \right) \sqrt{\frac{j\xi}{4\pi}} \cos^2 \alpha. \quad (\text{A.16})$$

Finally, substituting (A.16) into (A.2), (A.2) can be expressed as

$$E_z(\alpha, s) \approx Z_0^2 G(k_0 s) \left(\frac{-1}{m_t} \right) \sqrt{\frac{j\xi}{4\pi}} \cos^2 \alpha \\ \left\{ \int_{-\infty}^{\infty} \left[k_{t0} \frac{T_e}{T} P_e^z + \frac{\nu k_z}{d} \frac{k_{t0}}{k_{t1}^2} \frac{(C_\nu^e - k_{t0} R_\nu)}{T} P_e^\phi \right] e^{-j\xi\tau} d\tau \right\} \quad (\text{A.17})$$

and making use of the approximation done by [4] where $\frac{\nu k_z}{d} \approx k_0^2 \sin \alpha \cos \alpha$ in the numerator (which is valid for large cylinders) (A.17) becomes

$$E_z(\alpha, s) \approx Z_0^2 G(k_0 s) \cos^2 \alpha \left[P_e^z \left(\frac{-1}{m_t} \right) \sqrt{\frac{j\xi}{4\pi}} \int_{-\infty}^{\infty} k_{t0} \frac{T_e}{T} e^{-j\xi\tau} d\tau + \right. \\ \left. P_e^\phi (-\sin \alpha \cos \alpha) \frac{k_0^2}{k_{t1}^2} \left(\frac{-1}{m_t} \right) \sqrt{\frac{j\xi}{4\pi}} \int_{-\infty}^{\infty} k_{t0} \frac{(k_{t0} R_\nu - C_\nu^e)}{T} e^{-j\xi\tau} d\tau \right] \quad (\text{A.18})$$

which is identical to (A.3)

A.2 The Limiting Expression for $E_\phi(\alpha, s)$

Similar to the $E_z(\alpha, s)$ case, (2.70) in the limiting case is given by

$$E_\phi(\alpha, s) \approx \frac{\sqrt{2} e^{j3\pi/4}}{4\pi^2 d} \frac{e^{-jk_0 s}}{\sqrt{k_0 s}} \sqrt{\pi} k_0 \cos \alpha m_t \\ \left[\int_{C_\tau(0)} (G_{\phi\phi}(\tau, 0) P_e^\phi + G_{\phi z}(\tau, 0) P_e^z) e^{-j\xi\tau} d\tau \right] \quad (\text{A.19})$$

which can be written as

$$\begin{aligned}
E_\phi(\alpha, s) \approx & \frac{jZ_0}{k_0} \frac{\sqrt{2\pi} e^{j3\pi/4}}{4\pi^2 d} \frac{e^{-jk_0 s}}{\sqrt{k_0 s}} k_{t0}^2 m_t \\
& \left\{ \int_{-\infty}^{\infty} \left[\left(\frac{\nu k_z}{d} \right) \frac{k_{t0}}{k_{t1}^2} \frac{(C_\nu^e - k_{t0} R_\nu)}{T} P_e^z + \left(\frac{k_0^2}{k_{t1}^2} \frac{(R_\nu C_\nu^e T_m)}{T} \right. \right. \right. \\
& \left. \left. \left. - \frac{R_\nu T_c^2}{(\epsilon_r - 1)T} - \left(\frac{\nu k_z}{dk_{t1}} \right)^2 \frac{(C_\nu^e - k_{t0} R_\nu)}{k_{t0} T} \right) P_e^\phi \right] e^{-j\xi\tau} d\tau \right\}. \quad (\text{A.20})
\end{aligned}$$

Now consider the leading term of (2.56) given by [72]

$$\begin{aligned}
E_\phi(\alpha, s) \approx & Z_0^2 G(k_0 s) \left\{ P_e^z \left(-\frac{\sin 2\alpha}{2} \right) \left[V^e(\xi) + \left(\frac{j}{k_0 s} \right) \left(\frac{U^d(\xi)}{\cos^2 \alpha} \right) \right] + \right. \\
& P_e^\phi \left[\frac{k_0^2}{k_{t1}^2} \left(\frac{\sin 2\alpha}{2} \right)^2 V_l^e(\xi) + \right. \\
& \left. \left. \left(\frac{j}{k_0 s} \right) \left(\frac{U^h(\xi)}{\cos^2 \alpha} \right) + \left(\frac{j}{k_0 s} \right) \left(\frac{k_0^2 \sin^2 \alpha}{k_{t1}^2} \right) U^d(\xi) \right] \right\} \quad (\text{A.21})
\end{aligned}$$

where

$$U^h(\xi) \equiv e^{j\frac{3\pi}{4}} \xi^{\frac{3}{2}} \left(\frac{m_t}{\sqrt{\pi}} \right) \int_{-\infty}^{\infty} d\tau e^{-j\xi\tau} \frac{H_\nu^{(2)'}(k_{t0}d)}{D(\nu)} \Lambda_2^e(\nu) \Gamma_2^h(\nu) \quad (\text{A.22a})$$

$$U^d(\xi) \equiv e^{j\frac{3\pi}{4}} \xi^{\frac{3}{2}} \left(\frac{-m_t}{\sqrt{\pi}} \right) \int_{-\infty}^{\infty} d\tau e^{-j\xi\tau} \frac{H_\nu^{(2)'}(k_{t0}d)}{D(\nu)} \left(\frac{k_1^2 - k_0^2}{k_{t1}^2} \right) H_\nu^{(2)}(k_{t0}d). \quad (\text{A.22b})$$

The V -type special functions, namely, $V^e(\xi)$ and $V_l^e(\xi)$ as well as the other expressions used in these U -type special functions are the same as given in Section A.1. Note that $\left(\frac{j}{k_0 s} \right) \left(\frac{U^d(\xi)}{\cos^2 \alpha} \right)$, $\left(\frac{j}{k_0 s} \right) \left(\frac{U^h(\xi)}{\cos^2 \alpha} \right)$ and $\left(\frac{j}{k_0 s} \right) \left(\frac{k_0^2 \sin^2 \alpha}{k_{t1}^2} \right) U^d(\xi)$ are still first order

terms and similar to those of $V^e(\xi)$ and $V_1^e(\xi)$, they can be recognized as

$$\frac{j}{k_0 s} \left(\frac{U^d(\xi)}{\cos^2 \alpha} \right) \equiv \frac{1}{m_t} \sqrt{\frac{j\xi}{4\pi}} \int_{-\infty}^{\infty} d\tau e^{-j\xi\tau} \left(\frac{k_{t0}^2}{k_{t1}^2} \right) \frac{R_\nu(\epsilon_r - 1) k_0^2}{T}, \quad (\text{A.23a})$$

$$\frac{j}{k_0 s} \left(\frac{U^h(\xi)}{\cos^2 \alpha} \right) \equiv \frac{-1}{m_t} \sqrt{\frac{j\xi}{4\pi}} \int_{-\infty}^{\infty} d\tau e^{-j\xi\tau} \left(\frac{k_{t0}^2}{k_{t1}^2} \right) \left(\frac{R_\nu C_\nu^e T_m}{T} \right), \quad (\text{A.23b})$$

$$\frac{j}{k_0 s} \left(\frac{k_0^2 \sin^2 \alpha}{k_{t1}^2} \right) U^d(\xi) \equiv \frac{k_0^2 \sin^2(2\alpha)}{4 k_{t1}^2 m_t} \sqrt{\frac{j\xi}{4\pi}}$$

$$\int_{-\infty}^{\infty} d\tau e^{-j\xi\tau} \left(\frac{k_{t0}^2}{k_{t1}^2} \right) \frac{R_\nu(\epsilon_r - 1) k_0^2}{T}, \quad (\text{A.23c})$$

respectively, where we made use of the definitions given in Section A.1 ((A.11)-(A.14)). Substituting the special functions into (A.21) and using some algebra, (A.21) can be written as

$$\begin{aligned} E_\phi(\alpha, s) \approx & Z_0^2 G(k_0 s) \left\{ P_e^z \left(-\frac{\sin 2\alpha}{2} \right) \sqrt{\frac{j\xi}{4\pi}} \left(\frac{-1}{m_t} \right) \int_{-\infty}^{\infty} d\tau e^{-j\xi\tau} \left(\frac{k_{t0}^3}{k_{t1}^2} \right) \left(\frac{k_{t0} R_\nu - C_\nu^e}{T} \right) \right. \\ & + P_e^\phi \sqrt{\frac{j\xi}{4\pi}} \left(\frac{-1}{m_t} \right) \int_{-\infty}^{\infty} d\tau e^{-j\xi\tau} \left[\left(\frac{k_0^2 \sin^2(2\alpha)}{4 k_{t1}^2} \right) k_{t0} \left(\frac{k_{t0} R_\nu - C_\nu^e}{T} \right) \right. \\ & \left. \left. + \left(\frac{k_{t0}^2}{k_{t1}^2} \right) \left(\frac{R_\nu C_\nu^e T_m}{T} \right) - \left(\frac{k_0^2 \sin^2(2\alpha)}{4 k_{t1}^4} \right) k_{t0}^2 \left(\frac{R_\nu k_0^2 (\epsilon_r - 1)}{T} \right) \right] \right\}. \quad (\text{A.24}) \end{aligned}$$

On the other hand, making use of (A.16) in (A.20), (A.20) is given by

$$\begin{aligned} E_\phi(\alpha, s) \approx & Z_0^2 G(k_0 s) \left(\frac{-1}{m_t} \right) \sqrt{\frac{j\xi}{4\pi}} \cos^2 \alpha \int_{-\infty}^{\infty} d\tau e^{-j\xi\tau} \left\{ P_e^z \left(\frac{\nu k_z}{d} \right) \left(\frac{k_{t0}}{k_{t1}^2} \right) \left(\frac{C_\nu^e - k_{t0} R_\nu}{T} \right) \right. \\ & + \left. \left[\frac{k_0^2}{k_{t1}^2} \left(\frac{R_\nu C_\nu^e T_m}{T} \right) - \frac{R_\nu T_c^2}{(\epsilon_r - 1) T} - \left(\frac{\nu k_z}{dk_{t1}} \right)^2 \left(\frac{C_\nu^e - k_{t0} R_\nu}{k_{t0} T} \right) \right] P_e^\phi \right\} \quad (\text{A.25}) \end{aligned}$$

and making use of the approximation done by [4] where $\frac{\nu k_x}{d} \approx k_0^2 \sin \alpha \cos \alpha$ in the numerator, (A.25) becomes identical to (A.24) (i.e.(A.21)).

APPENDIX B

Limiting Values of the SDP Integral Representation of the Surface Fields for a Dielectric Coated Circular Cylinder for large τ values

In the following appendix, the B_i values (2.73)-(2.77) are found as follows:

$$\lim_{\tau \rightarrow \infty} k_{t0} R_\nu = -\frac{\nu}{d} , \quad (B.1a)$$

$$\lim_{\tau \rightarrow \infty} C_\nu^m = \frac{\nu}{d} , \quad (B.1b)$$

$$\lim_{\tau \rightarrow \infty} C_\nu^e = \frac{\nu}{d} . \quad (B.1c)$$

Using (B.1a)-(B.1c), the limiting values of T_m and T_e are given by

$$\lim_{\tau \rightarrow \infty} T_m = -\frac{\nu}{d} \left[1 + \epsilon_r \frac{k_{t0}^2}{k_{tl}^2} \right] \quad (B.2a)$$

$$\lim_{\tau \rightarrow \infty} T_e = -\frac{\nu}{d} \left[1 + \frac{k_{t0}^2}{k_{tl}^2} \right] . \quad (B.2b)$$

Also writing the limiting value of T_c as

$$\lim_{\tau \rightarrow \infty} T_c = \frac{\nu}{d} \left[\frac{k_0(\epsilon_r - 1)k_z}{k_{tl}^2} \right] \quad (B.3)$$

the denominator of the Green's function components, namely, T is given by

$$\lim_{\tau \rightarrow \infty} T = \left(\frac{\nu}{d}\right)^2 \left[\left(1 + \epsilon_r \frac{k_{t0}^2}{k_{t1}^2}\right) \left(1 + \frac{k_{t0}^2}{k_{t1}^2}\right) - \left(\frac{k_0(\epsilon_r - 1)k_z}{k_{t1}^2}\right)^2 \right] \quad (\text{B.4})$$

Consequently, using (B.1a)-(B.4) in (2.18), the limiting values for the Green's function components are given by

$$\lim_{\tau \rightarrow \infty} G_{zz} = \frac{jZ_0}{k_0} k_{t0}^2 \frac{\left[1 + \frac{k_{t0}^2}{k_{t1}^2}\right]}{\left(\frac{\nu}{d}\right) \left[\left(1 + \epsilon_r \frac{k_{t0}^2}{k_{t1}^2}\right) \left(1 + \frac{k_{t0}^2}{k_{t1}^2}\right) - \left(\frac{k_0(\epsilon_r - 1)k_z}{k_{t1}^2}\right)^2 \right]} \quad (\text{B.5})$$

and for large τ values ($\frac{\nu}{d} \approx \frac{m_t \tau}{d}$)

$$\lim_{\tau \rightarrow \infty} G_{zz} = \frac{jZ_0}{k_0} k_{t0}^2 \frac{\left[1 + \frac{k_{t0}^2}{k_{t1}^2}\right]}{\left(\tau \frac{m_t}{d}\right) \left[\left(1 + \epsilon_r \frac{k_{t0}^2}{k_{t1}^2}\right) \left(1 + \frac{k_{t0}^2}{k_{t1}^2}\right) - \left(\frac{k_0(\epsilon_r - 1)k_z}{k_{t1}^2}\right)^2 \right]} \quad (\text{B.6})$$

yielding

$$B_1 = \frac{jZ_0}{k_0} k_{t0}^2 \frac{\left[1 + \frac{k_{t0}^2}{k_{t1}^2}\right]}{\left(\frac{m_t}{d}\right) \left[\left(1 + \epsilon_r \frac{k_{t0}^2}{k_{t1}^2}\right) \left(1 + \frac{k_{t0}^2}{k_{t1}^2}\right) - \left(\frac{k_0(\epsilon_r - 1)k_z}{k_{t1}^2}\right)^2 \right]} . \quad (\text{B.7})$$

Similarly,

$$\lim_{\tau \rightarrow \infty} G_{\phi z} = \frac{jZ_0}{k_0} \frac{k_{t0}^2}{k_{t1}^2} \frac{2k_z}{\left[\left(1 + \epsilon_r \frac{k_{t0}^2}{k_{t1}^2}\right) \left(1 + \frac{k_{t0}^2}{k_{t1}^2}\right) - \left(\frac{k_0(\epsilon_r - 1)k_z}{k_{t1}^2}\right)^2 \right]} = B_2 , \quad (\text{B.8})$$

$$\lim_{\tau \rightarrow \infty} G_{\phi\phi} = \frac{jZ_0}{k_0} \frac{\left(\frac{\nu}{d}\right) \left[\frac{k_0^2}{k_{t1}^2} \left(1 + \epsilon_r \frac{k_{t0}^2}{k_{t1}^2}\right) + \frac{k_0^2(\epsilon_r - 1)k_z^2}{k_{t1}^4} - 2 \frac{k_z^2}{k_{t1}^2} \right]}{\left[\left(1 + \epsilon_r \frac{k_{t0}^2}{k_{t1}^2}\right) \left(1 + \frac{k_{t0}^2}{k_{t1}^2}\right) - \left(\frac{k_0(\epsilon_r - 1)k_z}{k_{t1}^2}\right)^2 \right]} \quad (\text{B.9})$$

yielding

$$B_3 = \frac{jZ_0}{k_0} \frac{m_t}{d} \frac{\left[\frac{k_0^2}{k_{t1}^2} \left(1 + \epsilon_r \frac{k_{t0}^2}{k_{t1}^2}\right) + \frac{k_0^2(\epsilon_r - 1)k_z^2}{k_{t1}^4} - 2 \frac{k_z^2}{k_{t1}^2} \right]}{\left[\left(1 + \epsilon_r \frac{k_{t0}^2}{k_{t1}^2}\right) \left(1 + \frac{k_{t0}^2}{k_{t1}^2}\right) - \left(\frac{k_0(\epsilon_r - 1)k_z}{k_{t1}^2}\right)^2 \right]} \quad (\text{B.10})$$

and

$$B_4 = \frac{jZ_0}{k_0} k_{t0} \frac{\left[\frac{k_{t0}^2}{k_{t1}^2} \left(1 + \epsilon_r \frac{k_{t0}^2}{k_{t1}^2} \right) + \frac{k_0^2(\epsilon_r - 1)k_z^2}{k_{t1}^4} - 2 \frac{k_z^2}{k_{t1}^2} \right]}{\left[\left(1 + \epsilon_r \frac{k_{t0}^2}{k_{t1}^2} \right) \left(1 + \frac{k_{t0}^2}{k_{t1}^2} \right) - \left(\frac{k_0(\epsilon_r - 1)k_z}{k_{t1}^2} \right)^2 \right]}, \quad (\text{B.11})$$

$$\lim_{r \rightarrow \infty} G_{\rho z} = \frac{jZ_0}{k_0} \frac{\frac{d}{k_0} \left[\frac{k_{t0}^2}{k_{t1}^2} \left(\frac{k_0(\epsilon_r - 1)k_z}{k_{t1}^2} \right) \left(\frac{d^2 + a^2}{2a^2} \right) + \frac{k_z}{d} \left(1 + \frac{k_{t0}^2}{k_{t1}^2} \right) \frac{k_{t0}^2}{k_{t1}^2} \left(\frac{a+d}{2a} \right) \right]}{\left[\left(1 + \epsilon_r \frac{k_{t0}^2}{k_{t1}^2} \right) \left(1 + \frac{k_{t0}^2}{k_{t1}^2} \right) - \left(\frac{k_0(\epsilon_r - 1)k_z}{k_{t1}^2} \right)^2 \right]} \quad (\text{B.12})$$

which is equal to B_5 , and finally,

$$\begin{aligned} \lim_{r \rightarrow \infty} G_{\rho \phi} &= \frac{jZ_0}{k_0} \frac{k_{t0}^2}{k_{t1}^2} \left\{ \frac{\nu \left[- \left(1 + \epsilon_r \frac{k_{t0}^2}{k_{t1}^2} \right) \frac{k_0^2}{k_{t1}^2} - \frac{k_0^2(\epsilon_r - 1)k_z^2}{k_{t1}^4} \right] \left(\frac{d^2 + a^2}{2a^2 d} \right)}{\left[\left(1 + \epsilon_r \frac{k_{t0}^2}{k_{t1}^2} \right) \left(1 + \frac{k_{t0}^2}{k_{t1}^2} \right) - \left(\frac{k_0(\epsilon_r - 1)k_z}{k_{t1}^2} \right)^2 \right]} \right. \\ &+ \frac{\nu \left[\left(1 + \epsilon_r \frac{k_{t0}^2}{k_{t1}^2} \right) \left(1 + \frac{k_{t0}^2}{k_{t1}^2} \right) - \left(\frac{k_0(\epsilon_r - 1)k_z}{k_{t1}^2} \right)^2 \right] \frac{k_0^2}{k_{t0}^2} \left(\frac{d^2 + a^2}{2a^2 d} \right)}{\left[\left(1 + \epsilon_r \frac{k_{t0}^2}{k_{t1}^2} \right) \left(1 + \frac{k_{t0}^2}{k_{t1}^2} \right) - \left(\frac{k_0(\epsilon_r - 1)k_z}{k_{t1}^2} \right)^2 \right]} \\ &- \left. \frac{\frac{\nu}{d} \left(\frac{2k_z^2}{k_{t1}^2} \right) \left(\frac{a+d}{2a} \right)}{\left[\left(1 + \epsilon_r \frac{k_{t0}^2}{k_{t1}^2} \right) \left(1 + \frac{k_{t0}^2}{k_{t1}^2} \right) - \left(\frac{k_0(\epsilon_r - 1)k_z}{k_{t1}^2} \right)^2 \right]} \right\} \end{aligned} \quad (\text{B.13})$$

yielding

$$\begin{aligned}
B_6 &= \frac{jZ_0 k_{t0}^2}{k_0 k_{t1}^2} \left\{ \frac{m_t \left[- \left(1 + \epsilon_r \frac{k_{t0}^2}{k_{t1}^2} \right) \frac{k_{t0}^2}{k_{t1}^2} - \frac{k_0^2(\epsilon_r-1)k_z^2}{k_{t1}^4} \right] \left(\frac{d^2+a^2}{2a^2d} \right)}{\left[\left(1 + \epsilon_r \frac{k_{t0}^2}{k_{t1}^2} \right) \left(1 + \frac{k_{t0}^2}{k_{t1}^2} \right) - \left(\frac{k_0(\epsilon_r-1)k_z}{k_{t1}^2} \right)^2 \right]} \right. \\
&\quad + \frac{m_t \left[\left(1 + \epsilon_r \frac{k_{t0}^2}{k_{t1}^2} \right) \left(1 + \frac{k_{t0}^2}{k_{t1}^2} \right) - \left(\frac{k_0(\epsilon_r-1)k_z}{k_{t1}^2} \right)^2 \right] \frac{k_{t0}^2}{k_{t1}^2} \left(\frac{d^2+a^2}{2a^2d} \right)}{\left[\left(1 + \epsilon_r \frac{k_{t0}^2}{k_{t1}^2} \right) \left(1 + \frac{k_{t0}^2}{k_{t1}^2} \right) - \left(\frac{k_0(\epsilon_r-1)k_z}{k_{t1}^2} \right)^2 \right]} \\
&\quad \left. - \frac{\frac{m_t}{d} \left(\frac{2k_z^2}{k_{t1}^2} \right) \left(\frac{a+d}{2a} \right)}{\left[\left(1 + \epsilon_r \frac{k_{t0}^2}{k_{t1}^2} \right) \left(1 + \frac{k_{t0}^2}{k_{t1}^2} \right) - \left(\frac{k_0(\epsilon_r-1)k_z}{k_{t1}^2} \right)^2 \right]} \right\} \tag{B.14}
\end{aligned}$$

and

$$\begin{aligned}
B_7 &= \frac{jZ_0 k_{t0}^2}{k_0 k_{t1}^2} \left\{ \frac{k_{t0} d \left[- \left(1 + \epsilon_r \frac{k_{t0}^2}{k_{t1}^2} \right) \frac{k_{t0}^2}{k_{t1}^2} - \frac{k_0^2(\epsilon_r-1)k_z^2}{k_{t1}^4} \right] \left(\frac{d^2+a^2}{2a^2d} \right)}{\left[\left(1 + \epsilon_r \frac{k_{t0}^2}{k_{t1}^2} \right) \left(1 + \frac{k_{t0}^2}{k_{t1}^2} \right) - \left(\frac{k_0(\epsilon_r-1)k_z}{k_{t1}^2} \right)^2 \right]} \right. \\
&\quad + \frac{k_{t0} d \left[\left(1 + \epsilon_r \frac{k_{t0}^2}{k_{t1}^2} \right) \left(1 + \frac{k_{t0}^2}{k_{t1}^2} \right) - \left(\frac{k_0(\epsilon_r-1)k_z}{k_{t1}^2} \right)^2 \right] \frac{k_{t0}^2}{k_{t1}^2} \left(\frac{d^2+a^2}{2a^2d} \right)}{\left[\left(1 + \epsilon_r \frac{k_{t0}^2}{k_{t1}^2} \right) \left(1 + \frac{k_{t0}^2}{k_{t1}^2} \right) - \left(\frac{k_0(\epsilon_r-1)k_z}{k_{t1}^2} \right)^2 \right]} \\
&\quad \left. - \frac{k_{t0} \left(\frac{2k_z^2}{k_{t1}^2} \right) \left(\frac{a+d}{2a} \right)}{\left[\left(1 + \epsilon_r \frac{k_{t0}^2}{k_{t1}^2} \right) \left(1 + \frac{k_{t0}^2}{k_{t1}^2} \right) - \left(\frac{k_0(\epsilon_r-1)k_z}{k_{t1}^2} \right)^2 \right]} \right\}. \tag{B.15}
\end{aligned}$$

APPENDIX C

Approximation of Periodic Functions Using Fourier Series

A large class of periodic functions $f(t)$ can be represented as

$$f(t) = a_0 + \sum_{n=1}^{\infty} a_n \cos n\omega_0 t + \sum_{n=1}^{\infty} b_n \sin n\omega_0 t \quad (\text{C.1})$$

where a_0 , a_n and b_n are certain coefficients to be determined and ω_0 is the fundamental frequency given by

$$\omega_0 = \frac{2\pi}{T} \quad (\text{C.2})$$

where T is the fundamental period. The sufficient conditions for (C.1) to be valid are (as given in [61]):

- i) $f(t)$ can have at most a finite number of minima and maxima in any single period.
- ii) $f(t)$ can have at most a finite number of finite discontinuities in any single period.
- iii) Over any period $f(t)$ must be "absolutely integrable", that is,

$$\int_{T_0} |f(t)| dt < \infty. \quad (\text{C.3})$$

Once a function is approximated by (C.1), it is necessary to determine the coefficients a_0 , a_n and b_n . Multiplying both sides of (C.1) by $\cos n\omega_0 t$, integrating both sides over one period and invoking the orthogonality relations [61], a_0 and a_n are given by,

$$a_0 = \frac{1}{T} \int_T f(t) dt \quad (C.4a)$$

$$a_n = \frac{2}{T} \int_T f(t) \cos n\omega_0 t dt \quad (C.4b)$$

and similarly, multiplying both sides of (C.1) by $\sin n\omega_0 t$, integrating both sides over one period and invoking the orthogonality relations [61], b_n is given by,

$$b_n = \frac{2}{T} \int_T f(t) \sin n\omega_0 t dt. \quad (C.5)$$

Furthermore, if a function is even, that is, $f(t) = f(-t)$ then it can be shown that $b_n = 0$ and

$$a_n = \frac{4}{T} \int_{T/2} f(t) \cos n\omega_0 t dt. \quad (C.6)$$

and if a function is odd, that is, $f(t) = -f(-t)$, $a_n = 0$ and

$$b_n = \frac{4}{T} \int_{T/2} f(t) \sin n\omega_0 t dt. \quad (C.7)$$

APPENDIX D

Representation of $G_{\phi\phi}(\zeta, \psi)$ component as the sum of Planar + Curvature Correction terms

In this Appendix, the main steps how the $G_{\phi\phi}(\zeta, \psi)$ component is written as the sum of *planar+curvature correction* terms is explained and the curvature correction term is given explicitly, whereas explicit expressions regarding to the planar terms are given in Appendix E. The followings are the basic steps followed in this dissertation:

- * 2-term Debye approximations are used for the special functions, namely R_ν is represented by (2.57) whereas, C_ν^e and C_ν^m are represented by (2.62) and (2.63), respectively. Note that, these functions are defined the same as before with the polar transformations given by (3.2). As mentioned in Chapter 2, first terms can be recognized as the equations corresponding to the planar grounded dielectric slab, whereas the second terms can be treated as the curvature correction terms.
- * Two-term Debye approximation fails for R_ν in the ζ -domain for $|\frac{\zeta}{k_0} - 1| \leq \frac{\sin \psi}{d^{2/3}}$. Recall that R_ν can be written in the following form:

$$R_\nu(\zeta, \psi) = \begin{cases} \frac{H_{(\zeta d \sin \psi)}^{(2)'}(d\sqrt{k_0^2 - \zeta^2 \cos^2 \psi})}{H_{(\zeta d \sin \psi)}^{(2)}(d\sqrt{k_0^2 - \zeta^2 \cos^2 \psi})} & |\frac{\zeta}{k_0} - 1| \leq \frac{\sin \psi}{d^{2/3}} \\ -j \frac{\sqrt{k_0^2 - \zeta^2}}{\sqrt{k_0^2 - \zeta^2 \cos^2 \psi}} - \frac{1}{2d} \frac{\sqrt{k_0^2 - \zeta^2 \cos^2 \psi}}{(k_0^2 - \zeta^2)} & \text{elsewhere} \end{cases} \quad (\text{D.1})$$

In region $|\frac{\zeta}{k_0} - 1| \leq \frac{\sin \psi}{d^{2/3}}$, $R_\nu(\zeta, \psi)$ is rewritten as

$$\begin{aligned} R_\nu(\zeta, \psi) = & \frac{H_{(\zeta d \sin \psi)}^{(2)'}(d\sqrt{k_0^2 - \zeta^2 \cos^2 \psi})}{H_{(\zeta d \sin \psi)}^{(2)}(d\sqrt{k_0^2 - \zeta^2 \cos^2 \psi})} \\ & -j \frac{\sqrt{k_0^2 - \zeta^2}}{\sqrt{k_0^2 - \zeta^2 \cos^2 \psi}} + j \frac{\sqrt{k_0^2 - \zeta^2}}{\sqrt{k_0^2 - \zeta^2 \cos^2 \psi}} \end{aligned} \quad (\text{D.2})$$

where $-j \frac{\sqrt{k_0^2 - \zeta^2}}{\sqrt{k_0^2 - \zeta^2 \cos^2 \psi}}$ serves as the term related to the planar case and the rest serves as the term related to the curvature correction term.

- * Collect the terms which contain only the first (leading) term of the Debye approximation.
- * Perform the following 1:1 matching between the cylindrical and rectangular wave numbers:

$$\begin{aligned} k_z &= \zeta \cos \psi \longleftrightarrow k_x \\ \frac{\nu}{d} &= \mu = \zeta \sin \psi \longleftrightarrow k_y \\ \zeta^2 &\longleftrightarrow \beta^2 = k_x^2 + k_y^2 \\ k_{\rho 0} &= \sqrt{k_0^2 - \zeta^2} \longleftrightarrow k_{z0} = \sqrt{k_0^2 - \beta^2} \\ k_{\rho 1} &= \sqrt{k_1^2 - \zeta^2} \longleftrightarrow k_{z1} = \sqrt{k_1^2 - \beta^2} \end{aligned} \quad (\text{D.3})$$

Consequently, collection of terms which contain only the leading term of the Debye approximation gives the planar term (with some algebra), resulting

$$G_{yy}^p(\zeta, \psi) = \frac{-Z_0}{2\pi k_0} \left[\frac{k_0^2 U(s)}{2\pi} - \zeta^2 \frac{\sin^2 \psi}{2\pi} \left(U(s) - \frac{\epsilon_r - 1}{\epsilon_r} W(s) \right) \right] \quad (\text{D.4})$$

where $W(s)$ and $U(s)$ are given by (E.1e) and (E.1f) and, respectively.

On the other hand, rest of terms form the curvature correction term which is explicitly given by

$$G_{\phi\phi}^{cc}(\zeta, \psi) \approx \left(\frac{j Z_0}{k_0 d} \right) \left\{ \frac{Num_1(\zeta, \psi) d^2 + Num_2(\zeta, \psi) d + A_3(\zeta, \psi)}{T_0(\zeta, \psi) [T_0(\zeta, \psi) d^2 + T_1(\zeta, \psi) d + T_2(\zeta, \psi)]} \right\} \quad (\text{D.5})$$

with the following definitions:

$$Num_1(\zeta, \psi) = A_1(\zeta, \psi) T_0(\zeta, \psi) - A_0(\zeta, \psi) T_1(\zeta, \psi) \quad (\text{D.6a})$$

$$Num_2(\zeta, \psi) = A_2(\zeta, \psi) T_0(\zeta, \psi) - A_0(\zeta, \psi) T_2(\zeta, \psi) \quad (\text{D.6b})$$

where

$$A_0(\zeta, \psi) = -j \sqrt{k_0^2 - \zeta^2} S_1(\zeta, \psi) - S_4(\zeta, \psi) \quad (\text{D.7a})$$

$$A_1(\zeta, \psi) = 0.5 \left[j \sqrt{k_0^2 - \zeta^2} S_2(\zeta, \psi) - [-2dC_{fx}(\zeta, \psi)] S_1(\zeta, \psi) - S_5(\zeta, \psi) \right] \quad (\text{D.7b})$$

$$A_2(\zeta, \psi) = 0.25 \left[j \sqrt{k_0^2 - \zeta^2} S_3(\zeta, \psi) + (-2dC_{fx}(\zeta, \psi)) S_2(\zeta, \psi) \right] \quad (\text{D.7c})$$

$$A_3(\zeta, \psi) = 0.125 (-2dC_{fx}(\zeta, \psi)) S_3(\zeta, \psi) \quad (\text{D.7d})$$

$$T_0(\zeta, \psi) = Pl_1(\zeta, \psi)Pl_2(\zeta, \psi) - T_c^2(\zeta, \psi) \quad (\text{D.8a})$$

$$T_1(\zeta, \psi) = -0.5 [Pl_1(\zeta, \psi)\bar{C}_2(\zeta, \psi) + Pl_2(\zeta, \psi)\bar{C}_1(\zeta, \psi)] \quad (\text{D.8b})$$

$$T_2(\zeta, \psi) = 0.25\bar{C}_1(\zeta, \psi)\bar{C}_2(\zeta, \psi) \quad (\text{D.8c})$$

$$S_1(\zeta, \psi) = N_1(\zeta, \psi)Pl_1(\zeta, \psi) - \frac{T_c^2(\zeta, \psi)}{\epsilon_r - 1} \quad (\text{D.9a})$$

$$S_2(\zeta, \psi) = N_1(\zeta, \psi)\bar{C}_1(\zeta, \psi) - N_2(\zeta, \psi)Pl_1(\zeta, \psi) \quad (\text{D.9b})$$

$$S_3(\zeta, \psi) = N_2(\zeta, \psi)\bar{C}_1(\zeta, \psi) \quad (\text{D.9c})$$

$$S_4(\zeta, \psi) = \left(\frac{\zeta^2 \sin \psi \cos \psi}{\sqrt{k_1^2 - \zeta^2 \cos^2 \psi}} \right)^2 \left[\frac{-\sqrt{k_1^2 - \zeta^2}}{\cot \left[t_h \sqrt{k_1^2 - \zeta^2} \right]} + j\sqrt{k_0^2 - \zeta^2} \right] \quad (\text{D.9d})$$

$$S_5(\zeta, \psi) = \left(\frac{\zeta^2 \sin \psi \cos \psi}{\sqrt{k_1^2 - \zeta^2 \cos^2 \psi}} \right)^2 [C_3(\zeta, \psi) + (-2dC_{fx}(\zeta, \psi))] \quad (\text{D.9e})$$

$$N_1(\zeta, \psi) = \left(\frac{k_0^2}{k_1^2 - \zeta^2 \cos^2 \psi} \right) \left(\frac{-\sqrt{k_1^2 - \zeta^2}}{\cot \left[t_h \sqrt{k_1^2 - \zeta^2} \right]} \right) \quad (\text{D.10a})$$

$$N_2(\zeta, \psi) = \left(\frac{k_0^2}{k_1^2 - \zeta^2 \cos^2 \psi} \right) C_3(\zeta, \psi) \quad (\text{D.10b})$$

$$Pl_1(\zeta, \psi) = -j\sqrt{k_0^2 - \zeta^2} - \epsilon_r \left(\frac{k_0^2 - \zeta^2 \cos^2 \psi}{k_1^2 - \zeta^2 \cos^2 \psi} \right) \frac{\sqrt{k_1^2 - \zeta^2}}{\tan \left[t_h \sqrt{k_1^2 - \zeta^2} \right]} \quad (\text{D.11a})$$

$$Pl_2(\zeta, \psi) = -j\sqrt{k_0^2 - \zeta^2} + \left(\frac{k_0^2 - \zeta^2 \cos^2 \psi}{k_1^2 - \zeta^2 \cos^2 \psi} \right) \frac{\sqrt{k_1^2 - \zeta^2}}{\cot \left[t_h \sqrt{k_1^2 - \zeta^2} \right]} \quad (\text{D.11b})$$

$$T_c(\zeta, \psi) = \frac{k_0(\epsilon_r - 1)}{k_1^2 - \zeta^2 \cos^2 \psi} \zeta^2 \sin \psi \cos \psi \quad (\text{D.12})$$

$$\bar{C}_1(\zeta, \psi) = [-2dC_{fx}(\zeta, \psi)] - \epsilon_r \left(\frac{k_0^2 - \zeta^2 \cos^2 \psi}{k_1^2 - \zeta^2 \cos^2 \psi} \right) C_2(\zeta, \psi) \quad (\text{D.13a})$$

$$\bar{C}_2(\zeta, \psi) = [-2dC_{fx}(\zeta, \psi)] + \left(\frac{k_0^2 - \zeta^2 \cos^2 \psi}{k_1^2 - \zeta^2 \cos^2 \psi} \right) C_3(\zeta, \psi) \quad (\text{D.13b})$$

$$C_1(\zeta, \psi) = \frac{k_0^2 - \zeta^2 \cos^2 \psi}{k_0^2 - \zeta^2} \quad (\text{D.14a})$$

$$C_2(\zeta, \psi) = \frac{k_1^2 - \zeta^2 \cos^2 \psi}{k_1^2 - \zeta^2} - \frac{t_h^2 \zeta^2 \sin^2 \psi}{\sin^2 \left[t_h \sqrt{k_1^2 - \zeta^2} \right]} \quad (\text{D.14b})$$

$$C_3(\zeta, \psi) = \frac{t_h^2 \zeta^2 \sin^2 \psi}{\cos^2 \left[t_h \sqrt{k_1^2 - \zeta^2} \right]} + \frac{k_1^2 - \zeta^2 \cos^2 \psi}{k_1^2 - \zeta^2} \tan^2 \left[t_h \sqrt{k_1^2 - \zeta^2} \right] \quad (\text{D.14c})$$

and finally,

$$C_{fx}(\zeta, \psi) = \begin{cases} j\sqrt{k_0^2 - \zeta^2} + \sqrt{k_0^2 - \zeta^2 \cos^2 \psi} \left(\frac{H_{(\zeta d \sin \psi)}^{(2)'}(d\sqrt{k_0^2 - \zeta^2 \cos^2 \psi})}{H_{(\zeta d \sin \psi)}^{(2)}(d\sqrt{k_0^2 - \zeta^2 \cos^2 \psi})} \right) & |\frac{\zeta}{k_0} - 1| \leq \frac{\sin \psi}{d^{2/3}} \\ -\frac{1}{2d} \frac{k_0^2 - \zeta^2 \cos^2 \psi}{(k_0^2 - \zeta^2)} & \text{elsewhere.} \end{cases} \quad (\text{D.15})$$

APPENDIX E

Special Functions used to Calculate the Approximate Space Domain Green's Function Representations valid in the Paraxial Region

The special functions used in (3.40)-(3.42) are given by

$$P(s) = \int_0^\infty \frac{\zeta}{jT_m^{\frac{1}{2}}(\zeta)} J_0(\zeta s) d\zeta \quad (\text{E.1a})$$

$$Q(s) = \int_0^\infty \frac{k_0^2 - \zeta^2}{j\zeta} \left\{ \frac{1}{T_m^0(\zeta)} - \frac{1}{T_m^{\frac{1}{2}}(\zeta)} \right\} J_0(\zeta s) d\zeta \quad (\text{E.1b})$$

$$M(s) = \int_0^\infty \frac{\zeta}{jT_m^0(\zeta)} J_0(\zeta s) d\zeta \quad (\text{E.1c})$$

$$R(s) = \int_0^\infty \frac{k_0^2(\epsilon_r - 1)}{k_1^2 - \zeta^2} \frac{\zeta \sqrt{k_0^2 - \zeta^2} R^0(\zeta)}{jT_m^0(\zeta) T_e^0(\zeta)} J_0(\zeta s) d\zeta \quad (\text{E.1d})$$

$$W(s) = \int_0^\infty \frac{\zeta \sqrt{k_0^2 - \zeta^2}}{Dp_1 Dp_2} J_0(\zeta s) d\zeta \quad (\text{E.1e})$$

$$U(s) = \int_0^\infty \frac{\zeta}{Dp_1} J_0(\zeta s) d\zeta \quad (\text{E.1f})$$

where

$$Dp_1(\zeta) = \sqrt{k_0^2 - \zeta^2} - j\sqrt{k_1^2 - \zeta^2} \cot \left[t_h \sqrt{k_1^2 - \zeta^2} \right] \quad (\text{E.2a})$$

$$Dp_2(\zeta) = \sqrt{k_0^2 - \zeta^2} + \frac{j\sqrt{k_1^2 - \zeta^2}}{\epsilon_r} \tan \left[t_h \sqrt{k_1^2 - \zeta^2} \right] \quad (\text{E.2b})$$

$$T_m^0(\zeta) = \sqrt{k_0^2 - \zeta^2} R^0(\zeta) - \epsilon_r \frac{k_0^2 - \zeta^2}{k_1^2 - \zeta^2} C^{m0}(\zeta) \quad (\text{E.3a})$$

$$T_e^0(\zeta) = \sqrt{k_0^2 - \zeta^2} R^0(\zeta) - \frac{k_0^2 - \zeta^2}{k_1^2 - \zeta^2} C^{e0}(\zeta) \quad (\text{E.3b})$$

$$T_m^{\frac{\pi}{2}}(\zeta) = k_0 R^{\frac{\pi}{2}}(\zeta) - C^{m\frac{\pi}{2}}(\zeta) \quad (\text{E.3c})$$

$$T_e^{\frac{\pi}{2}}(\zeta) = k_0 R^{\frac{\pi}{2}}(\zeta) - \frac{1}{\epsilon_r} C^{e\frac{\pi}{2}}(\zeta) \quad (\text{E.3d})$$

with

$$R^0(\zeta) = -j - \frac{1}{2d\sqrt{k_0^2 - \zeta^2}} \quad (\text{E.4})$$

$$R^{\frac{\pi}{2}}(\zeta) = \begin{cases} \frac{H_{(\zeta d)}^{(2)\prime}(k_0 d)}{H_{(\zeta d)}^{(2)}(k_0 d)} & |\frac{\zeta}{k_0} - 1| \leq \frac{1}{d^{2/3}} \\ -j \frac{\sqrt{k_0^2 - \zeta^2}}{k_0} - \frac{1}{2d} \frac{k_0}{(k_0^2 - \zeta^2)} & \text{elsewhere} \end{cases} \quad (\text{E.5})$$

$$C^{m0} = \frac{\sqrt{k_1^2 - \zeta^2}}{\tan \left[t_h \sqrt{k_1^2 - \zeta^2} \right]} - \frac{1}{2d} \quad (\text{E.6a})$$

$$C^{e0} = \frac{-\sqrt{k_1^2 - \zeta^2}}{\cot \left[t_h \sqrt{k_1^2 - \zeta^2} \right]} + \frac{1}{2d} \tan^2 \left[t_h \sqrt{k_1^2 - \zeta^2} \right] \quad (\text{E.6b})$$

$$C^{m\frac{\pi}{2}} = \frac{\sqrt{k_1^2 - \zeta^2}}{\tan \left[t_h \sqrt{k_1^2 - \zeta^2} \right]} - \frac{1}{2d} \left\{ \frac{k_1^2}{k_1^2 - \zeta^2} - \frac{t_h^2 \zeta^2}{\sin^2 \left[t_h \sqrt{k_1^2 - \zeta^2} \right]} \right\} \quad (\text{E.6c})$$

$$\begin{aligned} C^{e\frac{\pi}{2}} &= \frac{-\sqrt{k_1^2 - \zeta^2}}{\cot \left[t_h \sqrt{k_1^2 - \zeta^2} \right]} \\ &+ \frac{1}{2d} \left\{ \frac{t_h^2 \zeta^2}{\cos^2 \left[t_h \sqrt{k_1^2 - \zeta^2} \right]} + \frac{k_1^2 \tan^2 \left[t_h \sqrt{k_1^2 - \zeta^2} \right]}{k_1^2 - \zeta^2} \right\}. \end{aligned} \quad (\text{E.6d})$$

On the other hand, the special functions $S(s)$ and $T(s)$, which are related with the curvature correction term are given by

$$T(s) = \bar{S}(s) - \frac{S(s)}{\zeta^2} \quad (\text{E.7})$$

where

$$S(s) = \int_0^\infty \left(\frac{1}{d} \right) \left\{ \frac{Num_1^0(\zeta) d^2 + Num_2^0(\zeta) d + A_3^0(\zeta)}{T_0^0(\zeta) [T_0^0(\zeta) d^2 + T_1^0(\zeta) d + T_2^0(\zeta)]} \right\} J_0(\zeta s) \zeta d\zeta \quad (\text{E.8a})$$

$$\bar{S}(s) = \int_0^\infty \left(\frac{1}{d} \right) \left\{ \frac{Num_1^{\frac{\pi}{2}}(\zeta) d^2 + Num_2^{\frac{\pi}{2}}(\zeta) d + A_3^{\frac{\pi}{2}}(\zeta)}{T_0^{\frac{\pi}{2}}(\zeta) [T_0^{\frac{\pi}{2}}(\zeta) d^2 + T_1^{\frac{\pi}{2}}(\zeta) d + T_2^{\frac{\pi}{2}}(\zeta)]} \right\} \frac{J_0(\zeta s)}{\zeta} d\zeta \quad (\text{E.8b})$$

with

$$Num_1^0(\zeta) = A_1^0(\zeta) T_0^0(\zeta) - A_0^0(\zeta) T_1^0(\zeta) \quad (\text{E.9a})$$

$$Num_2^0(\zeta) = A_2^0(\zeta) T_0^0(\zeta) - A_0^0(\zeta) T_2^0(\zeta) \quad (\text{E.9b})$$

$$Num_1^{\frac{\pi}{2}}(\zeta) = A_1^{\frac{\pi}{2}}(\zeta)T_0^{\frac{\pi}{2}}(\zeta) - A_0^{\frac{\pi}{2}}(\zeta)T_1^{\frac{\pi}{2}}(\zeta) \quad (\text{E.10a})$$

$$Num_2^{\frac{\pi}{2}}(\zeta) = A_2^{\frac{\pi}{2}}(\zeta)T_0^{\frac{\pi}{2}}(\zeta) - A_0^{\frac{\pi}{2}}(\zeta)T_2^{\frac{\pi}{2}}(\zeta) . \quad (\text{E.10b})$$

The functions used in (E.8)-(E.10) are as follows:

$$A_0^0(\zeta) = -j\sqrt{k_0^2 - \zeta^2} S_1^0(\zeta) \quad (\text{E.11a})$$

$$A_1^0(\zeta) = 0.5 \left[j\sqrt{k_0^2 - \zeta^2} S_2^0(\zeta) - S_1^0(\zeta) \right] \quad (\text{E.11b})$$

$$A_2^0(\zeta) = 0.25 \left[j\sqrt{k_0^2 - \zeta^2} S_3^0(\zeta) + S_2^0(\zeta) \right] \quad (\text{E.11c})$$

$$A_3^0(\zeta) = 0.125 S_3^0(\zeta) \quad (\text{E.11d})$$

$$A_0^{\frac{\pi}{2}}(\zeta) = -j\sqrt{k_0^2 - \zeta^2} S_1^{\frac{\pi}{2}}(\zeta) \quad (\text{E.12a})$$

$$A_1^{\frac{\pi}{2}}(\zeta) = 0.5 \left[j\sqrt{k_0^2 - \zeta^2} S_2^{\frac{\pi}{2}}(\zeta) - \left(-2dC_{fx}^{\frac{\pi}{2}}(\zeta) \right) S_1^{\frac{\pi}{2}}(\zeta) \right] \quad (\text{E.12b})$$

$$A_2^{\frac{\pi}{2}}(\zeta) = 0.25 \left[j\sqrt{k_0^2 - \zeta^2} S_3^{\frac{\pi}{2}}(\zeta) + \left(-2dC_{fx}^{\frac{\pi}{2}}(\zeta) \right) S_2^{\frac{\pi}{2}}(\zeta) \right] \quad (\text{E.12c})$$

$$A_3^{\frac{\pi}{2}}(\zeta) = 0.125 \left(-2dC_{fx}^{\frac{\pi}{2}}(\zeta) \right) S_3^{\frac{\pi}{2}}(\zeta) \quad (\text{E.12d})$$

$$T_0^0(\zeta) = Pl_1^0(\zeta)Pl_2^0(\zeta) \quad (\text{E.13a})$$

$$T_1^0(\zeta) = -0.5 [Pl_1^0(\zeta)\bar{C}_2^0(\zeta) + Pl_2^0(\zeta)\bar{C}_1^0(\zeta)] \quad (\text{E.13b})$$

$$T_2^0(\zeta) = 0.25\bar{C}_1^0(\zeta)\bar{C}_2^0(\zeta) \quad (\text{E.13c})$$

$$T_0^{\frac{1}{2}}(\zeta) = Pl_1^{\frac{1}{2}}(\zeta)Pl_2^{\frac{1}{2}}(\zeta) \quad (\text{E.14a})$$

$$T_1^{\frac{1}{2}}(\zeta) = -0.5 [Pl_1^{\frac{1}{2}}(\zeta)\bar{C}_2^{\frac{1}{2}}(\zeta) + Pl_2^{\frac{1}{2}}(\zeta)\bar{C}_1^{\frac{1}{2}}(\zeta)] \quad (\text{E.14b})$$

$$T_2^{\frac{1}{2}}(\zeta) = 0.25\bar{C}_1^{\frac{1}{2}}(\zeta)\bar{C}_2^{\frac{1}{2}}(\zeta) \quad (\text{E.14c})$$

$$S_1^0(\zeta) = N_1^0(\zeta)Pl_1^0(\zeta) \quad (\text{E.15a})$$

$$S_2^0(\zeta) = N_1^0(\zeta)\bar{C}_1^0(\zeta) - N_2^0(\zeta)Pl_1^0(\zeta) \quad (\text{E.15b})$$

$$S_3^0(\zeta) = N_2^0(\zeta)\bar{C}_1^0(\zeta) \quad (\text{E.15c})$$

$$S_1^{\frac{\pi}{2}}(\zeta) = N_1^{\frac{\pi}{2}}(\zeta) Pl_1^{\frac{\pi}{2}}(\zeta) \quad (\text{E.16a})$$

$$S_2^{\frac{\pi}{2}}(\zeta) = N_1^{\frac{\pi}{2}}(\zeta) \tilde{C}_1^{\frac{\pi}{2}}(\zeta) - N_2^{\frac{\pi}{2}}(\zeta) Pl_1^{\frac{\pi}{2}}(\zeta) \quad (\text{E.16b})$$

$$S_3^{\frac{\pi}{2}}(\zeta) = N_2^{\frac{\pi}{2}}(\zeta) \tilde{C}_1^{\frac{\pi}{2}}(\zeta) \quad (\text{E.16c})$$

$$N_1^0(\zeta) = \frac{k_0^2}{k_1^2 - \zeta^2} \left(\frac{-\sqrt{k_1^2 - \zeta^2}}{\cot \left[t_h \sqrt{k_1^2 - \zeta^2} \right]} \right) \quad (\text{E.17a})$$

$$N_2^0(\zeta) = \frac{k_0^2}{k_1^2 - \zeta^2} \tan^2 \left[t_h \sqrt{k_1^2 - \zeta^2} \right] \quad (\text{E.17b})$$

$$N_1^{\frac{\pi}{2}}(\zeta) = \frac{1}{\epsilon_r} \left(\frac{-\sqrt{k_1^2 - \zeta^2}}{\cot \left[t_h \sqrt{k_1^2 - \zeta^2} \right]} \right) \quad (\text{E.18a})$$

$$N_2^{\frac{\pi}{2}}(\zeta) = \frac{1}{\epsilon_r} \left[\frac{t_h^2 \zeta^2}{\cos^2 \left[t_h \sqrt{k_1^2 - \zeta^2} \right]} + \frac{k_1^2}{k_1^2 - \zeta^2} \tan^2 \left[t_h \sqrt{k_1^2 - \zeta^2} \right] \right] \quad (\text{E.18b})$$

$$Pl_1^0(\zeta) = -j \sqrt{k_0^2 - \zeta^2} - \epsilon_r \left(\frac{k_0^2 - \zeta^2}{k_1^2 - \zeta^2} \right) \frac{\sqrt{k_1^2 - \zeta^2}}{\tan \left[t_h \sqrt{k_1^2 - \zeta^2} \right]} \quad (\text{E.19a})$$

$$Pl_2^0(\zeta) = -j \sqrt{k_0^2 - \zeta^2} + \left(\frac{k_0^2 - \zeta^2}{k_1^2 - \zeta^2} \right) \frac{\sqrt{k_1^2 - \zeta^2}}{\cot \left[t_h \sqrt{k_1^2 - \zeta^2} \right]} \quad (\text{E.19b})$$

$$Pl_1^{\frac{\pi}{2}}(\zeta) = -j\sqrt{k_0^2 - \zeta^2} - \frac{\sqrt{k_1^2 - \zeta^2}}{\tan \left[t_h \sqrt{k_1^2 - \zeta^2} \right]} \quad (\text{E.20a})$$

$$Pl_2^{\frac{\pi}{2}}(\zeta) = -j\sqrt{k_0^2 - \zeta^2} + \frac{1}{\epsilon_r} \left(\frac{\sqrt{k_1^2 - \zeta^2}}{\cot \left[t_h \sqrt{k_1^2 - \zeta^2} \right]} \right) \quad (\text{E.20b})$$

$$\tilde{C}_1^0(\zeta) = 1 - \epsilon_r \frac{k_0^2 - \zeta^2}{k_1^2 - \zeta^2} \quad (\text{E.21a})$$

$$\tilde{C}_2^0(\zeta) = 1 + \left(\frac{k_0^2 - \zeta^2}{k_1^2 - \zeta^2} \right) \tan^2 \left[t_h \sqrt{k_1^2 - \zeta^2} \right] \quad (\text{E.21b})$$

$$\tilde{C}_1^{\frac{\pi}{2}}(\zeta) = -2dC_{fx}^{\frac{\pi}{2}}(\zeta) - \left(\frac{k_1^2}{k_1^2 - \zeta^2} - \frac{t_h^2 \zeta^2}{\sin^2 \left[t_h \sqrt{k_1^2 - \zeta^2} \right]} \right) \quad (\text{E.22a})$$

$$\tilde{C}_2^{\frac{\pi}{2}}(\zeta) = -2dC_{fx}^{\frac{\pi}{2}}(\zeta)$$

$$+ \frac{1}{\epsilon_r} \left(\frac{t_h^2 \zeta^2}{\cos^2 \left[t_h \sqrt{k_1^2 - \zeta^2} \right]} + \frac{k_1^2}{k_1^2 - \zeta^2} \tan^2 \left[t_h \sqrt{k_1^2 - \zeta^2} \right] \right) \quad (\text{E.22b})$$

and finally,

$$C_{fx}^{\frac{\pi}{2}}(\zeta) = \begin{cases} j\sqrt{k_0^2 - \zeta^2} + k_0 \frac{H_{(\zeta d)}^{(2)'}(k_0 d)}{H_{(\zeta d)}^{(2)}(k_0 d)} & |\frac{\zeta}{k_0} - 1| \leq \frac{1}{d^{2/3}} \\ -\frac{1}{2d} \frac{k_0^2}{(k_0^2 - \zeta^2)} & \text{elsewhere .} \end{cases} \quad (\text{E.23})$$

Note that, a superscript '0' or ' $\frac{\pi}{2}$ ' denotes that a function is evaluated at $\psi = 0$ or $\psi = \frac{\pi}{2}$, respectively.

References

- [1] R. F. Harrington, *Field Computation by Moment Methods*. New York: The Macmillan Company, 1968.
- [2] E. H. Newman, "An overview of the hybrid MM/Green's function method in electromagnetics," *Proc. IEEE*, vol. 76, pp. 270–282, March 1988.
- [3] P. H. Pathak and R. G. Kouyoumjian, "An analysis of the radiation from apertures in curved surfaces by the geometrical theory of diffraction," *Proc. IEEE*, vol. 62, pp. 1438–1461, November 1974.
- [4] P. Munk, *A uniform geometrical theory of diffraction for the radiation and mutual coupling associated with antennas on a material coated convex conducting surface*. PhD thesis, The Ohio State University Dept. of Electrical Engineering, 1996.
- [5] C. Demirdag and R. G. Rojas, "Mutual coupling calculations on a dielectric coated pec cylinder using UTD-based Green's function," *IEEE Antennas and Propagation Society International Symposium Digest*, vol. 3, pp. 1525–1528, July 1997.
- [6] R. G. Rojas and V. B. Erturk, "UTD ray analysis of mutual coupling and radiation for antennas mounted on dielectric coated pec convex surfaces," *Proceedings of URSI Int. Symposium on Electromagnetic Theory*, vol. 1, pp. 178–180, May 1998.
- [7] S. Barkeshli, *Efficient approaches for evaluating the planer microstrip Green's function and its applications to the analysis of microstrip antennas*. PhD thesis, The Ohio State University Dep. of Electrical Engineering, 1987.
- [8] Z. W. Chang, L. B. Felsen, and A. Hessel, "Surface ray methods for mutual coupling in conformal arrays on cylinder and conical surfaces," Tech. Rep. N00123-76-C-0236, Polytech. Inst. New York, February 1976.
- [9] P. H. Pathak and N. Wang, "An analysis of the mutual coupling between antennas on a smooth convex surface," Tech. Rep. 784583-7, The Ohio State University ElectroScience Lab. Dep. of Electrical Engineering, October 1978.

- [10] R. J. Pogorzelski, "On the high-frequency asymptotic evaluation of the potentials of elemental sources on an anisotropic impedance cylinder," *Radio Sci.*, vol. 31, pp. 389–399, March-April 1996.
- [11] C. A. Balanis, *Advanced Engineering Electromagnetics*. New York: John Wiley & Sons, 1989.
- [12] A. Nakatini, N. G. Alexopoulos, N. K. Uzunoglu, and P. L. E. Uslenghi, "Accurate Green's function computation for printed circuit antennas on cylindrical substrates," *Electromagnetics*, vol. 6, pp. 243–254, July-Sept. 1986.
- [13] T. M. Habashy, S. M. Ali, and J. A. Kong, "Input impedance and radiation pattern of cylindrical-rectangular and wraparound microstrip antennas," *IEEE Trans. Antennas Propagat.*, vol. 38, pp. 722–731, May 1990.
- [14] R. E. Munson, "Conformal microstrip antennas and microstrip phased arrays," *IEEE Trans. Antennas Propagat.*, vol. 22, pp. 74–78, January 1974.
- [15] T. E. Clements, C. R. Paul, and A. T. Adams, "Computation of the capacitance matrix for systems of dielectric-coated cylindrical conductors," *IEEE Trans. Electromagn. Compat.*, vol. EMC-17, pp. 238–248, November 1975.
- [16] Y.-C. Wang, "Cylindrical and cylindrically wrapped strip and microstriplines," *IEEE Trans. Microwave Theory Tech.*, vol. 26, pp. 20–23, January 1978.
- [17] C. M. Krown, "Cylindrical-rectangular microstrip antenna," *IEEE Trans. Antennas Propagat.*, vol. 31, pp. 194–199, January 1983.
- [18] J. S. Dahele, R. J. Mitchell, K. M. Luk, and K. F. Lee, "Effect of curvature on characteristics of rectangular patch antenna," *Electron. Letters*, vol. 23, pp. 748–749, July 1987.
- [19] K. M. Luk, K. F. Lee, and J. S. Dahele, "Analysis of the cylindrical-rectangular patch antenna," *IEEE Trans. Antennas Propagat.*, vol. 37, pp. 143–147, February 1989.
- [20] K. M. Luk and K. F. Lee, "Characteristics of the cylindrical-circular patch antenna," *IEEE Trans. Antennas Propagat.*, vol. 38, pp. 119–123, July 1990.
- [21] J.-S. Chen and K.-L. Wong, "Theory and experiment of slot-coupled cylindrical rectangular and circular microstrip antennas," *IEEE Antennas and Propagation Society International Symposium Digest*, vol. 1, pp. 688–691, July 1996.
- [22] S.-T. Fang and K.-L. Wong, "Curvature effects on the characteristics of triangular microstrip antennas," *IEEE Antennas and Propagation Society International Symposium Digest*, vol. 2, pp. 924–927, June 1998.

- [23] G. Amendola, "Analysis of the elliptical-cylindrical-rectangular patch antenna," *IEEE Antennas and Propagation Society International Symposium Digest*, vol. 3, pp. 1586–1589, June 1998.
- [24] C.-Y. Huang, Y.-H. Liu, and K.-L. Wong, "Input impedance calculation of cylindrical rectangular microstrip antennas using GTLM theory," *IEEE Antennas and Propagation Society International Symposium Digest*, vol. 4, pp. 1792–1795, June 1995.
- [25] N. G. Alexopoulos and A. Nakatini, "Cylindrical substrate microstrip line characterization," *IEEE Trans. Microwave Theory Tech.*, vol. 35, pp. 843–849, September 1987.
- [26] A. Nakatini and N. G. Alexopoulos, "Coupled microstrip lines on a cylindrical substrate," *IEEE Trans. Microwave Theory Tech.*, vol. 35, pp. 1392–1398, December 1987.
- [27] A. Nakatini and N. G. Alexopoulos, "Microstrip elements on cylindrical substrates-general algorithm and numerical results," *Electromagnetics*, vol. 9, pp. 405–426, 1989.
- [28] B. W. Kwan, *Mutual coupling analysis for conformal microstrip antennas*. PhD thesis, The Ohio State University Dept. of Electrical Engineering, 1984.
- [29] S. M. Ali, T. M. Habashy, J.-F. Kiang, and J. A. Kong, "Resonance in cylindrical-rectangular and wraparound microstrip structures," *IEEE Trans. Microwave Theory Tech.*, vol. 37, pp. 1773–1782, November 1989.
- [30] K. L. Wong, Y. T. Cheng, and J. S. Row, "Resonance in a superstrate-loaded cylindrical-rectangular microstrip structure," *IEEE Trans. Microwave Theory Tech.*, vol. 41, pp. 814–819, May 1993.
- [31] K. L. Wong, Y. T. Cheng, and J. S. Row, "Analysis of a cylindrical-rectangular microstrip structure with an airgap," *IEEE Trans. Microwave Theory Tech.*, vol. 42, pp. 1032–1037, June 1994.
- [32] R.-B. Tsai and K. L. Wong, "Characterization of cylindrical microstriplines mounted inside a ground cylindrical surface," *IEEE Trans. Microwave Theory Tech.*, vol. 43, pp. 1607–1610, July 1995.
- [33] W. Y. Tam, A. K. Y. Lai, and K. M. Luk, "Mutual coupling between cylindrical rectangular microstrip antennas," *IEEE Trans. Antennas Propagat.*, vol. 43, pp. 897–899, August 1995.

- [34] H.-M. Chen and K.-L. Wong, "Analysis of microstrip open-end and gap discontinuities on a cylindrical body," *IEEE Antennas and Propagation Society International Symposium Digest*, vol. 4, pp. 1784–1787, June 1995.
- [35] R.-B. Tsai and K.-L. Wong, "Analysis of cylindrical printed slot and slot-coupled microstrip antennas," *IEEE Antennas and Propagation Society International Symposium Digest*, vol. 4, pp. 1788–1791, June 1995.
- [36] G. Vecchi, T. Bertuch, and M. Orefice, "Spectral-domain analysis of printed antennas of general shape on cylindrical substrates," *IEEE Antennas and Propagation Society International Symposium Digest*, vol. 3, pp. 1496–1499, July 1997.
- [37] S.-C. Pan and K. L. Wong, "Characteristics of a cylindrical triangular microstrip antenna," *Microwave Opt. Technol. Lett.*, vol. 15, pp. 49–52, May 1997.
- [38] S.-C. Pan and K. L. Wong, "Mutual coupling between triangular microstrip antennas on a cylindrical body," *Electron. Lett.*, vol. 33, pp. 1005–1006, June 1997.
- [39] P.-S. Kildal, S. Rengarajan, and A. Moldsvor, "Analysis of nearly cylindrical antennas and scattering problems using a spectrum of two-dimensional solutions," *IEEE Trans. Antennas Propagat.*, vol. 44, pp. 1183–1192, August 1996.
- [40] P. Slattman, P.-S. Kildal, and A. A. Kishk, "Radiation from patches on grounded cylindrical substrates with arbitrary cross-section," *IEEE Antennas and Propagation Society International Symposium Digest*, vol. 3, pp. 1500–1503, July 1997.
- [41] P.-S. Kildal, Z. Sipus, and M. Johansson, "Analysis of antennas on a curved multilayer structures by using the G1DMULT routine," *IEEE Antennas and Propagation Society International Symposium Digest*, vol. 3, pp. 1492–1495, July 1997.
- [42] J.-M. Jin, J. A. Berrie, R. Kipp, and S.-W. Lee, "Calculation of radiation patterns of microstrip antennas on cylindrical bodies of arbitrary cross section," *IEEE Trans. Antennas Propagat.*, vol. 45, pp. 126–132, January 1997.
- [43] D. H. Werner, G. D. Mouyis, and R. Mittra, "A reciprocity approach for determining radiation patterns of patch antennas on circularly-cylindrical platforms," *IEEE Antennas and Propagation Society International Symposium Digest*, vol. 3, pp. 1582–1585, June 1998.
- [44] R. C. Hall, C. H. Thng, and D. C. Chang, "Mixed potential Green's functions for cylindrical microstrip structures," *IEEE Antennas and Propagation Society International Symposium Digest*, vol. 4, pp. 1776–1779, June 1995.

- [45] R. C. Hall and D. I. Wu, "Modeling and design of circularly-polarized cylindrical wraparound microstrip antenna," *IEEE Antennas and Propagation Society International Symposium Digest*, vol. 1, pp. 672–675, July 1996.
- [46] D. Loffler, W. Wiesbeck, and B. Johannisson, "Conformal aperture coupled microstrip phased array on a cylindrical surface," *IEEE Antennas and Propagation Society International Symposium Digest*, July 1999.
- [47] S. B. Fonseca and A. J. Giarola, "Analysis of microstrip wraparound antennas using dyadic Green's functions," *IEEE Trans. Antennas Propagat.*, vol. 31, pp. 248–253, March 1983.
- [48] F. C. Silva, S. B. Fonseca, A. J. M. Soares, and A. J. Giarola, "Analysis of microstrip antennas on circular-cylindrical substrates with dielectric overlay," *IEEE Trans. Antennas Propagat.*, vol. 39, pp. 1398–1404, September 1991.
- [49] Z. Xiang and Y. Lu, "Electromagnetic dyadic Green's function in cylindrically multilayered media," *IEEE Trans. Microwave Theory Tech.*, vol. 44, pp. 614–621, April 1996.
- [50] L. C. Kempel and J. L. Volakis, "Scattering by cavity-baked antennas on a circular cylinder," *IEEE Trans. Antennas Propagat.*, vol. 42, pp. 1268–1278, September 1994.
- [51] J. Byun, B. Lee, and F. J. Harackiewicz, "FDTD analysis of mutual coupling between microstrip patch antennas on curved surfaces," *IEEE Antennas and Propagation Society International Symposium Digest*, July 1999.
- [52] K. Naishadham and L. B. Felsen, "Dispersion of waves guided along a cylindrical substrate-superstrate layered medium," *IEEE Trans. Antennas Propagat.*, vol. 41, pp. 304–313, March 1993.
- [53] N. Wang, "Electromagnetic scattering from a dielectric-coated circular cylinder," *IEEE Trans. Antennas Propagat.*, vol. 33, pp. 960–963, September 1985.
- [54] R. Paknys and N. Wang, "Creeping wave propagation constants and modal impedance for a dielectric coated cylinder," *IEEE Trans. Antennas Propagat.*, vol. 34, pp. 674–980, May 1986.
- [55] R. Paknys and N. Wang, "Excitation of creeping waves on a circular cylinder with a thick dielectric coating," *IEEE Trans. Antennas Propagat.*, vol. 35, pp. 1487–1489, December 1987.
- [56] H.-T. Kim and N. Wang, "UTD solution for electromagnetic scattering by a circular cylinder with thin lossy coatings," *IEEE Trans. Antennas Propagat.*, vol. 37, pp. 1463–1472, November 1989.

- [57] L. W. Pearson, "A ray representation of surface diffraction by a multilayer cylinder," *IEEE Trans. Antennas Propagat.*, vol. 35, pp. 698–707, June 1987.
- [58] L. W. Pearson, "A construction of the fields radiated by z-directed point sources of current in the presence of a cylindrically layered obstacle," *Radio Sci.*, vol. 21, pp. 559–569, July-August 1986.
- [59] M. Marin and P. H. Pathak, "Calculation of surface fields created by a current distribution on a coated circular cylinder," Tech. Rep. 721565-1, The Ohio State University ElectroScience Lab. Dep. of Electrical Engineering, April 1989.
- [60] C. Tokgoz, "Derivation of closed-form Green's functions for cylindrically stratified media," Master's thesis, The Middle East Technical University Dep. of Electrical and Electronics Engineering, 1997.
- [61] R. J. Mayhan, *Discrete-Time and Continuous-Time Linear Systems*. Massachusetts: Addison-Wesley, 1983.
- [62] D. M. Pozar, "Analysis of an infinite array of rectangular microstrip patches with idealized probe feeds," *IEEE Trans. Antennas Propagat.*, vol. 32, pp. 1101–1107, October 1984.
- [63] A. Ishimaru, *Electromagnetic Wave Propagation, Radiation and Scattering*. New Jersey: Prentice Hall, 1991.
- [64] V. A. Fock, "Diffraction of radio waves around the earth's surface," *J. Phys. U.S.S.R.*, vol. 9, pp. 256–266, 1945.
- [65] L. B. Felsen and N. Marcuvitz, *Radiation and Scattering of Waves*. New Jersey: Prentice Hall, 1973.
- [66] P. H. Pathak, "Advanced Electromagnetics-3." Unpublished EE819 Class Notes.
- [67] M. Abramowitz and I. A. Stegun, *Handbook of Mathematical Functions*. New York: Dover Publications, 1970.
- [68] R. Paknys, "Evaluation of hankel functions with complex argument and complex order ,," *IEEE Trans. Antennas Propagat.*, vol. 40, pp. 569–578, May 1992.
- [69] W. H. Press, S. A. Teukolsky, W. T. Vetterling, and B. P. Flanney, *Numerical Recipies in Fortran 77*. New York: Cambridge University Press, 1986.
- [70] L. W. Pearson, "A scheme for automatic computation of Fock-type integrals," *IEEE Trans. Antennas Propagat.*, vol. 35, pp. 1111–1118, October 1987.
- [71] O. A. Tuck, "A simple 'Filon-trapezoidal' rule," *Math. Comp.*, vol. 21, pp. 239–241, 1967.

- [72] R. G. Rojas and C. Demirdag, "UTD-based mutual coupling and radiation pattern calculations for a source excited dielectric coated pec circular cylinder," Tech. Rep. 731716-1, The Ohio State University ElectroScience Lab. Dep. of Electrical Engineering, September 1997.
- [73] R. F. Harrington, *Time-Harmonic Electromagnetic Fields*. New York: McGraw-Hill, 1961.
- [74] J. R. Mosig and F. E. Gardiol, "Analytical and numerical techniques in the Green's function treatment of microstrip antennas and scatterers," *IEE Proc., Part H*, vol. 130, pp. 175–182, March 1983.
- [75] J. R. Mosig, "Arbitrarily shaped microstrip structures and their analysis with a mixed-potential integral equation," *IEEE Trans. Microwave Theory Tech.*, vol. 36, pp. 314–323, February 1988.
- [76] K. A. Michalski and D. Zheng, "Electromagnetic scattering and radiation by surfaces of arbitrary shape in layered media, part 1: Theory," *IEEE Trans. Antennas Propagat.*, vol. 38, pp. 335–344, March 1990.
- [77] A. F. Peterson, S. L. Ray, and R. Mittra, *Computational Methods for Electromagnetics*. New York: IEEE Press, 1998.
- [78] M. A. Marin and P. H. Pathak, "An asymptotic closed-form representation for the grounded double-layer surface Green's function," *IEEE Trans. Antennas Propagat.*, vol. 40, pp. 1357–1366, November 1992.
- [79] D. M. Pozar, "Input impedance and mutual coupling of rectangular microstrip antennas," *IEEE Trans. Antennas Propagat.*, vol. 30, pp. 1191–1196, November 1984.
- [80] K. L. Wong, Y. H. Liu, and C. Y. Huang, "Generalized transmission line model for cylindrical-rectangular microstrip antenna," *Microwave Opt. Technol. Lett.*, vol. 7, pp. 729–732, November 1994.
- [81] C.-Y. Huang and Y.-T. Chang, "Curvature effects on the mutual coupling of cylindrical-rectangular microstrip antennas," *Electron. Lett.*, vol. 33, pp. 1108–1109, June 1997.